



# SAIMM

THE SOUTHERN AFRICAN INSTITUTE  
OF MINING AND METALLURGY

VOLUME 121 NO. 6 JUNE 2021



**UKWAZI**  
we do mining

ENERGY

POLY METALS

BULK MINERALS

PRECIOUS METALS

MINERAL SANDS & INDUSTRIAL MINERALS

DIAMONDS & GEMSTONES

Thermal	Metallurgical	Anthracite	Lignite	92 238 <b>U</b> Uranium
27 58.9 <b>Co</b> Cobalt	28 58.6 <b>Ni</b> Nickel	29 63.5 <b>Cu</b> Copper	30 65.3 <b>Zn</b> Zinc	82 207.2 <b>Pb</b> Lead
23 26.9 <b>Al</b> Aluminium	23 50.9 <b>V</b> Vanadium	24 51.9 <b>Cr</b> Chromium	25 54.9 <b>Mn</b> Manganese	26 55.8 <b>Fe</b> Iron
46 102.91 <b>Rh</b> Rhodium	46 106.4 <b>Pd</b> Palladium	78 195.1 <b>Pt</b> Platinum	79 196.9 <b>Au</b> Gold	47 107.8 <b>Ag</b> Silver
<b>ZrSiO<sub>4</sub></b> Zircon	<b>FeTiO<sub>2</sub></b> Ilmenite	<b>TiO<sub>2</sub></b> Rutile	Aggregates	Industrial Minerals
Kimberlite Diamonds	Alluvial Diamonds	Tanzanite	Rubies	Emeralds

Your mining technical and execution partner.  
[www.ukwazi.com](http://www.ukwazi.com)

CONNECT WITH US ON



**UKWAZI**  
we do mining

# The rules might change, but the fundamentals never do.

## We've got you covered



Ukwazi is a leading African-based specialist mining advisory company, offering a full spectrum of sector expertise. Our multi-disciplinary teams will support you in developing your mining project from inception to successful capital raising and from mine delivery to mine closure. Partner with us to design and deliver effective mines with right-sized infrastructure based on safety, agility and value.

**Your mining technical and execution partner.**

[www.ukwazi.com](http://www.ukwazi.com)

**UKWAZI**  
we do mining

CONNECT WITH US ON



## OFFICE BEARERS AND COUNCIL FOR THE 2020/2021 SESSION

### Honorary President

Mxolisi Mgojo  
President, Minerals Council South Africa

### Honorary Vice Presidents

Gwede Mantashe  
Minister of Mineral Resources, South Africa

Ebrahim Patel  
Minister of Trade, Industry and Competition, South Africa

Blade Nzimande  
Minister of Higher Education, Science and Technology, South Africa

### President

V.G. Duke

### President Elect

I.J. Geldenhuys

### Senior Vice President

Z. Botha

### Junior Vice President

W.C. Joughin

### Incoming Junior Vice President

E Matinde

### Immediate Past President

M.I. Mthenjane

### Co-opted to Office Bearers

S. Ndlovu

G.R. Lane

### Honorary Treasurer

W.C. Joughin

### Ordinary Members on Council

B. Genc	A.G. Smith
G.R. Lane	M.H. Solomon
K.M. Letsoalo	A.J.S. Spearing
T.M. Mmola	S.J. Tose
G. Njowa	M.I. van der Bank
S.J. Ntsoelengoe	A.T. van Zyl
S.M. Rupprecht	E.J. Walls
N. Singh	

### Co-opted Members

Z. Fakhraei

### Past Presidents Serving on Council

N.A. Barcza	J.L. Porter
R.D. Beck	S.J. Ramokgopa
J.R. Dixon	M.H. Rogers
H.E. James	D.A.J. Ross-Watt
R.T. Jones	G.L. Smith
A.S. Macfarlane	W.H. van Niekerk
C. Musingwini	
S. Ndlovu	

G.R. Lane-TPC Mining Chairperson

Z. Botha-TPC Metallurgy Chairperson

S.F. Manjengwa-YPC Chairperson

A.T. Chinhava-YPC Vice Chairperson

### Branch Chairpersons

Johannesburg	D.F. Jensen
Namibia	N.M. Namate
Northern Cape	I. Lute
Pretoria	S. Uludag
Western Cape	A.B. Nesbitt
Zambia	D. Muma
Zimbabwe	C.P. Sadomba
Zululand	C.W. Mienie

## PAST PRESIDENTS

### \*Deceased

* W. Bettel (1894-1895)	* R.J. Adamson (1959-1960)
* A.F. Crosse (1895-1896)	* W.S. Findlay (1960-1961)
* W.R. Feldtmann (1896-1897)	* D.G. Maxwell (1961-1962)
* C. Butters (1897-1898)	* J. de V. Lambrechts (1962-1963)
* J. Loevy (1898-1899)	* J.F. Reid (1963-1964)
* J.R. Williams (1899-1903)	* D.M. Jamieson (1964-1965)
* S.H. Pearce (1903-1904)	* H.E. Cross (1965-1966)
* W.A. Caldecott (1904-1905)	* D. Gordon Jones (1966-1967)
* W. Cullen (1905-1906)	* P. Lambooy (1967-1968)
* E.H. Johnson (1906-1907)	* R.C.J. Goode (1968-1969)
* J. Yates (1907-1908)	* J.K.E. Douglas (1969-1970)
* R.G. Bevington (1908-1909)	* V.C. Robinson (1970-1971)
* A. McA. Johnston (1909-1910)	* D.D. Howat (1971-1972)
* J. Moir (1910-1911)	* J.P. Hugo (1972-1973)
* C.B. Saner (1911-1912)	* P.W.J. van Rensburg (1973-1974)
* W.R. Dowling (1912-1913)	* R.P. Plewman (1974-1975)
* A. Richardson (1913-1914)	* R.E. Robinson (1975-1976)
* G.H. Stanley (1914-1915)	* M.D.G. Salamon (1976-1977)
* J.E. Thomas (1915-1916)	* P.A. Von Wielligh (1977-1978)
* J.A. Wilkinson (1916-1917)	* M.G. Atmore (1978-1979)
* G. Hildick-Smith (1917-1918)	* D.A. Viljoen (1979-1980)
* H.S. Meyer (1918-1919)	* P.R. Jochens (1980-1981)
* J. Gray (1919-1920)	* G.Y. Nisbet (1981-1982)
* J. Chilton (1920-1921)	* A.N. Brown (1982-1983)
* F. Wartenweiler (1921-1922)	* R.P. King (1983-1984)
* G.A. Watermeyer (1922-1923)	* J.D. Austin (1984-1985)
* F.W. Watson (1923-1924)	* H.E. James (1985-1986)
* C.J. Gray (1924-1925)	* H. Wagner (1986-1987)
* H.A. White (1925-1926)	* B.C. Alberts (1987-1988)
* H.R. Adam (1926-1927)	* C.E. Fivaz (1988-1989)
* Sir Robert Kotze (1927-1928)	* O.K.H. Steffen (1989-1990)
* J.A. Woodburn (1928-1929)	* H.G. Mosenthal (1990-1991)
* H. Pirow (1929-1930)	* R.D. Beck (1991-1992)
* J. Henderson (1930-1931)	* J.P. Hoffman (1992-1993)
* A. King (1931-1932)	* H. Scott-Russell (1993-1994)
* V. Nimmo-Dewar (1932-1933)	* J.A. Cruise (1994-1995)
* P.N. Lategan (1933-1934)	* D.A.J. Ross-Watt (1995-1996)
* E.C. Ranson (1934-1935)	* N.A. Barcza (1996-1997)
* R.A. Flugge-De-Smidt (1935-1936)	* R.P. Mohring (1997-1998)
* T.K. Prentice (1936-1937)	* J.R. Dixon (1998-1999)
* R.S.G. Stokes (1937-1938)	* M.H. Rogers (1999-2000)
* P.E. Hall (1938-1939)	* L.A. Cramer (2000-2001)
* E.H.A. Joseph (1939-1940)	* A.A.B. Douglas (2001-2002)
* J.H. Dobson (1940-1941)	* S.J. Ramokgopa (2002-2003)
* Theo Meyer (1941-1942)	* T.R. Stacey (2003-2004)
* John V. Muller (1942-1943)	* F.M.G. Egerton (2004-2005)
* C. Biccard Jeppe (1943-1944)	* W.H. van Niekerk (2005-2006)
* P.J. Louis Bok (1944-1945)	* R.P.H. Willis (2006-2007)
* J.T. McIntyre (1945-1946)	* R.G.B. Pickering (2007-2008)
* M. Falcon (1946-1947)	* A.M. Garbers-Craig (2008-2009)
* A. Clemens (1947-1948)	* J.C. Ngoma (2009-2010)
* F.G. Hill (1948-1949)	* G.V.R. Landman (2010-2011)
* O.A.E. Jackson (1949-1950)	* J.N. van der Merwe (2011-2012)
* W.E. Gooday (1950-1951)	* G.L. Smith (2012-2013)
* C.J. Irving (1951-1952)	* M. Dworzanowski (2013-2014)
* D.D. Stitt (1952-1953)	* J.L. Porter (2014-2015)
* M.C.G. Meyer (1953-1954)	* R.T. Jones (2015-2016)
* L.A. Bushell (1954-1955)	* C. Musingwini (2016-2017)
* H. Britten (1955-1956)	* S. Ndlovu (2017-2018)
* Wm. Bleloch (1956-1957)	* A.S. Macfarlane (2018-2019)
* H. Simon (1957-1958)	* M.I. Mthenjane (2019-2020)
* M. Barcza (1958-1959)	

### Honorary Legal Advisers

MH Attorneys

### Auditors

Genesis Chartered Accountants

### Secretaries

The Southern African Institute of Mining and Metallurgy

Fifth Floor, Minerals Council South Africa

5 Hollar Street, Johannesburg 2001 • P.O. Box 61127, Marshalltown 2107

Telephone (011) 834-1273/7 • Fax (011) 838-5923 or (011) 833-8156

E-mail: journal@saimm.co.za

## Editorial Board

S.O. Bada  
R.D. Beck  
P. den Hoed  
I.M. Dikgwathe  
R. Dimitrakopoulos\*  
M. Dworzanowski\*  
L. Falcon  
B. Genc  
R.T. Jones  
W.C. Joughin  
A.J. Kinghorn  
D.E.P. Klenam  
H.M. Lodewijks  
D.F. Malan  
R. Mitra\*  
C. Musingwini  
S. Ndlovu  
P.N. Neingo  
M. Nicol\*  
S.S. Nyoni  
N. Rampersad  
Q.G. Reynolds  
I. Robinson  
S.M. Rupprecht  
K.C. Sole  
A.J.S. Spearing\*  
T.R. Stacey  
E. Topal\*  
D. Tudor\*  
F.D.L. Uahengo  
D. Vogt\*

\*International Advisory Board members

## Editor /Chairman of the Editorial Board

R.M.S. Falcon

## Typeset and Published by

The Southern African Institute of Mining and Metallurgy  
P.O. Box 61127  
Marshalltown 2107  
Telephone (011) 834-1273/7  
Fax (011) 838-5923  
E-mail: journal@saimm.co.za

## Printed by

Camera Press, Johannesburg

## Advertising Representative

Barbara Spence  
Avenue Advertising  
Telephone (011) 463-7940  
E-mail: barbara@avenue.co.za

ISSN 2225-6253 (print)

ISSN 2411-9717 (online)



## Directory of Open Access Journals



# SAIMM

JOURNAL OF THE SOUTHERN AFRICAN INSTITUTE OF MINING AND METALLURGY

VOLUME 121 NO. 6 JUNE 2021

## Contents

### Journal Comment: Sustainable development, digitalization, mineral value chains, and new paradigm shifts

R. Dimitrakopoulos . . . . . iv

### President's Corner: An agile SAIMM for the agile professional

by V.G. Duke . . . . . v-vi

### News of General Interest

#### SAMCODES NEWS (June 2021)

by T.R. Marshall . . . . . vii

#### The Importance of ESG for Mineral Reporting

by T. Steele-Schober . . . . . viii-xi

## PROFESSIONAL TECHNICAL AND SCIENTIFIC PAPERS

### Depositional environment - The original control on gold processing

K.L. Youlton, J.A. Kinnaird, and B.J. Youlton . . . . . 267

*The mode of formation of gold-bearing deposits affects gold processing and extraction. In this study several South African gold deposits were considered. The refractory nature of gold ores is controlled by a limited number of well-understood mineralogical factors. Solid solution gold is linked to low temperature and pressure conditions in fine-grained sedimentary lithologies, while reactive pyrrhotite can form from hydrothermal fluids associated with mafic magmatic rocks. These formational controls can be used to reduce complications down the value chain by means of early mineralogical studies.*

### Automatic closed-loop scheduling in underground mining using discrete event simulation

by B. Skawina, M. Astrand, F. Sundqvist, J. Greberg, A. Salama, and P. Ekbeck . . . . . 277

*An automatic mine scheduling system could not only quickly reschedule mining operations, but also propose alternative solutions when necessary. In this study we present a model that integrates automatic scheduling software with discrete event simulation. This provides a safe environment to evaluate different operating rules and algorithms, and avoids the financial and physical risks associated with testing such a system directly in operation.*

### THE INSTITUTE, AS A BODY, IS NOT RESPONSIBLE FOR THE STATEMENTS AND OPINIONS ADVANCED IN ANY OF ITS PUBLICATIONS.

Copyright© 2021 by The Southern African Institute of Mining and Metallurgy. All rights reserved. Multiple copying of the contents of this publication or parts thereof without permission is in breach of copyright, but permission is hereby given for the copying of titles and abstracts of papers and names of authors. Permission to copy illustrations and short extracts from the text of individual contributions is usually given upon written application to the Institute, provided that the source (and where appropriate, the copyright) is acknowledged. Apart from any fair dealing for the purposes of review or criticism under **The Copyright Act no. 98, 1978, Section 12**, of the Republic of South Africa, a single copy of an article may be supplied by a library for the purposes of research or private study. No part of this publication may be reproduced, stored in a retrieval system, or transmitted in any form or by any means without the prior permission of the publishers. **Multiple copying of the contents of the publication without permission is always illegal.**

U.S. Copyright Law applicable to users in the U.S.A.

The appearance of the statement of copyright at the bottom of the first page of an article appearing in this journal indicates that the copyright holder consents to the making of copies of the article for personal or internal use. This consent is given on condition that the copier pays the stated fee for each copy of a paper beyond that permitted by Section 107 or 108 of the U.S. Copyright Law. The fee is to be paid through the Copyright Clearance Center, Inc., Operations Center, P.O. Box 765, Schenectady, New York 12301, U.S.A. This consent does not extend to other kinds of copying, such as copying for general distribution, for advertising or promotional purposes, for creating new collective works, or for resale.



<b>Synthesis of Pt-based alloy nanostructures</b>	
G.M. Leteba and E. van Steen . . . . .	283
<i>Optimizing the performance of multimetallic nanoparticle (NP) catalysts demands an understanding of their design. In this paper we report the influence of reductants on the shape- and morphological-evolution of Pt-based binary (PtNi and PtCo) and ternary (PtNiAu and PtCoAu) nanostructures. Nanostructures exhibiting well-defined and composition-controlled surfaces were successfully synthesized. The resulting alloy NPs are expected to display enhanced functionality as catalysts for utilization in specific chemical reactions.</i>	
<b>A Bayesian network approach for geotechnical risk assessment in underground mines</b>	
R. Mishra, L. Uotinen, and M. Rinne . . . . .	287
<i>A formal geotechnical risk assessment can help to forecast and to mitigate underground mining hazards. The purpose of this research is to present the use of Bayesian networks (BNs) as an alternative to existing risk assessment methods in underground mines by combining expert knowledge with data as it becomes available. The BN models can account for variability for multiple parameters without increasing the complexity of the calculation. BNs can work with varying amounts of data, which makes them a good tool for carrying out real-time risk assessment.</i>	
<b>Navigation and positioning technology in underground coal mines and tunnels: A review</b>	
Y. Cui, S. Liu, and Q. Liu. . . . .	295
<i>To reduce mining incidents and improve safety and production efficiency, it is important to develop technology for the autonomous positioning and navigation of mine equipment without the assistance of satellite navigation signals. In this study we review the current technological environment for positioning and navigation underground and present several integrated navigation strategies.</i>	
<b>Investigation of the mechanism for fireside corrosion in coal-fired boilers in South Africa</b>	
K.G. Moloko and J.W. van der Merwe . . . . .	305
<i>Furnace wall tubes from three coal-fired power stations were sampled and the fireside deposits examined to determine the mechanism of fireside corrosion affecting the tubes. The consistent coexistence of iron sulphide and iron oxide and high CO concentrations are indicative of substoichiometric conditions in the furnace, while the high CO concentrations detected by gas analysis indicate limited combustion caused by limited O<sub>2</sub>. These reducing conditions promote formation of FeS-rich deposits, which are the corrosive species responsible for tube degradation.</i>	
<b>Mechanical properties and damage mode of cemented tailings backfill in an acidic environment</b>	
Y. Huang, G. Wang, Y. Rao, and W. Liu. . . . .	317
<i>The characteristics and the deterioration in strength of cemented tailings backfill (CTB) in the underground acidic environment were studied. The mechanism of corrosion damage to CTB was found to be the dissolution of hydrogen ions and a sulphate ion reaction that produces an expansive substance, resulting in a deterioration of the strength of CTB.</i>	



## Sustainable development, digitalization, mineral value chains, and new paradigm shifts



The sustainable development of the Earth's mineral resources ensures the continuous supply of the raw materials and metals upon which we rely. It is a critical global problem, particularly given the growth of emerging economies and increasing environmental concerns. Digitalization and related advances have facilitated important technological progress and the emergence of several paradigm shifts in the mining industry.

One of these shifts is based on the concept of a mining complex or mineral value chain, introduced to reflect an integrated engineering system. This integrated system manages the quality-quantity and extraction of materials from a group of mines, followed by the treatment of the materials through different interconnected processing facilities to generate saleable products for delivery to customers and/or the spot market. Given its integrated nature, a mining complex is optimized simultaneously in a single mathematical model, integrating all its components to capitalize on their synergies, facilitate multi-source data integration, as well as account for and manage technical risks.

Most technical aspects of a mining complex/mineral value chain are substantially affected by uncertainties (stochasticity) stemming from multiple sources. These range from the materials available in the ground to the operational performance of a mining complex, including the ability to adapt to endogenous and exogenous changes. The effects of uncertainty are compounded by multi-level decision-making. This includes decisions about which materials to extract and when, how to stockpile and/or blend materials, use available processing streams, handle waste, manage capital investments, sequence rehabilitation, and how to transport the various products.

Critical sources of uncertainty in this integrated system include the quality and quantity of materials produced from the mines (material supply uncertainty) and the metal's spot market price (demand uncertainty). With new technological developments, it is possible to quantify and account for these uncertainties, as well as to assimilate new information collected as a mining complex operates, including data from various sensors. This new information needs to be evaluated and used to update models, forecasts, and further support complex, multi-level decision-making.

To date, new geostatistical simulation frameworks and smart(er) simultaneous stochastic optimization approaches allow us to perform the strategic planning of industrial mining complexes under uncertainty at a new scale of intricacy, not imagined a decade ago. As always, new challenges and opportunities emerge, thus it is hoped that the development of new paradigms will extend to stochastic 'self-learning' mining complexes. Self-learning will capitalize from developments in artificial intelligence, enabling engineering production systems to learn from operations and respond to new, real-time incoming production information collected by a wide range of online sensors, already available in industrial mining complexes.

New digital technologies and related R&D will continue to create technological step-changes and paradigm shifts to advance the performance of mineral value chains and support the sustainable and responsible development of mineral resources – all new, advanced and exciting developments for both the mining industry and academia.

**R. Dimitrakopoulos**



## An agile SAIMM for the agile professional

*'The most important single central fact about a free market is that no exchange takes place unless both parties benefit.'* - Milton Friedman



I was encouraged to join the SAIMM by senior university staff in the early 'eighties. Most the students in the industry (about 90%) had bursaries with one or other of the large mining houses, which at the time dominated our minerals industry. Upon employment following our graduation, we were encouraged to continue our relationship with the SAIMM, where Student Members would then progress to Associate Members.

I soon sought recognition as a fully-fledged Member because, even though there were many benefits of Associate Membership, the international relevance of the brand held greater potential for me. I saw membership of the SAIMM as an additional endorsement of the quality of my education and professional development in the South African minerals industry.

Times have since changed, and support for the SAIMM from industry has faltered. Universities still encourage their students to join the Institute, but very few (some 10%) enjoy the security of financial sponsorship from a mining company, or an offer of full-time employment at the end of their studies. A further 20% seem to find employment within six months of graduating, and another 30% manage to secure employment over the following six months. The roadmap to membership for our emerging professionals is now fragmented, and this may have shifted the youth's perceptions of the SAIMM. To many, the Institute bases its activities on technical papers, webinars, schools, seminars, and conferences. Though we do partake in these activities, they do not constitute who we are, or what we stand for as the Southern African Institute of Mining and Metallurgy.

The SAIMM is, at its core, a fraternity of professionals who strive to connect with each other, learn from one another and contribute to the industry for the benefit of tomorrow's professionals.

The Institute is not oblivious to the fact that times have changed, and we are fully committed to doing things differently. We recently reaffirmed our fundamental purpose as: *'... to provide our Members with a unique collaborative platform where they can develop as agile professionals in the rapidly evolving future of work in our sector.'*

Our administrative team have established more effective ways of working, with the aim of performing more efficiently in terms of our four well-established processes of engaging, informing, convening, and educating. These processes are the foundation of our ability to deliver on our promise to our members, as well as to the minerals industry which we all form part of.

Our new mindset looks to embracing technology for increased agility, greater flexibility, and enhanced performance. A full online membership interface system is now in place and our website is becoming increasingly user-friendly. It is rich with information and allows members easy access to the many benefits that the SAIMM has to offer.

Over the coming months, and consistent with our strategic realignment, we will be actively communicating with our members, and with mining companies, on the SAIMM's contribution to the minerals industry and its employees. We have generated a corporate brochure with a supporting video to facilitate this.

- Our Membership Committee has established a special working group to incorporate into our membership base, tomorrow's specialists and experts that our industry

## An agile SAIMM for the agile professional *(continued)*

will need, to navigate green energy-related technologies and the challenges of environmental and social governance.

- Our Young Professionals Council, with the support of the Johannesburg Branch, is engaging with the Department of Mineral Resources on a project linking community initiatives with the development of our young professionals.
- Our code of ethics has been modified to encourage higher levels of self-governance and ethical leadership.
- We are engaging more closely with the Minerals Council so that our future activities are structured to complement the many initiatives currently underway for the long-term benefit of our minerals industry. This will prevent unnecessary and unwanted duplication of effort.
- We will also seek to secure firm partnerships with businesses that ultimately benefit from SAIMM-related activities. We believe that many of our activities can be appropriately tailored through these partnerships to secure a better operating environment for our minerals industry over the medium to long term.
- The SAIMM has secured an agreement to establish a branch in China, and similar discussions have been initiated on closer ties with Turkey.

However, we are going to need a lot more support and involvement from senior professionals in our industry and from long-serving members of the SAIMM if we are to get this right.

When seen to be proudly endorsing the SAIMM and actively participating in our activities, these industry leaders will be providing our young professionals with a much broader insight into the 'depth' and 'reach' of SAIMM-related activities, while perhaps also encouraging them to emulate the behaviour of their role models, just as I was encouraged by my mentors.

I thank my peers who contributed to this President's Corner.

**V.G. Duke**  
*President, SAIMM*



## SAMCODES NEWS (June 2021)

Please go to [www.samcode.co.za](http://www.samcode.co.za) to read these and other items of interest to the CP/CV/QRE communities

### ESG INQUISITION

The GSSA is hosting a two-day ESG Inquisition webinar event in the second week of August 2021. The main objective of the event is to gather industry views and input regarding the potential ESG reporting requirements when disclosing Mineral Resource and Mineral Reserve estimates in Competent Persons reports and also in the Annual Mineral Resource and Mineral Reserve reports published by mineral companies. The current version of the SAMESG (2017) Guidelines is being redrafted and the event will strive to obtain industry views on potential improvements. It is perceived that general confusion regarding the purpose of the SAMESG guidelines needs to be clarified as well as the integration between Annual Sustainability/ESG reports and Annual Mineral Resource and Mineral Reserve reports.

- SAVE THE DATE (10-11 August 2021) for the ESG Inquisition. Attendance is free, but registration is required.
- Register at [https://zoom.us/meeting/register/tJUqde2trjMuHdZdZfjLNHKs6p\\_J-ZywPUK\\_](https://zoom.us/meeting/register/tJUqde2trjMuHdZdZfjLNHKs6p_J-ZywPUK_)

SAMCODES have launched an app that allows one to access and search the SAMREC, SAMVAL, and SAMOG codes, the JSE Section 12 Listing Rules as well as SAMESG and the Diamond/Precious Stones Reporting Guidelines. Download it from your preferred app store now.

There is a digital suggestion box on the home page of the SAMCODES website. Please let us know how you think we can improve our service to you and/or how to improve public reporting practices in general.

Your contributions in terms of photos, articles, and content are welcome – please send to [sam@saimm.co.za](mailto:sam@saimm.co.za).

T.R. Marshall

# The Importance of ESG for Mineral Reporting

Compiled by Teresa Steele-Schober

*Uvuna Sustainability and Chair of the SAMESG Committee*

Consideration of environmental, social and governance (ESG) criteria in mining projects and investments generally is a common headline in mining, business and mainstream media. Why is this the case and what does it mean for mineral resource developers in South Africa? This article explores the concept of ESG, the rationale for international concern about the importance of ESG and how the South African Mineral Reporting Codes (SAMCODES) has responded to this increased focus.

## What is ESG?

A conference held in Switzerland in August 2005 hosted by The United Nations Global Compact and others has been credited with the first formalized requirement for ESG criteria to be incorporated into the financial evaluations of companies. Final recommendations by the financial industry contributors to the event were compiled into a report titled 'Who Cares Wins'<sup>1</sup> with one of the conclusions being that the 'endorsing institutions are convinced that a better consideration of environmental, social and governance factors will ultimately contribute to stronger and more resilient investment markets, as well as contribute to the sustainable development of societies'. Recommendations from the report called on all sectors of society and business to integrate ESG into their core activities and, specifically, that investors should 'reward well-managed companies' that embrace ESG.

At the same time, the then United Nations Secretary General Kofi Annan asked a group of large institutional investors to collaborate on a process to develop what has become the Principles for Responsible Investment. The Principles (or PRI) were launched in April 2006, with the number of signatories growing since then to over 3 000. Developed 'by investors, for investors' the six Principles aim to contribute to a more sustainable global financial system and ultimately, in the long term, interests of the environment and society as a whole<sup>2</sup>.

Whilst ESG is spoken about as a single concept, it is an amalgamation of three distinct disciplines, each with their own underlying knowledge base, areas of focus, and methodologies for approaching problems and solutions. There is, however, considerable overlap amongst the three disciplines with issues in one area (e.g. pollution of a water resource) typically impacting on or being impacted by elements of the other two (e.g. reduced quality of water for downstream communities and lack of compliance with legal requirements).



## Why is it considered important?

The World Economic Forum (WEF) brings together public and private entities 'to shape global, regional and industry agendas'. In 1973 the WEF published its first Davos Manifesto<sup>3</sup> which set out a common code of ethics for business leaders. This was recently updated at the WEF's Annual Meeting in 2020 and builds on the concept of 'stakeholder capitalism' first introduced in the initial Manifesto. Stakeholder capitalism recognizes that long-term business value is only created when the interests of all stakeholders (employees, shareholders, governments, the environment, and society as a whole) are served simultaneously. This model recognizes the critical role that private corporations play as trustees of society and therefore stewards of the environment on which societies depend<sup>4</sup>.

By contrast, shareholder capitalism, which has dominated global thinking, prioritizes return of profits to shareholders and fails to recognize that companies are social organisms. Profit seeking at the expense of society and the environment has resulted in a disconnect between companies and the real economy, including natural and human capital assets on which companies depend for their profitability.

The focus on ESG issues has arisen in response to increasing global recognition of the impacts that human beings are having on our planet. Extensive areas of land have been transformed into the world's cities, farms, industrial complexes, and associated infrastructure, resulting in loss of biodiversity at a rate and scale not seen before. As one example, human beings and the livestock we rear as our food source currently constitute 96% of the mass of all mammals on the planet<sup>5</sup>. Increased standards of living for the average person have contributed to this degradation of the planet's natural assets to the point where 'the demands we make of its goods and services far exceed its ability to meet them on a sustainable basis'<sup>6</sup>.



This decade has been widely recognized as being the critical decade for global action to address climate change. Activists like Greta Thunberg and respected personalities such as Sir David Attenborough have been broadcasting messages of concern to global leaders in an effort to spur increased global action to address the planet's most pressing issues. The Paris Agreement calls on nations to strengthen the global response to the threat of climate change by curtailing the increased average global temperature to 'well below 2°C' above pre-industrial levels, increasing the ability to adapt to the adverse impact of climate change and make financial flows consistent with a pathway towards low greenhouse gas emissions and climate resilient developments<sup>7</sup>.

<sup>1</sup>The Global Compact, Who Cares Wins: Connecting financial markets to a changing world, June 2004

<sup>2</sup>Principles for Responsible Investment, <https://www.unpri.org/pri/about-the-pri>

<sup>3</sup>World Economic Forum, <https://www.weforum.org/agenda/2019/12/davos-manifesto-1973-a-code-of-ethics-for-business-leaders/>

<sup>4</sup>Klaus Schwab, <https://www.weforum.org/agenda/2019/12/why-we-need-the-davos-manifesto-for-better-kind-of-capitalism/>

<sup>5</sup>Dasgupta, P, The economics of biodiversity: The Dasgupta Review, Abridged Version, 2021

<sup>6</sup>Id

<sup>7</sup>United Nations, Paris Agreement, 2015

In pursuit of sustainable development and recognition of the challenges facing the globe, the United Nations and member states adopted 17 Sustainable Development Goals (SDGs) in 2015. The 2030 Agenda for Sustainable Development is seen as a blueprint for peace and prosperity for people and the planet, now and into the future<sup>8</sup>. The SDGs are increasingly used by companies and nations to track their contributions to achieving these goals and driving the company's own sustainability agenda.

Against this backdrop of global issues, individuals around the world are voicing their concerns about mankind's impacts on the planet and are responding in a number of ways. One response is seen in the ways that people spend or invest their money. In the USA approximately 84% of women and 90% of millennials have voiced preferences for sustainable investments. Millennials and women are expected to inherit nearly US\$60 trillion as a result of wealth transfers in the coming 15 years. Their preferences to entrust their wealth to financial advisors who integrate ESG considerations into their long-term investment strategies is a strong incentive for markets to respond accordingly<sup>9</sup>.

## So, what is sustainable investment?

Sustainable (or responsible) investing describes the process whereby ESG factors are incorporated into the investment decisions of individuals when they invest in companies, organizations, or funds. These investment decisions are based on the individual's real or perceived understanding of the environmental and/or social impacts (positive or negative) that will result from their investments in parallel with the expected financial returns. People choose to invest their money based on their values and personal priorities and some of the reasons cited as influencing their decisions include climate change, community benefits, gender parity, and health and safety, among others. The purpose of directing funds towards investments which are seen as sustainable is to generate measurable environmental and social impacts in addition to a financial return. In response to the growing demand for sustainable investment offerings, institutional investors and money managers have created investment products that enable investors to put their money into products that meet their ESG performance requirements.

The result of increased focus on sustainable investment is an increase in sustainable assets under management (AuM) in the USA from less than \$1 billion before 1995 to more than \$16 billion in 2020<sup>10</sup> (Figure 1).

In Europe, responsible investment has also grown with sustainable investment funds increasing their AuM by 12.5% between 2016 and 2018<sup>11</sup>. The number of responsible investment funds has also nearly doubled from 2012 to 2018.

BlackRock, a leading global investment manager, conducted its first sustainable investing survey in 2020 which revealed that 86% of responders in Europe, the Middle East, and Africa (EMEA) stated that sustainable investing is already, or will become, central to their investment strategies<sup>12</sup>. One of the key reasons why this is the case is because ESG integration is recognized as positively influencing the market value of shares and the long-term risk management of funds or a portfolio<sup>13</sup>.

A review of companies listed in the S&P 500 ranking was undertaken in 2019 by NASDAQ. The results concluded that companies that received high sustainability ratings 'exhibited both higher returns and less risk', whereas companies with poor ESG ratings 'showed the opposite results'<sup>14</sup>. This study suggests that the opinion of the authors of *Who Cares Wins* is indeed valid and that companies with better ESG performance are being rewarded by attracting more investment compared to those with weaker performance, which are seen as riskier investments<sup>15</sup>.

The Covid-19 pandemic has been a positive catalyst for many investment managers. Around 20% of responders to BlackRock's survey indicated that the pandemic has accelerated



**Sustainable Investing in the United States 1995–2020**

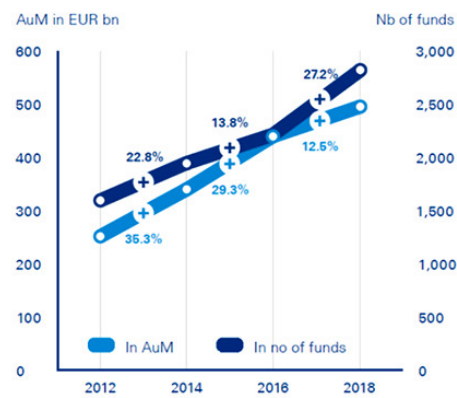
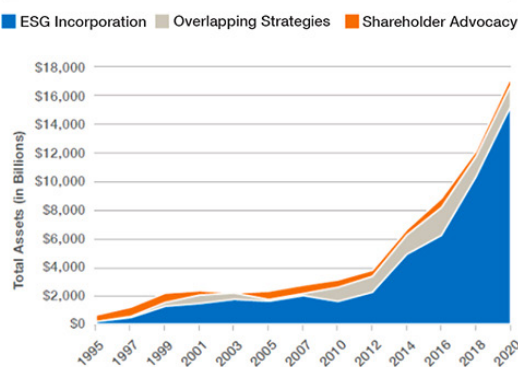


**Figure 1: (a, left) Sustainable investing in the United States (1995 – 2020) (US SIF Foundation, 2020) and (b, right) Sustainable investing in Europe (2012 – 2018) in terms of AuM and number of funds (KPMG, 2019)**

<sup>8</sup><https://sdgs.un.org/goals>

<sup>9</sup>Jeff Glitterman and Paul Ellis, ESG data drives demand for sustainable and impact investing, August 2019

<sup>10</sup>US Sustainable Investing Foundation, Report on US Sustainable and Impact Investing and Trends 2020

<sup>11</sup>KPMG European Responsible Investing Fund market 2019

<sup>12</sup>BlackRock, Sustainability goes mainstream: 2020 global sustainable investing survey, July – September 2020

<sup>13</sup>Supra note 9

<sup>14</sup>Betsy Atkins, *ESG History and Status, 2020*

<sup>15</sup>*Id*

their plans to include increase sustainable investment strategies<sup>16</sup>. The survey respondents expect to double their sustainable assets by 2025, clearly indicating that sustainable investment is not a passing phase but is rapidly emerging as the new normal investment strategy.

### What aspects of E, S, or G are investors concerned about most?

KPMG (2019) reports that the largest number of responsible investment funds in Europe are cross-sectoral funds where ESG considerations are accounted for by means of screening strategies for potential investments<sup>17</sup>. Within the environmental discipline, the environmental/ecological theme dominated in 2018, with climate mitigation and adaptation as the second largest thematic area in terms of number of funds and AuM. In the social area, while the number of social funds decreased between 2016 and 2018, the AuM increased slightly. In this arena the social and solidarity theme accounted for almost two-thirds of the social investments.

In the USA, investments made by money managers on behalf of individuals or institutional investors account for by far the largest AuM for sustainable investments. These investments were fairly evenly distributed across each of the E, S, and G categories between 2018 and 2020. The specific criteria used for investment allocation include climate change/carbon, anti-corruption, board issues, sustainable natural resources/agriculture, and executive pay. Of these criteria, climate change and carbon accounted for the largest investments by almost 50%, and grew by 39% over the period<sup>18</sup>.

BlackRock's survey confirmed that the vast majority of responders (89%) ranked environmental issues as their main ESG focus, with climate change perceived as the most urgent issue that investors want to address. Climate change is expected to remain the key focus in the next five years but social concerns are expected to grow, largely in response to societal awareness of the pandemic<sup>19</sup>.

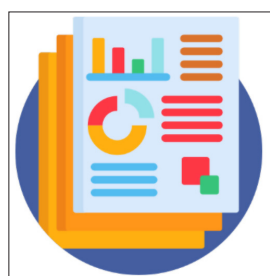


### What does this mean for Mineral Reporting standards?

The SAMCODES set the minimum standards for Public Reporting of Exploration Results, Mineral Resources, and Mineral Reserves. Such reports, by definition, are prepared for the purpose of informing investors or potential investors and their advisors on the mineral assets of a reporting company<sup>20</sup>. Within the SAMREC Code, ESG issues are considered important contributors to Modifying Factors which can influence the declaration of Mineral Reserves and, furthermore, play an important role in determining the *realistic prospects of eventual economic extraction* (RPEEE) for Mineral Resources. Investors rely on these reports to inform their investment decisions. The investors are looking for evidence of how companies integrate ESG considerations into their businesses and this evidence needs to impact all aspects of the business, including geological processes and activities.

Investors obtain ESG information about companies directly through engagement with companies or via information generated by a growing number of ESG ratings agencies (raters). These raters in turn obtain their information from companies actively or passively, or a combination thereof. Active raters will request information directly from a company (for example the Carbon Disclosure Project questionnaires), aggregate this information, and provide a rating. Passive raters on the other hand will rely solely on reviewing publicly available information to inform their assigned rating. Not all ratings agencies provide insight into their scoring requirements and companies, rightfully, have expressed concerns about what these raters do with their information and how they generate a rating<sup>21</sup>.

Sustainability reporting is largely undertaken voluntarily by companies, regardless of their listing status on a stock exchange. In response to this growing desire to report on their ESG performance, a number of reporting frameworks have been developed. Some of the more commonly used ones include the Global Reporting Initiative (GRI), Sustainability Accounting Standards Board (SASB), Carbon Disclosures Project (CDP), and Task Force on Climate-related Financial Disclosures (TCFD). The common objective of all of these frameworks is to help those who wish to disclose their sustainability performance by providing guidance and metrics that they can use. Critics of sustainability reporting suggest that these reports have done little to improve the actual management of sustainability issues at a global scale and are utilizing company resources to compile the reports that could be better spent managing sustainability issues on the ground<sup>22</sup>. Gaps also remain between society's expectations of mining companies and their performance in respect of ESG issues<sup>23</sup>. Concerns about 'greenwashing' remain, with the mining industry failing to present an honest picture of the challenges it faces and its work to support the SDGs<sup>24</sup>.



Yet investors remain hungry for access to information on which to base their decisions. More than half of the responders to the BlackRock survey noted that the quality or availability of ESG data and analytics is inadequate, and this has been cited as a barrier to increasing their sustainable investments. More and more investors are applying structured analyses of non-financial disclosures by companies and have noted that there is an increasing dissatisfaction with the ESG information presented by companies.

An EY investor survey in 2020<sup>25</sup> found that there was a 14% increase in dissatisfaction with environmental risk disclosures amongst survey responders since the previous survey in 2018. The Responsible Mining Foundation stated in its Responsible Mining Index Report (2020) that there is a severe deficit of mine-site level data on issues that are of particular interest to communities, workers, governments, and investors<sup>26</sup>. The risk to mining companies who seek investment is that the information used to inform their ESG rating may not adequately reflect the true sustainability performance of that company and investors may move their funds elsewhere as a result.

<sup>16</sup>Supra note 12

<sup>17</sup>Supra note 11

<sup>18</sup>Supra note 10

<sup>19</sup>Supra note 12

<sup>20</sup>The South African Code for the Reporting of Exploration Results, Mineral Resources and Mineral Reserves: The SAMREC Code 2016

<sup>21</sup>SustainAbility, Rate the raters 2020: Investor survey and interview results, March 2020

<sup>22</sup><https://hbr-org.cdn.ampproject.org/c/s/hbr.org/amp/2021/05/overselling-sustainability-reporting>

<sup>23</sup>Responsible Mining Foundation, Responsible Mining Index Report, 2020

<sup>24</sup>Ibid

<sup>25</sup>EY, How will ESG performance shape your future? What investors are making ESG an imperative for COVID-19 and beyond, July 2020

<sup>26</sup>Supra note 23

Further there is a need, and a call by industry and investors, to increase standardization of sustainability reporting metrics. Initiated by the World Economic Forum's International Business Council, work is progressing to finalize the development and implementation of set of common 'Stakeholder Capitalism Metrics (SCM)'<sup>27</sup>. It is envisaged that these metrics will assist members of the IBC (and by association any organization desiring to report on ESG performance) to align their mainstream reporting of ESG indicators and track their contributions towards achieving the SDGs. The aligned metrics include 21 core and 34 expanded metrics and disclosures which organizations can adopt. Drawn wherever possible from existing standards and frameworks, these metrics have been grouped under four pillars, namely Principles of Governance, Planet, People, and Prosperity. These efforts are being supported by the leading voluntary ESG framework and standard-setters, who have expressed their intent to cooperate towards achieving a 'single, coherent, global ESG reporting system'.

## What is SAMESG?

The South African guideline for the reporting of environmental, social and governance parameters (SAMESG Guideline) supports the SAMCODES by providing information for authors of Public Reports on how to apply the ESG considerations throughout the geological reporting process. Building on existing frameworks, and in full recognition of the universe of sustainability reporting that already exists, SAMESG seeks to encourage mineral developers listed on the Johannesburg Stock Exchange (JSE) to distil all the information that many are already gathering in support of their voluntary sustainability reporting processes and answer the fundamental question of 'what does this mean for this project?' For junior and mid-tier companies that may not have prepared sustainability reports, SAMESG aims to provide these organizations with guidance on what information investors want to see and how to present it in a manner that best showcases their company's approach to ESG integration. Considering that Mineral Resource and Mineral Reserve reports need to present information at a project level, the SAMESG Guideline is well placed to help address some of the reporting concerns identified internationally, particularly in respect of the lack of available site-level data.

Launched in conjunction with the 2016 versions of the SAMCODES, the SAMESG Guideline resulted from a collaborative process initiated by the SAMCODES Standards Committee (SSC) in 2014 when the development of the guideline was first sanctioned. The Guideline was prepared by a working group comprising a range of environmental, social, and governance specialists from the mining and consulting industries.

Alignment with the SAMESG Guideline requirements in Public Reports prepared by JSE listed companies has been patchy. The Committee has been actively working to broaden its membership base as well as on developing a second version of the Guideline which will take into account developments within the sustainability reporting world since its first publication. The updated Guideline intends to improve the nature and extent of guidance for authors of Public Reports, particularly for the smaller mining companies.

In order to make SAMESG more user-friendly, more applicable to all situations, and more inclusive, the GSSA invites you to take part in our first ESG Inquisition where you will have the opportunity to hear what others think and also to voice your own opinion. The focus of this inquisition is to hear from mining companies and mining practitioners about the challenges they face, the benefits they have found, and what they would like to see in the ESG reporting space.

We expect to run the ESG Inquisition over three days (10-12 August 2021) from 9.00–12.00. Attendance will be FREE, and we want to hear your opinions and experiences (good, bad, or indifferent). If you have a short presentation that you or your company would like to give, please send a proposal to [info@gssa.org.za](mailto:info@gssa.org.za) marked 'ESG Inquisition'. The feedback from this Inquisition will be used to inform the forthcoming SAMESG and SAMREC updates, so your input counts.



*Have you used the SAMESG Guideline? Do you have any feedback that you would like to share with the SAMESG Committee? If so, please use the Contact Us page on [www.samcode.co.za](http://www.samcode.co.za)*

**T. Steele-Schober**

---

<sup>27</sup>World Economic Forum, Measuring stakeholder capitalism: towards common metrics and consistent reporting of sustainable value creation, September 2020



**HEXAGON**

**IDS**  
GeoRadar



**Data Aggregation**



**Critical Slope Monitoring**



**Support and Service**



**Strategic Long-Term Monitoring**



**Rockfall Hazard Mitigation**



**Focused Slope Monitoring**



Via Augusto Righi, 6, 6A, 8  
56121 Pisa, Italy



➔ [www.idsgeoradar.com](http://www.idsgeoradar.com)



# Depositional environment - The original control on gold processing

K.L. Youlton<sup>1</sup>, J.A. Kinnaird<sup>1</sup>, and B.J. Youlton<sup>1,2</sup>

## Affiliation:

<sup>1</sup> School of Geosciences,  
University of the Witwatersrand,  
South Africa

<sup>2</sup> Anglo American Technical  
Solutions, South Africa

## Correspondence to:

K.L. Youlton

## Email:

kyoulton@gmail.com

## Dates:

Received: 2 Jul. 2019

Revised: 29 Mar. 2021

Accepted: 21 Apr. 2021

Published: June 2021

## How to cite:

Youlton, K.L., Kinnaird, J.A., and  
Youlton, B.J. 2021

Depositional environment -  
The original control on gold  
processing.

Journal of the Southern African  
Institute of Mining and Metallurgy,  
vol. 121, no. 6, pp. 267–276.

## DOI ID:

<http://dx.doi.org/10.17159/2411-9717/811/2021>

## ORCID

K.L. Youlton

<https://orcid.org/0000-0001-7833-4471>

J.A. Kinnaird

<https://orcid.org/0000-0001-5879-8324>

## Synopsis

Methods for treating and processing refractory gold ores are well established. However, what is less well understood is how the formation of the gold-bearing deposits affects gold processing and extraction. In order to evaluate the effect of ore genesis on gold extraction a number of South African gold deposits were studied. These included complex Pilgrim's Rest samples as well as refractory Fairview, Barbrook, and Consolidated Murchison samples. We found the refractory nature of gold ores is controlled by a limited number of well-understood mineralogical factors. Solid solution gold is linked to low temperature and pressure conditions in fine-grained sedimentary lithologies, while reactive pyrrhotite can form from hydrothermal fluids associated with mafic magmatic rocks. These formational controls can be used to identify and avoid complex deposits at a desktop study phase, or address and reduce complications further along the pipeline using early mineralogical studies.

## Keywords

gold processing, refractory gold, ore mineralogy.

## Introduction

Gold has been an important commodity throughout much of human history, and is thought to be one of the earliest metals mined (Kongolo and Mwema, 1998; Reardon, 2011). Early gold recovery from stream bed sediments involved manual or gravity-based separation methods; beyond this, little advancement took place until underground mining was initiated in Russia in 1744, where crushing, gravity concentration, and amalgamation were used for gold extraction (Bath and Duncan, 1973; Kongolo and Mwema, 1998; Burt 1999). By 1848, a process to extract gold using chlorine gas was developed and extensively used, but was limited in its capacity to process ore of low grade (Eidem, 1974). Thus, when cyanidation was first patented in 1888, it was rapidly commercialized, first in New Zealand (in 1889) and subsequently in a number of countries including South Africa, the USA, Mexico, and France (Stanley, 1987; Reardon, 2011). The advent of the cyanide process is credited with reviving the failing Witwatersrand gold mining industry in 1890 when the mined ore transitioned from oxidized to sulphidic, with associated copper, lead, iron, and zinc sulphides which prevented effective recovery using amalgamation, the method used on the Witwatersrand prior to cyanidation (Fivaz, 1988).

In recent years there has been a dearth of new gold discoveries. Global gold exploration investment from 2007 to 2016 amounted to US\$65 billion, while the value of gold deposits discoveries in this same period was less than half of this amount (McKeith *et al.*, 2010; Schodde, 2016). Furthermore, in the past 15 years, only an extremely limited number of the discoveries that have been made could be considered world-class (greater than 15 million ounces) (Holmes, 2017). This declining state has forced the gold industry to rely on alternative methods for ensuring sufficient resources and reserves are owned in order to remain competitive and relevant.

Cyanidation is extremely effective at processing more readily extractable/free-milling gold. However, with the diminishing number of orebodies that are both easily accessible and amenable to cyanidation, increasing attention has been given to the discovery and exploitation of refractory ores (Fraser, Walton, and Wells, 1991; Chrystosoulis, Cabri, and Salter, 1987; Hasab, Rashchi, and Raygan, 2014; Vaughan and Kyin, 2004).

Gold deposits occur in a number of different geological settings, only a few of which are host to refractory gold ores. A knowledge of the link between the geological setting of a gold deposit and potential processing problems could be an important factor in the early stages of deposit targeting, an increasingly important phase of exploration. Should it be possible to target geological areas with a higher chance of hosting simple ores, particularly with free-milling gold, it would certainly be

## Depositional environment - The original control on gold processing

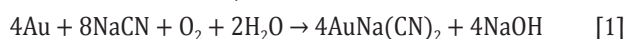
worth factoring this information into early desktop studies. Additionally, understanding the formation and mineralogy and therefore the metallurgical nature of the deposit early in a project will prevent later complications, or at least provide an understanding of the issues likely to arise and act as an early warning of future metallurgical complications.

The present study involved an investigation of selected South African refractory/complex gold deposits, their geological settings, mineralogy, and conditions of metallogenesis, to gain a better understanding of the formation of the complex ores and the causes of processing problems.

### Extractive metallurgy

Gold, a noble metal, is by definition resistant to chemical action, therefore there are a limited number of solvents capable of dissolving it (Moffa, 1977). Effective gold dissolution systems typically require an oxidant capable of oxidizing the gold, as well as a reactant/complexing agent able to form a reasonably stable gold complex post-oxidation (Kongolo and Mwema, 1998; Marsden and House, 2006).

Cyanide has been used in the extraction of gold for over 100 years and the chemistry of its interaction with gold is well understood. Sodium (or potassium) cyanide solution is added to the ground ore in order to dissolve gold. The overall reaction proceeds according to Equation [1] (Kongolo and Mwema, 1998; Marsden and House, 2006):



Oxygen acts as an oxidizing agent, while CN<sup>-</sup> dissociates from sodium and complexes with the gold (Habashi, 1967; McNulty, 1989). Cyanide-gold complexes are significantly more stable than those yielded by alternative lixiviants, making cyanide a useful tool in gold extraction (Chen *et al.*, 1980; Aylmore, 2005, 2016a). This reaction is maintained at a basic pH of approximately 10–11, as this lowers the reduction potential and is the most efficient leaching condition for many ores (Kongolo and Mwema, 1998). Furthermore, at more acidic conditions HCN is evolved, posing a safety concern as well as an economic one due to increased reagent losses (Eisler and Wiemeyer, 2004).

### Refractory ores

The cyanidation reaction typically proceeds quite readily, which accounts for its widespread use. However, its effectiveness is limited in the presence of certain interfering agents. The nature of these agents allows for the classification of gold ores, and while the classification system may vary from author to author (Chryssoulis and McMullen, 2005; Chryssoulis, Cabri, and Salter, 1987; Haque, 1987; Karimi *et al.*, 2010; Komnitsas and Pooley, 1989; Miller, Wan, and Diaz, 2005; Monhemius, 1987; Vaughan, 2004; Zhou and Cabri, 2004) the overall concept is the same. The following description has been strongly based on Vaughan, (2004). Three distinct gold types exist in this system (Figure 1); free milling, complex, and refractory (in increasing order of processing difficulty).

*Free milling ores* encompass all ores that readily yield their gold by cyanidation, with no factors that complicate or reduce extraction efficiency. A gold recovery of 90% or more defines free milling ores (La Brooy, Linge, and Walker, 1994; Marsden and House, 2006).

*Complex ores* refers to ores from which high gold recoveries are possible, but only under modified or more intense leaching conditions. Complex ores can be subdivided into two categories: preg-robbing and reactive. Preg-robbing ores contain material

capable of absorbing gold-cyanide complexes during leaching. This material tends to be carbonaceous matter (specifically elemental and organic carbon), although clays are also thought to have a minor capacity for preg-robbing (Goodall, Leatham, and Scales, 2005; Miller, Wan, and Diaz, 2005; Vaughan, 2004). The effects of preg-robbing can be countered (to a limited degree) in a number of ways: (1) addition of kerosene to deactivate the carbonaceous material, (2) carbon-in-leach, where activated carbon is present throughout the leach and can absorb the gold onto its surface more rapidly than the competing preg-robbing component (La Brooy, Linge, and Walker, 1994; Vaughan, 2004). Reactive ore refers to any ore that contains material that reacts with reagents required for successful gold leaching. These reactive materials tend to be cyanicides (*i.e.* they react with and reduce the available concentration of cyanide) or oxygen consumers. Examples of these minerals include; pyrrhotite, copper minerals (with the exception of chalcopyrite) such as chalcocite, malachite, azurite, and cuprite, as well as most base metal minerals that contain iron, arsenic, antimony, zinc, nickel, and cobalt (Aylmore and Muir, 2001; Karimi *et al.*, 2010). These ores can be dealt with by adding higher concentrations of reagents than would be required for standard cyanidation.

Refractory ores refers to deposits from which acceptable gold recoveries cannot be achieved using standard procedures. There are two types of refractory ores, those with physically and chemically locked gold, both of which make the gold inaccessible to lixiviants. Physically locked gold occurs when gold is present as very fine inclusions, typically within a sulphide mineral. Chemically locked gold can be found in discrete gold minerals such as gold tellurides, aurostibite, aurocupride, and maldonite (Harris, 1990; Vaughan, 2004). Chemically locked gold can also refer to gold present as solid solution within certain minerals; this means that atomic gold is present within crystal lattices (Chryssoulis, Cabri, and Salter, 1987; Haque, 1987; Komnitsas and Pooley, 1989; Monhemius, 1987; Vaughan and Kyin, 2004). Arsenopyrite, and to a lesser extent pyrite, may host solid solution gold (Barker *et al.*, 2009; Vaughan, 2004; Vaughan and Kyin, 2004).

In order to ensure acceptable recoveries from refractory ores, it is usually necessary to implement a pre-treatment step in the extraction process. Examples of pre-treatments include ultrafine milling, pressure oxidation, biological oxidation (BIOX) and in older designs, roasting. Pressure cyanidation, while not a pre-treatment, can also be an effective option (Davis, 1986; Haque, 1987; Lindström, Gunneriusson, and Tuovinen, 1992; Monhemius, 1987).

### Gold deposits

There are a number of important gold deposits in South Africa, accounting for significant gold production in the past and into the present (Janisch, 1986). The Witwatersrand Basin is host to the largest gold deposit in the world, accounting for nearly a third of the world's total gold production (Frimmel, 2005). This deposit will not be discussed further as it is a predominantly free-milling ore and the focus of this study is on refractory type deposits. While refractory deposits in South Africa are relatively small compared to the Witwatersrand Basin, they are still important. The deposits studied were the Fairview and Barbrook mines in the Barberton area, Pilgrim's Rest, and Consolidated Murchison.

### Barberton, Fairview, and Barbrook

The Barberton greenstone belt is one of the oldest and best

## Depositional environment - The original control on gold processing

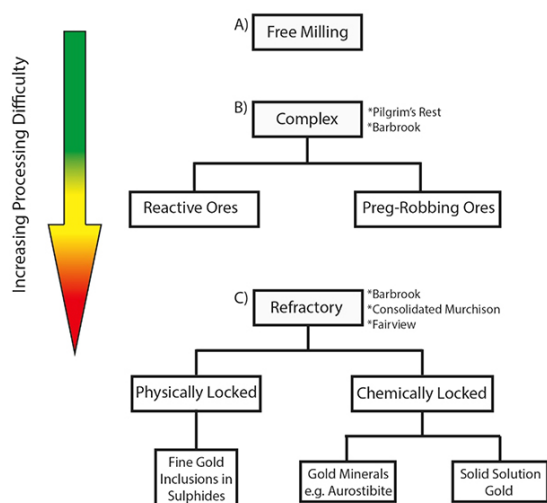


Figure 1—A diagram outlining the three main types of gold deposit: (1) free milling, (2) complex, and (3) refractory. The studied deposits have been grouped with their respective deposit types

preserved supracrustal sequences in the world. The belt occurs near the town of Barberton, Mpumalanga Province, approximately 280 km east of Johannesburg. The mechanism of mineralization is a contentious issue among researchers of this gold district. In the past there was consensus that the mineralization at Barberton had an orogenic genesis, linked to the accretion of the greenstone belt (de Ronde, de Wit, and Spooner, 1994; Goldfarb, Groves, and Gardoll, 2001; Groves *et al.*, 1998). However, a number of more recent papers suggest that the mineralization occurred later than the accretion, and was likely to have been associated with a subsequent extensional event (Dirks, Charlesworth, and Munyai, 2009; Dirks *et al.*, 2013; Munyai, Dirks, and Charlesworth, 2011). Isotope studies suggest that the mineralizing fluids originated from external sources that were probably dominantly magmatic, and migrated upwards through brittle-ductile shear zones, fractures, and faults (de Ronde, de Wit, and Spooner, 1994; Munyai Dirks, and Charlesworth, 2011; Ward, 1999).

### Consolidated Murchison

Consolidated Murchison represents an important antimony–gold deposit within the Murchison greenstone belt, an Archean volcano–sedimentary belt. The deposit is located in the northern Kaapvaal Craton, near Gravelotte, 50 km west of Phalaborwa and 370 km northeast of Johannesburg (Anhaeusser, 2001; Davis, 1986). There has been uncertainty regarding the metallogensis of the Antimony Line, which is host to the mineralization. Models for both syngenetic and epigenetic origins have been proposed. However the complex deformation that has occurred makes accurate studies of this region extremely difficult. The ores appear to be orogenic despite being associated with significant metamorphic remobilization. The simultaneous occurrence of both gold and antimony in their various forms suggests that a single process was responsible for this enrichment (Jaguin *et al.*, 2012; Pearton, 1982).

### Pilgrim's Rest

The Sabie-Pilgrim's Rest gold district is located in Mpumalanga, west of the Drakensberg, approximately 320 km east-northeast of Johannesburg. The Sabie-Pilgrim's Rest orebodies are epithermal deposits, hosted by the Proterozoic Transvaal Supergroup

(Boer *et al.*, 1995). The mineralization is thought to have been contemporaneous with the formation of the Bushveld Complex. The emplacement of such a large volume of magma (450 000 km<sup>3</sup> (Cawthorn and Walraven, 1998; Finn *et al.*, 2015) is likely to have initiated the thrust system that was exploited by the hydrothermal mineralizing fluids that emanated from the intrusion to form this epithermal gold deposit. Isotopic data, fluid inclusion studies, and elemental fingerprints all support the Bushveld Complex as the origin of the fluids (Boer *et al.*, 1995; Meyer and Robb, 1996; Tyler, 1986; Tyler and Tyler, 1996).

As such, the aim of this study is to use the characterization of the refractory ores and their depositional environments to determine the conditions of formation of the refractory deposits in order to apply this information on a larger scale to exploration and remote targeting.

### Methods and materials

The samples used for this study were obtained from the direct feed to the respective processing plants. The sampling took place after coarse crushing but before any other processing was employed. Attempts were made to ensure that the mineralogy was representative of the typical run-of-mine feed from the deposit, as determined by the on-site geologists. The ores were characterized using a combination of chemical assay, optical microscopy, X-ray diffraction (XRD), and Mineral Liberation Analyser (MLA).

### Optical microscopy

As the samples were composites of run-of-mine ore, it was necessary to prepare several thin sections to ensure that the petrological studies were completed on the full range of lithologies. An average of 10 sections from each deposit were prepared directly from the ore, in order to obtain an accurate representation of the respective deposits. The sample surfaces were selected to be as representative as possible, while still including important mineralization features.

### Chemical assay

Gold assays were performed using fire assay and atomic absorption spectroscopy (AAS). X-ray fluorescence (XRF), inductively coupled plasma–mass spectrometry (ICP-MS), and inductively coupled plasma–atomic emission spectroscopy (ICP-AES) were utilized to supplement mineralogical data. XRF provided information regarding the major elements (SiO<sub>2</sub>, Al<sub>2</sub>O<sub>3</sub>), while ICP-MS/AES was used for trace elements (Cu, Ni, Pb, Zn, Sb, *etc.*).

### XRD

The samples were pulverized to ensure the best possible results. Analyses were done using a Co-K $\alpha$  radiation source and a Panalytical X'pert Pro diffractometer.

### Automated scanning electron microscopy

Automated scanning electron microscopy using a MLA (Mineral Liberation Analyser) was performed on comminuted material. The typical grind size recommended for gold leaching is 80% passing 75  $\mu$ m (Marsden and House, 2006), and therefore the sample characterization, particularly the gold, was performed at this grind. The gold grains were mapped using XBSE measurement mode. The MLA instrument was a FEI XL40 ESEM with two EDAX Sapphire Si(Li) EDS detectors. The MLA identification was performed using spectra matching, as is typical for MLA.

## Depositional environment - The original control on gold processing

Several terms are used to describe the data from MLA analyses. The grain sizes are presented in equivalent circular diameter (ECD). Mineral association represents the percentage of the surface area of a certain mineral that is bordered by another. Liberation is the area of the mineral of interest relative to the area of the total host particle, while mineral exposure can be described as the percentage of the grain that has a free, exposed surface.

The number of identified gold grains that were characterized varies with each sample, and therefore the reliability of this characterization may vary. For example, the Barbrook and Consolidated Murchison samples contained slightly fewer than the ideal number of gold grains and therefore the conclusions may be less reliable than those for the Pilgrim's Rest, and Fairview samples.

### Results – deposit mineralogy

#### Fairview, Barberton

The mineralization at Barberton is hosted by a highly altered lithology comprising lithic quartz fragments, with a notable alignment, within a finer-grained matrix of chlorite, dolomite,

magnesite, and to a lesser extent muscovite. Ore minerals are present either in veins/fractures, where the grains tend to be large and euhedral, or as disseminations throughout the whole rock, where they tend to be fine and sub- to anhedral. These minerals include pyrite, arsenopyrite, and minor visible gold (Figure 2A). Gold grades in the studied material are close to 12.5 g/t (Table I) and this high grade is reflected in the gold particle count (Table II). At a grind of 80% –75 µm, visible native gold was 99.7% liberated, with a surface exposure/leach reactivity of 99.7%. Gold grains range in size from 0.5 µm to 425 µm (Figure 3A), with the most significant contribution to the total gold weight percentage in the range of 180 µm to 425 µm. The large range in grain size, as well as the presence of coarse gold, will affect the leach time. Minerals commonly associated with the gold include pyrite (3.8%), arsenopyrite (3.3%), and quartz (0.9%) (Figure 2B). The discrepancy between the visible gold content and the high grade (12.5 g/t Au) suggests that there is gold that is invisible to both optical petrology and MLA. Based on previous characterizations of the ore, this is likely to be due to solid solution gold present within arsenopyrite (Anhaeusser, 2001, 2015).

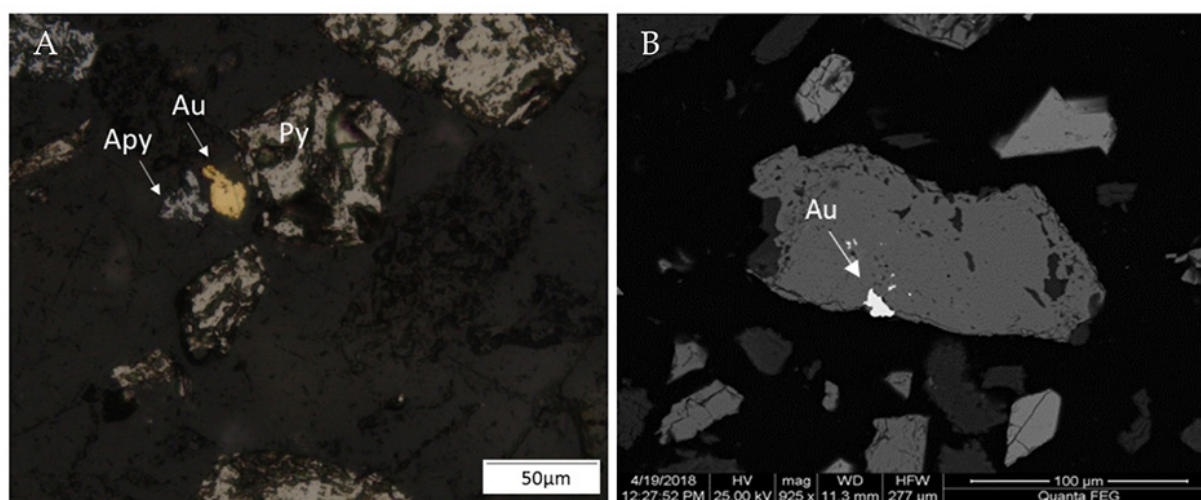


Figure 2—Typical mineralization found at Fairview. (A) Reflected light image of ores including arsenopyrite (Apy), pyrite (Py), and gold (Au). The gold grain has an equivalent circular diameter (ECD) of 46.5 µm. (B) BSE image of gold included within pyrite, resulting in limited liberation, moderate exposure, and an ECD of 10.7 µm

Table I

#### Chemical assay data, including gold grades and potentially deleterious elements

Sample	Au (g/t)	S (%)	C (%)	Org. C (%)	As (%)	Cu (ppm)	Fe (%)	Co (ppm)	Ni (ppm)	Sb (ppm)	Zn (ppm)	Pb (ppm)
Fairview	12.5	2.86	1.27		0.81	84		50	491		124	<20
Barbrook	2.08	8.06	3.94	0.23	0.23	597	15.3	-	472	65	2330	579
Consolidated Murchison	3.04	6.29	3.55	0.13	2.96	164	10.2	-	700	70100	98	87
Pilgrim's Rest	29.4	29.6	0.7	0.14	0.35	7230	25.5	-	84	931	47	108

Table II

#### Grain and particle count used to characterize the samples

Sample	Native gold			Aurostibite			
	Particles	Grains	Au (%)	Particles	Grains	Au (%)	Total gold-bearing grains
Fairview	224	321	100	-	-	-	321
Barbrook	47	50	100	-	-	-	50
Consolidated Murchison	22	23	37.2	44	44	62.8	67
Pilgrim's Rest	156	169	100	-	-	-	169

## Depositional environment - The original control on gold processing

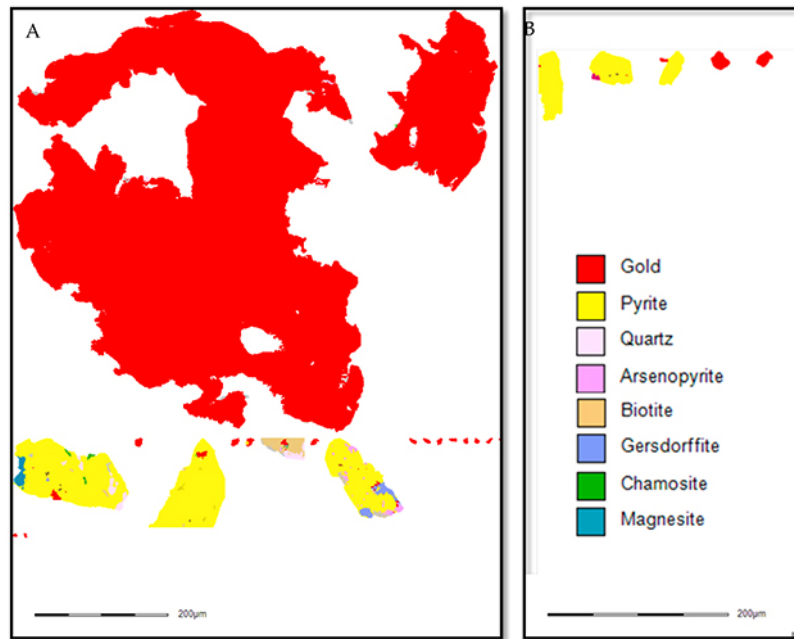


Figure 3—False colour image of gold grains generated from MLA data. (A) The Fairview sample shows a vast range in the sizes of gold grains associated with pyrite, where gold is represented in red. (B) The Barbrook gold is much finer-grained but is also associated with pyrite

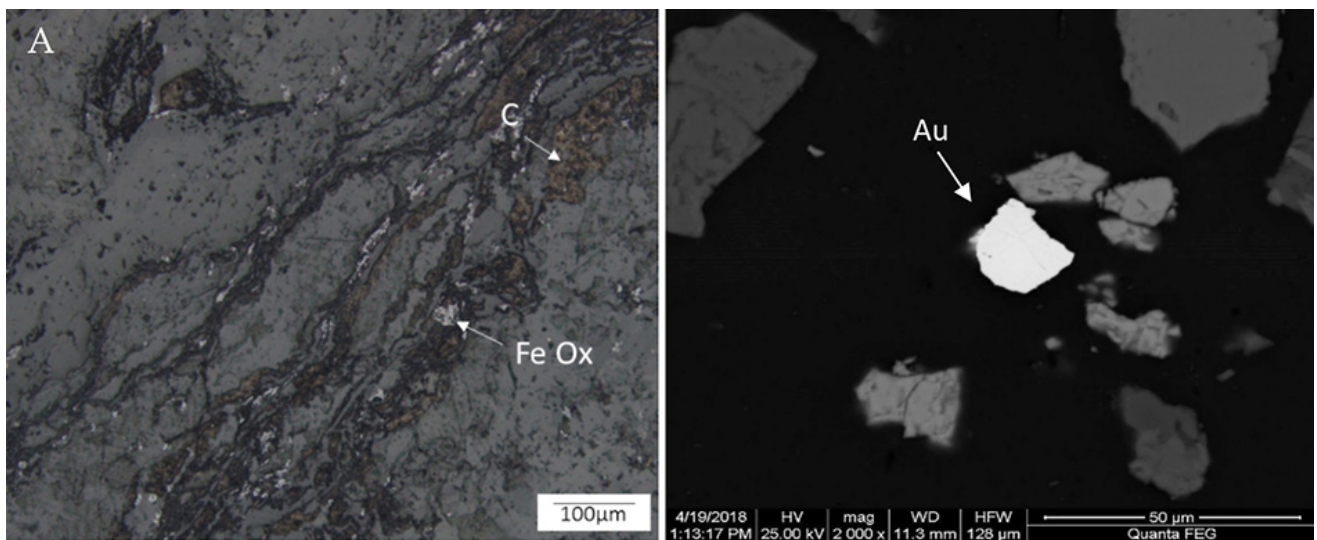


Figure 4—Barbrook samples. (A) The gold is too fine-grained to be visible in this reflected light image, but the associated deleterious occurrence of abundant iron oxide and particulate carbon is clear. (B) BSE image of one of the larger Barbrook gold grains found using the MLA (BSE image) with an ECD of 16.9 µm

### Barbrook, Barberton

The host lithology tends to be a highly altered carbonate-rich shale composed of quartz, dolomite, chlorite, muscovite, and carbon. Accessory iron-rich minerals range from highly abundant to entirely absent; secondary iron oxides such as limonite and goethite are also present (Figure 4A). Extensive veins are dominantly of carbonate and lesser quartz, with a range of orientations resulting in a stockwork texture. Ore minerals include pyrite, arsenopyrite, and minor chalcocite, galena, and pyrrhotite. Only a limited number of gold grains were identified using MLA (Figures 4B, 3B) and these ranged in size from 1 µm to 20 µm. The gold tends to be associated only with pyrite (10.0%), which is unlikely to significantly affect leaching conditions. A comparison of assayed (Table I) and mineralogically

calculated gold grades suggests that 40% of the gold is present as solid solution in arsenopyrite, a feature also commented on by Anhaeusser (2001) and Pearton and Viljoen (2017).

### Consolidated Murchison

The mineralization at Consolidated Murchison is hosted by altered schists, consisting predominantly of carbonate and quartz with lesser chlorite, biotite, and magnesite and locally abundant tourmaline. Ore minerals present include stibnite ( $Sb_2S_3$ ), pyrite, berthierite ( $FeSb_2S_4$ ), and lesser arsenopyrite (Figure 5A). Gold tends to be disseminated homogeneously throughout the schist with grain sizes ranging from 2 µm to 32 µm. Assays confirm a grade of 3 g/t (Table I), and this low grade is reflected in the number of gold grains located and identified. The MLA results

## Depositional environment - The original control on gold processing

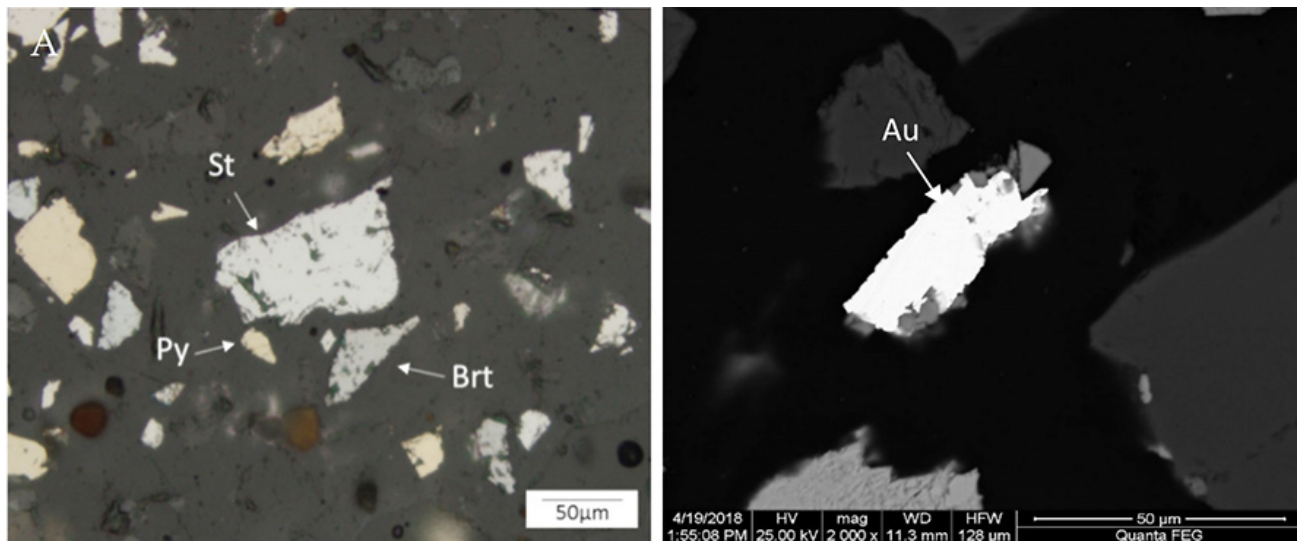


Figure 5—Ore minerals in Consolidated Murchison sample. (A) Shown in reflected light, stibnite (St), pyrite (Py) and berthierite (Brt) in an altered shale matrix which appears as dull grey in reflected light. (B) The gold grain is well liberated and exposed, with an ECD of 25.5 µm

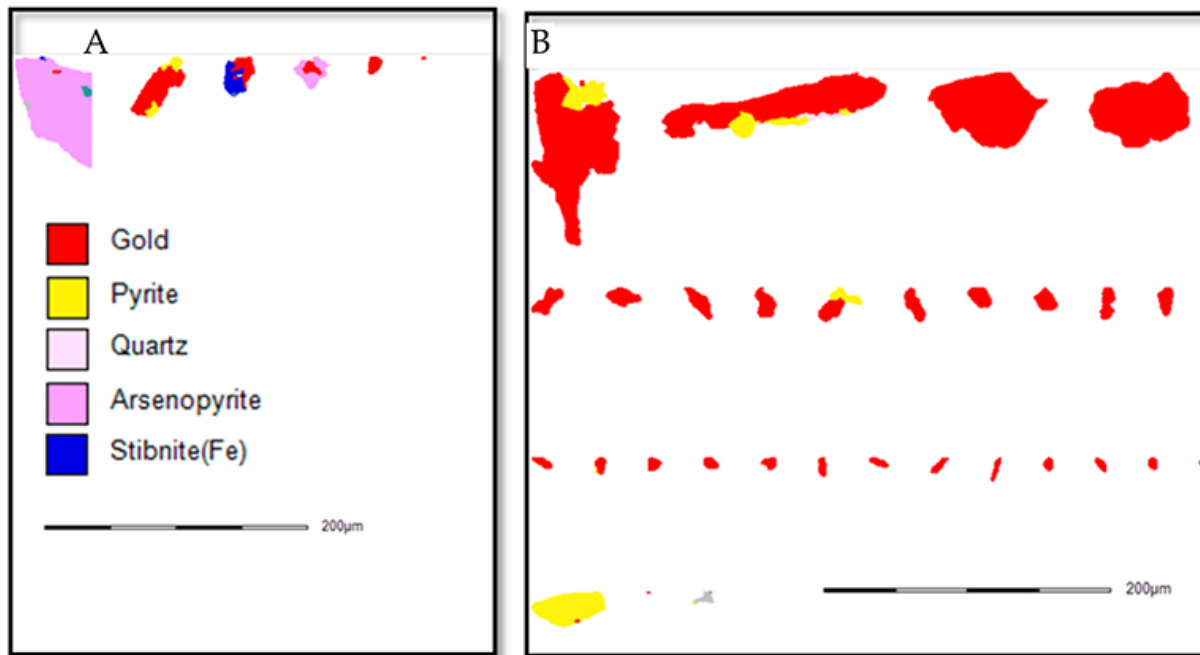


Figure 6—False colour image of gold grains generated from MLA data. (A) Consolidated Murchison gold grains, highlighting both the paucity of native gold grains and the low degree of liberation. (B) Gold grains derived from the Pilgrim's Rest sample, showing the range in grain size and the excellent liberation and exposure

suggest that the gold is less liberated (71.9%) than in the other samples investigated (Figure 6A); however, 91.3% of the gold is available/exposed for leaching (Figure 5B). Accessory minerals include arsenopyrite (15.7%), pyrite (13.6%), and stibnite (11.6%). The association of the gold and gold-bearing minerals with antimony-rich minerals such as stibnite will affect the leaching potential, due to both reagent consumption and passivation. The limited presence of native gold suggests that in addition to the coarse free grains and aurostibite, gold is also present in solid solution in arsenopyrite and aurostibite (Davis, 1986; Marsden and House, 2006; Vearncombe *et al.*, 1988).

### Pilgrim's Rest

The host lithology is predominantly a fine-grained shale

composed of quartz and fine-grained micas, crosscut by quartz-carbonate veins ranging from millimetres to metres in width. Within the veins, sulphides occur both as disseminations and massive mineralization. Gold occurs as discrete, fine grains, ranging in size from 1.5 µm to 75 µm (Figure 6B). The sulphides are dominated by abundant pyrite, representing approximately one third, by mass, of the feed, with lesser pyrrhotite (Figure 7A), chalcocite, and chalcopyrite, together with the native gold (Figure 7B). Assay results show high concentrations of both gold (29.4 g/t) and copper (7230 ppm) (Table I). While previous data suggests that a significant proportion of the gold in this ore is typically less than 5 µm in size (Swiegers, 1948), the contribution of gold in this size range to the overall weight percentage was found to be insignificant. Rather more than

## Depositional environment - The original control on gold processing

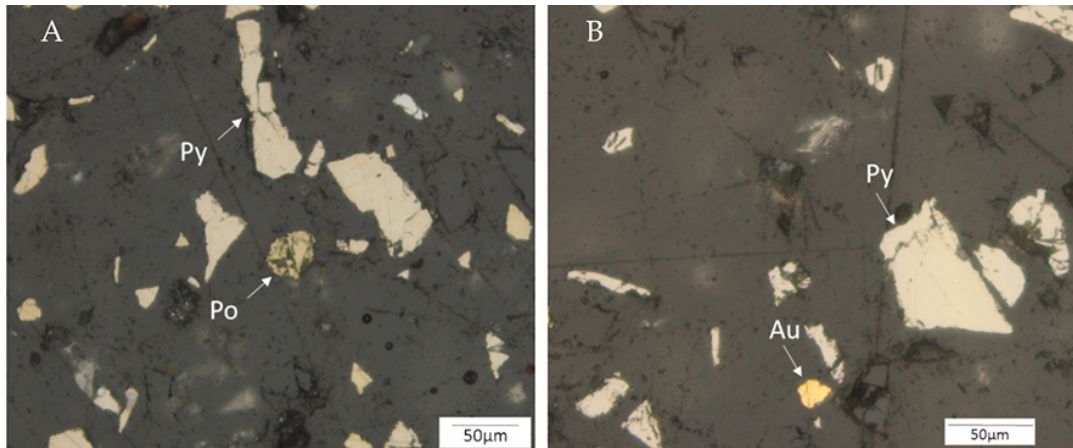


Figure 7—Pilgrim's Rest material imaged in reflected light. (A) Typical field of view showing the abundant pyrite (py) and deleterious pyrrhotite (po). (B) A gold grain with an equivalent circular diameter of 16 µm, with significant accessory pyrite also evident

85 wt% of the gold was in grains between 10 µm and 75 µm size. Gold mineral associations include pyrite and quartz, which are unlikely to affect the gold extraction.

### Discussion

Gold deposits occur in a number of different geological settings. Deposits such as those of Barberton are associated with short-term tectonic extension following a period of mountain building (de Ronde, 1994; Dirks *et al.*, 2013) while others formed from hydrothermal fluids associated with the intrusion of basaltic/mafic magma, such as at Pilgrim's Rest (Boer *et al.*, 1995). Other deposits are entirely hosted in sedimentary rocks, such as the Carlin type deposits in Nevada (Cline *et al.*, 2005), while high-sulphidation epithermal gold deposits are formed at shallow crustal levels associated with volcanic activity. However, some deposit types are more likely to be refractory than others. Examples of deposits that are more likely to be free milling include placer and low-sulphidation epithermal systems (volcanic-related mineralization). Conversely, Carlin (disseminated, sedimentary-hosted), high-sulphidation epithermal and, important to this study, atypical greenstone deposits of disseminated stockwork type, tend to be refractory (Rowe, 2007).

In this study we have identified a number of factors that are likely to affect the successful extraction of gold from certain types of deposit, depending on both the gangue phases and the nature of the gold occurrence. The processing procedures for each deposit have been adapted to account for these factors.

The Fairview ore is refractory as the gold is sulphide-hosted. During processing the sulphides are destroyed using biological oxidation (BIOX) prior to leaching. No deleterious effects are encountered from the quartz, chlorite, or dolomite that comprise the dominant minerals of the host rock.

The Barbrook ore is refractory/complex due to the coexistence of sulphide-hosted gold and preg-robbing carbon. The ore therefore undergoes a series of flotation steps in order to concentrate the gold-bearing sulphides. The sulphide concentrate is subjected to ultrafine milling and pressure oxidation, which releases the gold and allows effective leaching. Cyanidation is then undertaken with the gold loading onto resin-in-leach in order to reduce preg-robbing effects (Grant, 2004). At a grind size of 80% of -75 µm the visible gold observed had excellent

liberation and exposure, so any increased grinding would have a negligible positive impact on the gold recovery.

The Consolidated Murchison ore contains antimony which, during gold extraction, is thought to act as an oxygen scavenger (Monhemius, 1987), while increasing both cyanide and lime consumption. There is also evidence that the gold becomes passivated in the presence of antimony sulphides during normal cyanidation (Millard, 2005; Rohner and Millard, 2016). Gold extraction at Consolidated Murchison involves first separating out free gold using gravity concentration. The remaining ore is then subjected to flotation, concentrating both gold and stibnite. The gold is subsequently recovered from the flotation concentrate using a low-alkalinity, high-pressure (8.8 MPa) cyanidation process in a 1.5 km pressure pipe reactor (Davies and Paterson, 1986; Millard, 2005).

The Pilgrim's Rest ore shows no evidence of refractory gold. In addition, the excellent liberation and exposure would suggest that this ore is well disposed to cyanide leaching. However, significant copper concentrations (0.7%) adversely affect leaching, as copper competes with gold to form cyanide complexes (Deschênes and Prud'homme, 1997). In addition, the Pilgrim's Rest ore has notable quantities of pyrrhotite, which can consume cyanide and reduced leaching kinetics (Dai and Jeffrey, 2006). Due to the complex mineralogical components of Pilgrim's Rest ore, flotation and roasting are employed prior to cyanidation.

The key mineralogical components identified as responsible for the refractory nature of the deposits of interest include solid-solution gold, preg-robbing carbon, and reactive minerals (Figure 8). Their origins can be better constrained by understanding the genesis of these deposits.

Large proportions of the gold at Fairview and Barbrook are present within the crystal lattice of arsenopyrite. Submicroscopic gold is thought to be incorporated into the crystal lattices during mineralization at sub- to lower greenschist facies conditions. As indicated in Figure 8, with an increase in metamorphic (PT) conditions, the gold is progressively ejected from the lattice, first into fractures and occlusions within the sulphides and finally into discrete minerals within the gangue (Vaughan and Kyin, 2004). However, most of the orogenic belts in South Africa have undergone only low-grade/greenschist metamorphism. Consequently, the gold has largely remained within the arsenopyrite, resulting in the refractory nature of

## Depositional environment - The original control on gold processing

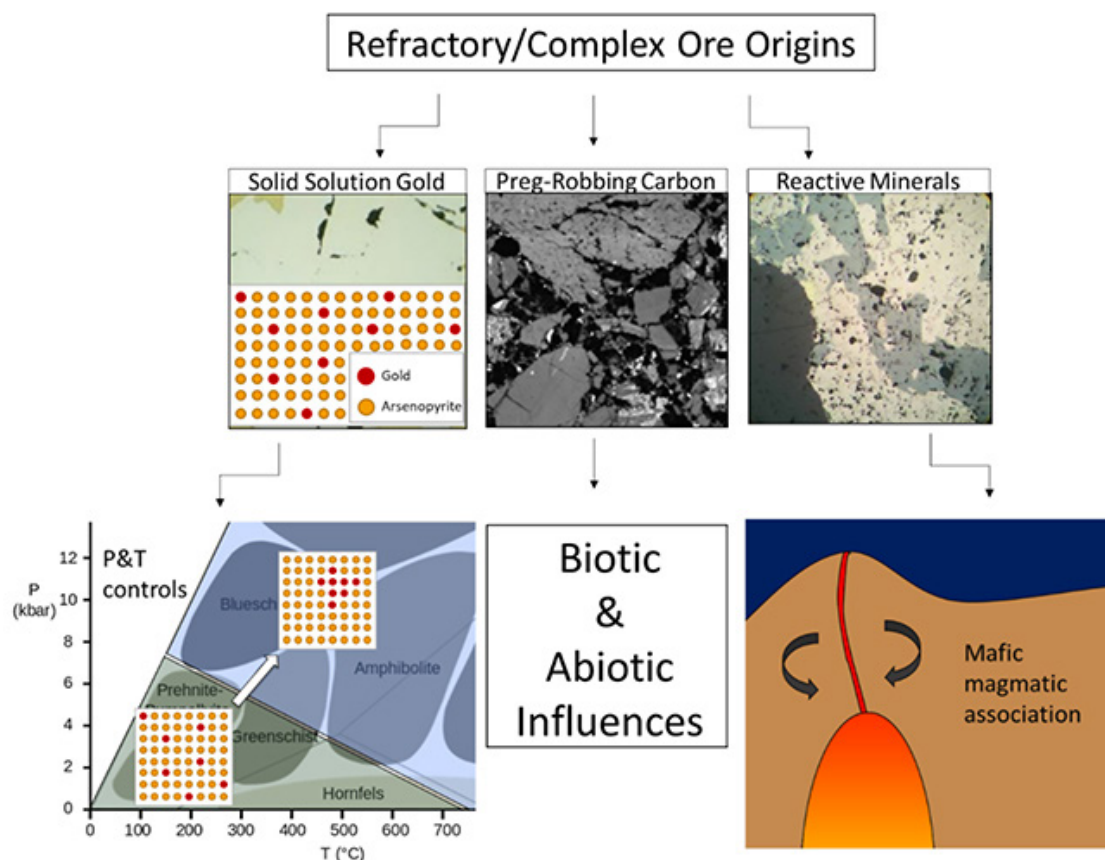


Figure 8—A schematic diagram showing the key components responsible for the refractory nature of gold deposits and some factors that influence this. Increasing metamorphic grade causes the gold in the arsenopyrite crystal lattice to be ejected, while both biotic and abiotic factors are responsible for the formation and preservation of preg-robbing carbon. A deposit associated with mafic magmatic fluids would likely contain reactive pyrrhotite

orogenic gold deposits that are characterized by low-temperature metamorphism (Foster and Piper, 1993). Other orogenic lode gold deposits that have undergone only low-grade metamorphism can also be expected to be refractory. This means that mineralogical assessments of potential deposits in these regions should be prioritized, in order to determine gold occurrence and prevent unexpected processing complications.

Arsenic tends to be enriched within sedimentary, rather than igneous, lithologies. The arsenic concentration in metamorphic units is strongly dependant on the original protolith, and arsenic is not significantly enriched during metamorphism (Tanaka, 1988). Arsenic enrichment in sedimentary material is thought to take place during the sedimentation process, with finer grained sediments typically having higher As concentrations (Tanaka, 1988). Thus gold-bearing provinces hosted in fine-grained sedimentary lithologies are more likely to be enriched in arsenic than other gold deposit types, and assays performed on this type of ore should include arsenic.

Antimony is another element with deleterious effects, typified by the Consolidated Murchison ore in this study. The mechanisms that constrain antimony concentration globally are not well understood, although a series of analyses on samples from various lithologies and localities indicated that antimony enrichment occurs in sediments (notably shales and argillites), as well as andesites and rhyolites (Boyle and Jonasson, 1984). The original rock types at Consolidated Murchison were a mix of volcanic and sedimentary units that later underwent metamorphism. The metasedimentary nature of

the sample studied accounts for the arsenic enrichment. While these conditions of formation may not be well constrained, the inclusion of antimony in early assays for prospects with relevant lithologies (shales, argillites, andesites, and rhyolites) would be a simple and cheap method of identifying potential processing complications relating to antimony.

Potentially preg-robbing carbonaceous components may originate from both biotic and abiotic factors (Welte, 1969). Examples of factors that control the formation and preservation of preg-robbers include initial presence and oxygen availability (both of which may vary on a scale of metres), iron concentration, burial rate, and subsequent metamorphism (Meyers, 2007; Pedersen and Calvert, 1990; Welte, 1969). The variability of factors is emphasized by the contrasting examples of Fairview and Barbrook. While these economic gold deposits formed in the same vicinity, at the same time, from the same mineralizing events and in the same stratigraphic units, they have distinctly different carbonaceous natures. For this reason the occurrence of preg-robbing carbon cannot be readily constrained based on the conditions of deposit formation and as such would need to be evaluated for each deposit of interest. Fortunately, there are highly effective methods of addressing the occurrence of preg-robbing carbon during processing.

Pyrrhotite, one of the most common base metal minerals in complex gold ores, can increase cyanide consumption and reduce leaching kinetics. Primary pyrrhotite forms predominantly in mafic to ultramafic intrusions, which do not typically host primary gold deposits. However, hydrothermal fluids from these

## Depositional environment - The original control on gold processing

intrusions are also commonly responsible for pyrrhotite formation (Gordon and McDonald, 2015; Vaughn, 1982). Hydrothermal deposits are the most widespread type on Earth and the hydrothermal fluids from which pyrrhotite precipitated are often a mix of magmatic, metamorphic, or diagenetic fluids (Reed and Palandri, 2006). However, where the hydrothermal fluids can be linked to an original mafic magmatic source, as typified by Pilgrim's Rest (Figure 8), it is a good indication of the potential for processing complexities.

### Conclusion

Several mineralogical features of gold ores can cause processing complications. The study of four complex/refractory deposits in South Africa highlighted several of these features: gold locked within arsenopyrite, preg-robbing carbon, reactive minerals such as pyrrhotite, and antimony-bearing phases. From this study it is possible to determine what features of deposit formation were responsible for these complicating mineralogical components. Solid-solution gold is linked to mineralization in regions that have experienced only low pressure and temperature conditions and are hosted in fine-grained sedimentary units. Reactive pyrrhotite will be present in gold deposits associated with hydrothermal fluids emanating from mafic magmatism.

Desktop studies and remote targeting are increasingly important steps in gold exploration, and the conditions in which complex deposits form could be readily incorporated into this approach, which could enable the selective targeting of free-milling/readily extractable deposits, reducing complications and expenses throughout the gold recovery process. Should it not prove possible to avoid these complex deposits entirely, these conditions of formation may act as a warning system to allow for mineralogical and metallurgical considerations early in the project pipeline.

### Acknowledgments

The support of the DST-NRF Centre of Excellence for Integrated Mineral and Energy Resource Analysis (DSI-NRF CIMERA) towards this research is hereby acknowledged. Opinions expressed and conclusions arrived at are those of the authors and are not necessarily to be attributed to the CoE. The authors would also like to express their gratitude to Bradley Guy for his invaluable technical assistance.

### References

- ANHAEUSSER, C.R. 2015. The stratigraphy, structure, and gold mineralization of the Jamestown and Sheba Hills areas of the Barberton Mountain Land. PhD thesis, University of the Witwatersrand, Johannesburg.
- ANHAEUSSER, C.R. 2001. Barberton Greenstone Belt. Economic Geology Research Unit, University of the Witwatersrand.
- AYLMORE, M.G. and MUIR, D.M. 2001. Thiosulfate leaching of gold—a review: *Minerals Engineering*, vol. 14. pp. 135–174.
- BARKER, S.L., HICKEY, K.A., CLINE, J.S., DIPPLE, G.M., KILBURN, M.R., VAUGHAN, J.R., and LONGO, A.A. 2009. Uncloaking invisible gold: Use of nanoSIMS to evaluate gold, trace elements, and sulfur isotopes in pyrite from Carlin-type gold deposits: *Economic Geology*, vol. 104. pp. 897–904.
- BATH, E.R. and DUNCAN, A.J. 1973. Some factors influencing gold recovery by gravity concentration. *Journal of the South African Institute of Mining and Metallurgy*, vol. 73, no. 11. pp. 363–384.
- BOER, R., MEYER, F., ROBB, L., GRANEY, J., VENNEMANN, T., and KESLER, S. 1995. Mesothermal-type mineralization in the Sabie-Pilgrim's Rest gold field, South Africa. *Economic Geology*, vol. 90. pp. 860–876.
- BOYLE, R. and JONASSON, I. 1984. The geochemistry of antimony and its use as an indicator element in geochemical prospecting. *Journal of Geochemical Exploration*, vol. 20. pp. 223–302.
- BURT, R. 1999. The role of gravity concentration in modern processing plants. *Minerals Engineering*, vol. 12, no. 11. pp. 1291–1300.
- CHRYSOULIS, S. and McMULLEN, J. 2005. Mineralogical investigation of gold ores. *Developments in Mineral Processing*, vol. 15. pp. 21–71.
- CHRYSOULIS, S.L., CABRI, L.J., and SALTER, R.S. 1987. Direct determination of invisible gold in refractory sulphide ores. *Proceedings of the Metallurgical Society of the Canadian Institute of Mining and Metallurgy*. Pergamon, Oxford. pp. 235–244.
- CLINE, J.S., HOFSTRA, A.H., MUNTEAN, J.L., TOSDAL, R.M. and HICKEY, K.A. 2005. Carlin-type gold deposits in Nevada: Critical geologic characteristics and viable models. *Economic Geology 100th Anniversary Volume*. pp. 451–484. doi:10.5382/av100.15
- CONGRESS, C.M.a.M. 1961. Notes dealing with the geology, mineralogy, mining, metallurgy and history of Pilgrims Rest, with particular reference to the Transvaal Gold Mining Estates, Limited. Presented to the 7th Commonwealth Mining and Metallurgical Congress, April 1961. Historical Papers Research Archive, University of the Witwatersrand. Ref. A1270f. 8 pp. Mimeog.
- DAI, X., BREUER, P., and JEFFREY, M. 2010. Comparison of activated carbon and ion-exchange resins in recovering copper from cyanide leach solutions. *Hydrometallurgy*, vol. 101. pp. 48–57.
- DAI, X. and JEFFREY, M.I. 2006. The effect of sulfide minerals on the leaching of gold in aerated cyanide solutions. *Hydrometallurgy*, vol. 82. pp. 118–125.
- DAVIES, D.R. and PATERSON, D.B. 1986. Practical implementation of low alkalinity pressure cyanidation leaching techniques for the recovery of gold from refractory flotation concentrates. *Gold 100. Proceedings of the International Conference on Gold*: Vol. 2. Wagner, H. (ed.). South African Institute of Mining and Metallurgy, Johannesburg. pp. 591–604.
- DAVIS, D. 1986. Antimony in South Africa. *Journal of the South African Institute of Mining and Metallurgy*, vol. 86. pp. 173–193.
- DE RONDE, C.E., DE WIT, M.J., and SPOONER, E.T. 1994. Early Archean (> 3.2 Ga) Fe-oxide-rich, hydrothermal discharge vents in the Barberton greenstone belt, South Africa: *Geological Society of America Bulletin*, vol. 106. pp. 86–104.
- DESCHÈNES, G. and PRUD'HOMME, P. 1997. Cyanidation of a copper-gold ore. *International Journal of Mineral Processing*, vol. 50. pp. 127–141.
- DIRKS, P., CHARLESWORTH, E., and MUNYAI, M. 2009. Cratonic extension and Archean gold mineralisation in the Sheba-Fairview mine, Barberton Greenstone Belt, South Africa. *South African Journal of Geology*, vol. 112. pp. 291–316.
- DIRKS, P.H., CHARLESWORTH, E.G., MUNYAI, M.R., and WORMALD, R. 2013. Stress analysis, post-orogenic extension and 3.01 Ga gold mineralisation in the Barberton Greenstone Belt, South Africa. *Precambrian Research*, vol. 226. pp. 157–184.
- EIDEM, I. and L. LUNDEVALL. 1974. Chlorine - Glimpses from its history. *Proceedings of the Chlorine Bicentennial Symposium*. The Electrochemical Society, Princeton, NJ.
- FIVAZ, C.E. 1988. Presidential Address: How the MacArthur-Forrest cyanidation process ensured South Africa's golden future. *Journal of the South African Institute of Mining and Metallurgy*, vol. 88, no. 9. pp. 309–318.
- FOSTER, R. and PIPER, D. 1993. Archean lode gold deposits in Africa: Crustal setting, metallogenesis and cratonization. *Ore Geology Reviews*, vol. 8. pp. 303–347.
- FRASER, K., WALTON, R., and WELLS, J. 1991. Processing of refractory gold ores. *Minerals Engineering*, vol. 4. pp. 1029–1041.
- GOLDFARB, R., GROVES, D., and GARDOLL, S. 2001. Orogenic gold and geologic time: A global synthesis. *Ore Geology Reviews*, vol. 18. pp. 1–75.
- GOODALL, W.R., LEATHAM, J.D., and SCALES, P.J. 2005. A new method for determination of preg-robbing in gold ores. *Minerals Engineering*, vol. 18. pp. 1135–1141.

## Depositional environment - The original control on gold processing

- Gordon, S.C. and McDonald, A.M. 2015. A study of the composition, distribution, and genesis of pyrrhotite in the Copper Cliff offset, Sudbury, Ontario, Canada. *Canadian Mineralogist*, vol. 53. pp. 859–878.
- GRANT, D. 2004. Barbrook Mines Limited, Mpumalanga Province, South Africa. Independent Qualified Person's Report. <https://www.caledoniamining.com/wp-content/uploads/2019/02/barbTechFull.pdf>
- GROVES, D.I., GOLDFARB, R.J., GEBRE-MARIAM, M., HAGEMANN, S., and ROBERT, F. 1998. Orogenic gold deposits: a proposed classification in the context of their crustal distribution and relationship to other gold deposit types. *Ore Geology Reviews*, vol. 13. pp. 7–27.
- HABASHI, F. 1967. Kinetics and mechanism of gold and silver dissolution in cyanide solution. *Geological Bulletin*, no. 59. Montana Bureau of Mines. 42 pp.
- HAQUE, K. 1987. Gold leaching from refractory ores—Literature survey. *Mineral Processing and Extractive Metallurgy Review*, vol. 2. pp. 235–253.
- HARRIS, D. 1990. The mineralogy of gold and its relevance to gold recoveries. *Mineralium Deposita*, vol. 25. pp. 53–57.
- HASAB, M.G., RASHCHI, F., and RAYGAN, S. 2014. Chloride-hypochlorite leaching and hydrochloric acid washing in multi-stages for extraction of gold from a refractory concentrate. *Hydrometallurgy*, vol. 142. pp. 56–59.
- JAGUIN, J., POUJOL, M., BOULVAIS, P., ROBB, L., and PAQUETTE, J.-L. 2012. Metallogeny of precious and base metal mineralization in the Murchison Greenstone Belt, South Africa: Indications from U–Pb and Pb–Pb geochronology. *Mineralium Deposita*, vol. 47. pp. 739–747.
- JANISCH, P.R. 1986. Gold in South Africa. *Journal of the South African Institute of Mining and Metallurgy*, vol. 86. pp. 273–316.
- KARIMI, P., ABDOLLAHI, H., AMINI, A., NOAPARAST, M., SHAFAEI, S., and HABASHI, F. 2010. Cyanidation of gold ores containing copper, silver, lead, arsenic and antimony. *International Journal of Mineral Processing*, vol. 95. pp. 68–77.
- KISSIN, S. and SCOTT, S. 1982. Phase relations involving pyrrhotite below 350 degrees C. *Economic Geology*, vol. 77. pp. 1739–1754.
- KOMNITSAS, C. and POOLEY, F.D. 1989. Mineralogical characteristics and treatment of refractory gold ores. *Minerals Engineering*, vol. 2. pp. 449–457.
- KONGOLO, K. and MWEMA, M. 1998. The extractive metallurgy of gold. *Hyperfine Interactions*, vol. 111. pp. 281–289.
- LA BROOY, S., LINGE, H., and WALKER, G. 1994. Review of gold extraction from ores. *Minerals Engineering*, vol. 7. pp. 1213–1241.
- LINDSTRÖM, E.B., GUNNERIUSSON, E., and TUOVINEN, O.H. 1992. Bacterial oxidation of refractory sulfide ores for gold recovery. *Critical Reviews in Biotechnology*, vol. 12. pp. 133–155.
- MARSDEN, J. and HOUSE, I. 2006. *The Chemistry of Gold Extraction*. Ellis Horwood, Chichester.
- McNULTY, T. 1989. A metallurgical history of gold. *Proceedings of the American Mining Congress*, San Francisco, September 1989.
- MEYER, F. and ROBB, L. 1996. The geochemistry of black shales from the Chuniespoort Group, Transvaal sequence, eastern Transvaal, South Africa. *Economic Geology*, vol. 91. pp. 111–121.
- MEYERS, S.R. 2007. Production and preservation of organic matter: The significance of iron. *Paleoceanography*, vol. 22, no. 4. <https://doi.org/10.1029/2006PA001332>
- MILLARD, M. 2005. Treatment of antimonial gold ores. *Developments in Mineral Processing*, vol. 15. pp. 985–991.
- MILLER, J., WAN, R.-Y., and DIAZ, X. 2005. Preg-robbing gold ores. *Developments in Mineral Processing*, vol. 15. pp. 937–972.
- MOFFA, J. 1977. Physical and mechanical properties of gold and base metal alloys. *Proceedings of Alternatives to Gold Alloys in Dentistry*. Valega, T.M. (ed.). US Department of Health, Education, and Welfare, Public Health Service, National Institutes of Health.
- MONHEMIUS, A. 1987. Recent advances in the treatment of refractory gold ores. *Proceedings of the II Meeting of the Southern Hemisphere on Mineral Technology*, Rio de Janeiro. <http://www.imperial.ac.uk/respub/MONHEMIUS-1987-644335.ris>
- MUNYAI, M., DIRKS, P., and CHARLESWORTH, E. 2011. Archaean gold mineralisation during post-orogenic extension in the new consort gold mine, Barberton Greenstone Belt, South Africa. *South African Journal of Geology*, vol. 114. pp. 121–144.
- PEARTON, T. 1982. Gold and antimony mineralization in altered komatiites of the Murchison greenstone belt, South Africa. *Komatiites*. George Allen and Unwin, London. pp. 459–475.
- PEARTON, T. and VILJOEN, M. 2017. Gold on the Kaapvaal Craton, outside the Witwatersrand Basin, South Africa. *South African Journal of Geology*, vol. 120. pp. 101–132.
- PEDERSEN, T. and CALVERT, S. 1990. Anoxia vs. productivity: What controls the formation of organic-carbon-rich sediments and sedimentary rocks? *AAPG Bulletin*, vol. 74. pp. 454–466.
- REARDON, A.C. 2011. *Metallurgy for the Non-metallurgist*. ASM International, Materials Park, OH.
- REED, M.H. and PALANDRI, J. 2006. Sulfide mineral precipitation from hydrothermal fluids. *Reviews in Mineralogy and Geochemistry*, vol. 61. pp. 609–631.
- ROHNER, P. and MILLARD, M. 2016. Treatment of antimonial gold ores. *Gold Ore Processing*. 2nd edn. Elsevier. pp. 927–933.
- ROWE, R. and ZHOU, X. 2007. Models and exploration methods for major gold deposit types. *Proceedings of Exploration*, vol. 7. p. 691–711.
- STANLEY, G.G. 1987. *The Extractive Metallurgy of Gold in South Africa*. vol. 7. South African Institute of Mining and Metallurgy, Johannesburg.
- SWIEGERS, J. 1948. The gold deposits of the Pilgrims Rest gold mining district, Transvaal. *South African Journal of Geology*, vol. 51. pp. 81–132.
- Tanaka, T. 1988. Distribution of arsenic in the natural environment with emphasis on rocks and soils. *Applied Organometallic Chemistry*, vol. 2. pp. 283–295.
- TYLER, N. 1986. The origin of gold mineralization in the Pilgrim's Rest Goldfield, Eastern Transvaal. *Information Circular* no. 179. Economic Geology Research Unit, University of the Witwatersrand.
- TYLER, R. and TYLER, N. 1996. Stratigraphic and structural controls on gold mineralization in the Pilgrim's Rest goldfield, eastern Transvaal, South Africa. *Precambrian Research*, vol. 79. pp. 141–169.
- VAUGHAN, J. 2004. The process mineralogy of gold: The classification of ore types. *JOM*, vol. 56. pp. 46.
- VAUGHAN, J. and KYIN, A. 2004. Refractory gold ores in Archaean greenstones, Western Australia: Mineralogy, gold paragenesis, metallurgical characterization and classification. *Mineralogical Magazine*, vol. 68. pp. 255–277.
- VAUGHN, J.C.D. 1982. Phase relations involving pyrrhotite below 350 degrees C. *Economic Geology*, vol. 77. pp. 1739–1754.
- VEARCOMBE, J., CHESHIRE, P., DE BEER, J., KILLICK, A., MALLINSON, W., McCOURT, S., and STETTLER, E. 1988. Structures related to the Antimony Line, Murchison schist belt, Kaapvaal Craton, South Africa. *Tectonophysics*, vol. 154. pp. 285–308.
- WARD, J. 1999. The metallogeny of the Barberton greenstone belt, South Africa and Swaziland. Council for Geoscience, Pretoria, South Africa.
- WELTE, D. 1969. Organic matter in sediments. *Organic Geochemistry*. Eglinton, G. and Murphy, M.T.J. (eds). Springer. pp. 262–264.
- ZHOU, J.Y. and CABRI, L.J. 2004. Gold process mineralogy: Objectives, techniques, and applications. *JOM*, vol. 56. pp. 49–52. ◆



# Automatic closed-loop scheduling in underground mining using discrete event simulation

by B. Skawina<sup>1</sup>, M. Astrand<sup>2,3</sup>, F. Sundqvist<sup>1,4</sup>, J. Greberg<sup>1</sup>, A. Salama<sup>5</sup>, and P. Ekbeck<sup>6</sup>

## Affiliation:

<sup>1</sup> Department of Civil, Environment and Natural Resources Engineering Division of Mining and Rock Engineering, Luleå University of Technology, Luleå, Sweden.

<sup>2</sup> Division of Decision and Control Systems, School of Electrical Engineering and Computer Science, KTH Royal Institute of Technology, Stockholm, Sweden.

<sup>3</sup> ABB Corporate Research Center, Västerås, Sweden.

<sup>4</sup> SimMine, Malå, Sweden.

<sup>5</sup> Department of Chemical and Mining, College of Engineering and Technology, The University of Dar es Salaam, Tanzania.

<sup>6</sup> ABB Industrial Automation, Process Industries, Umeå, Sweden.

## Correspondence to:

B. Skawina

## Email:

bart.skawina@ltu.se

## Dates:

Received: 20 Mar. 2020

Revised: 11 Sep. 2020

Accepted: 10 Mar. 2021

Published: June 2021

## How to cite:

Skawina, B., Astrand, M., Sundqvist, F., Greberg, J., Salama, A., and Ekbeck, P. 2021 Automatic closed-loop scheduling in underground mining using discrete event simulation.

Journal of the Southern African Institute of Mining and Metallurgy, vol. 121, no. 6, pp. 277–282.

## DOI ID:

<http://dx.doi.org/10.17159/2411-9717/679/2021>

## ORCID

B. Skawina  
<https://orcid.org/0000-0002-7334-4934>

M. Astrand  
<https://orcid.org/0000-0001-6778-51544>

J. Greberg  
<https://orcid.org/0000-0002-2306-9241>

## Synopsis

Today's mining operations require fast reporting and rapid rescheduling based on updated information. An automatic mine scheduling system could not only quickly reschedule but also propose alternative solutions. To avoid the financial and physical risks associated with testing such a system directly in operation, it could be first evaluated *via* discrete event simulation models. This would offer a safe environment to evaluate different operating rules and algorithms. In this study, this is achieved by integrating automatic scheduling software with a discrete event simulation model.

## Keywords

discrete event simulation; production planning; scheduling system; underground mining.

## Introduction

Traditionally, production planning in mining operations has been divided into four levels (Figure 1). In long-term planning, the focus is on formulating rough plans for mine production over a long period. These plans change over time to reflect the effects of a changing economy and market demand for minerals. Long-term plans can be used to establish financial forecasts relevant for the purchase of new equipment, changes in the workforce, and variations in operating costs (Hartmann and Mutmanský 2002). Long-term planning allows mine planners to first set mining targets and then test scenarios to find the best way to achieve the targets over multiple working periods. Medium-term and short-term plans contain a level of detail that reflects the immediate needs of the mine. These plans provide the information necessary for future production forecasts and predictions of market demands; they usually include daily production rates, material handling plans, equipment, and resource allocation. Production scheduling creates detailed schedules for a short period to ensure control of the ore grade, consistent daily operations (following a monthly plan), effective use of available resources, and maximum utilization of resources within the operating constraints (Hartmann and Mutmanský 2002).

Unexpected events can cause disturbances in operations, creating problems that a production planner must solve daily. In underground mining operations, manual rescheduling is time-consuming and production planners often find themselves in a situation where new or readjusted schedules are required in a very short time. It is also difficult to maintain a high quality of reporting and may even lead to a loss of important information.

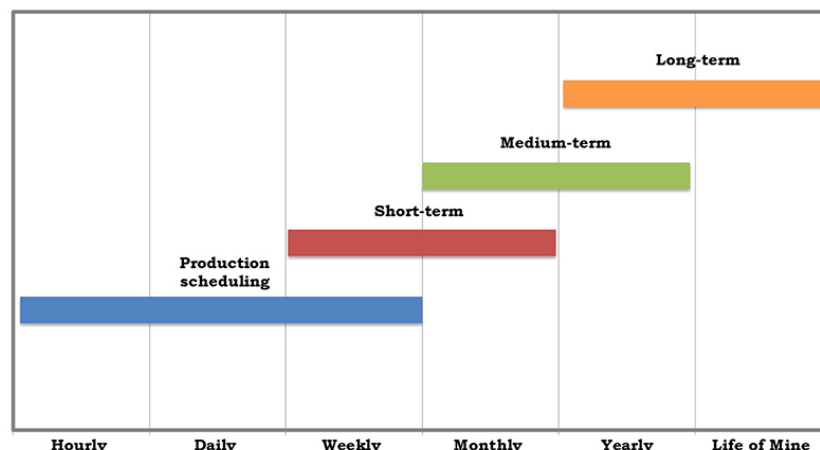


Figure 1—Time horizons for production plans in mining

## Automatic closed-loop scheduling in underground mining using discrete event simulation

An automated scheduling system, with real-time production feedback, could help planners initiate the necessary changes within a short time when unexpected events occur or when task execution can be improved. To avoid the financial and/or physical risks of testing the system in a real environment, automatic closed-loop scheduling can be connected to a simulation system. Tests in the real mine will still be required, but with simulation, many early issues may be resolved before changes are implemented in the mine operations. The challenge is threefold: to evaluate and accommodate complex and changing restrictions, to generate optimized production plans that meet production targets, and to promptly activate new production plans when unexpected errors occur. Introducing such an approach will help to optimize short-term production scheduling, reduce overall production costs and time, increase equipment efficiency, solve complex scheduling problems, and improve decision-making by increasing the efficiency and agility of planning tasks that are subject to change. This, in turn, will reduce operator stress, provide instant task progress reports, reduce the administrative workload, coordinate mine systems with fewer human errors, and unify scheduling.

This paper discusses the automatic scheduling tool and the commercial discrete-event simulator to create a possible digital twin that can be used to test various mine scenarios. This study was part of the Optimized Medium-Range Mine Scheduling (OMMS) project and was carried out by Luleå University of Technology (LTU), ABB, Boliden, and SimMine, coordinated by RockTech Centre, and funded by the partners and SIP STRIM. Further studies have been a part of the Sustainable Intelligent Mining Systems (SIMS) project and the H2020 EU Research and Innovation Programme.

### Scheduling and simulation

Scheduling is defined by Pinedo (2002), Brucker (2004), and Dugardin *et al.* (2007) as a process of allocating resources (people, equipment, or production lines) to tasks/jobs over time. The goal is to optimize (maximize or minimize) certain objectives, such as processing times or quantities, by making appropriate decisions (Dugardin *et al.* 2007; Fowler *et al.* 2006). When assigning the resources, decisions must be based on the production targets and other factors, such as priorities, sequencing, beginning and end of the job/task, but also including unexpected stops and rescheduling (Herrmann 2006). With the increasing complexity of systems and changing restrictions, scheduling should undergo a continuous cycle of improvement. However, the manual process of generating schedules consumes a lot of time, is prone to errors, and makes it difficult to incorporate real-time information. Thus, while production planners currently use their own experience and personal judgment (Song *et al.* 2015) in scheduling, they could be assisted by automated production scheduling systems.

Discrete event simulation (DES) is a widely used and suitable method for analysing dynamic systems in mining. In DES, variables change at discrete points when events occur (Banks 1998). An event can be an arrival or departure of a machine, for example. Simulation models are typically used for tactical and strategic decision support to solve problems that cannot be tackled by analytical techniques (Fowler and Rose 2004). They offer a solution to a problem in a controlled environment. One of the key advantages of simulation is that it does not disturb the existing system (Dugardin *et al.*, 2007).

There are various options for simulation and scheduling. The first option involves using the simulation as a base schedule for generating the initial schedules, improving the existing schedules, or optimizing the existing schedules from within the simulation (Fowler, Mönch, and Rose, 2006). This means the simulation model is a production control system used to derive production control instructions (Fowler, Mönch, and Rose, 2006). In an example given by Potradi, Maso, and Fowler (2002), a DES model was used to generate the schedule for machines and to plan the start of operations. A second option for simulation is to set parameters or test the instance generation required for scheduling. In this case, simulation is used to evaluate certain parameter setting strategies for a given production control scheme (Fowler, Mönch, and Rose, 2006). A third option is to use simulation to emulate and evaluate scheduling approaches. This allows the behaviour of a system to be evaluated. However, the simulation software has to have the functionality to model specific characteristics of the system (Mönch, Rose, and Sturm, 2003). Horiguchi *et al.* (2001) and Pritsker, O'Reilly, and Laval (1997) examined the performance of the algorithm by developing a simulation model in the AweSim DES language, while Mönch, Rose, and Sturm (2003) evaluated scheduling approaches in a simulation-based environment for manufacturing systems.

In this study, a connection between an automatic scheduler and a discrete event simulation (DES) tool is established to create a possible digital twin of the mine that could be used in the future to test various scenarios. This study considers the use of DES to emulate and evaluate the scheduler, with a focus on system interaction, scale of operation, and interaction between the underground mine model and the automatic production scheduling system. The simulator and scheduler thus jointly act as a test bed and decision support system. This enables the user to evaluate the automatic scheduling, current operating scheduling rules, and potential improvement strategies in close-to-real mine conditions without disturbing production.

### Integration of automatic scheduling system and DES model

The following section describes the integration of an automatic scheduling tool, the ABB Ability Operations Management System Execution Manager (OMS EM), and a DES tool, SimMine. The focus is on closing the loop in short-term mine scheduling by using simulation as a test bed and decision support system. OMS EM is a system for managing processes through detailed production schedules based on information collected from various sources. The system supports manual scheduling and intervention to enable such techniques as short interval control. An additional feature of OMS EM is the possibility to automatically create short-term schedules using algorithms. Scheduling is typically considered a manufacturing execution system, the intermediate layer between enterprise resource planning and production control. This means any industrial application of a manufacturing execution system must be tightly integrated with the (possibly complex) IT system on site. With this in mind, OMS EM was developed to support processes that can be modelled using the ISA-95 standard (ANSI/ISA-95.00.03 2005). The adherence to ISA-95 makes the integration with various information sources easier, as a common data model is used. Furthermore, in the mining industry, the standard is recognized by many companies as an enabler for future operation optimization (Roberts, 2016). Lastly, the automatic

# Automatic closed-loop scheduling in underground mining using discrete event simulation

scheduling feature in OMS EM enables closed-loop scheduling by incorporating real-time task progress from telemetry or mobile clients used by the production. Automatic scheduling is thus used to continuously reschedule based on the latest information available. Information is presented in the form of Gantt charts in which information is continuously updated (see Figure 2). In this study, machine location, machine activity, machine alarms, and delays are shown. Users can interact (in the Gantt chart) with the current automatically created schedule by reassigning orders to different equipment or editing the properties of the resources.

SimMine is a mining-oriented DES tool built on a full graphical interface. Since SimMine was developed specifically to simulate mining operations, it is made of interfaces where the user can set and specify underground mine-related parameters, such as fleet type and properties, rock properties, location sequences, shifts, and processing times. SimMine software accommodates various mine layouts and produces comprehensive output statistics. In this work, we develop a number of new modules to represent the surrounding information system, including extraction plans and maintenance systems. Based on the information obtained from the studied mine, SimMine can not only simulate the process, but also act as the mine operation centre (MOC) to coordinate activities.

The SimMine model of the simulated mine is shown in Figure 3. The figure includes the main interface and the graphical user interface (GUI). The main interface is split into main menu toolbars and tabs. Each tab consists of different input/output data for the current simulation. Input data includes fleet data (shift properties, activity cycles, fleet properties, operator costs, and materials), and layout data (face profiles, location type, dependencies, priorities, rock properties, and capacities). Output

data includes the statistics related to sequence, development, production, location, fleet performance measures, activity and loading, and transport. The GUI represents the layout of the 3D modelled scenario; it includes the tools and objects used for selecting, creating, or modifying the layout and views two perspectives: machine-centric and location-centric.

## Platform integration

The OMS EM scheduling system is responsible for generating schedules and assigning resources (or equipment) to tasks. The SimMine DES simulation is responsible for simulating the real mining system and reporting events to the scheduler (Figure 4). The layout of SimMine and OMS EM integration includes information related to the production/development plan, maintenance plan, system settings, localization, and additional mine services that can affect the scheduling in the mine.

At the start of the simulation, the simulator sends the location dependencies (available faces), order list (blast orders), and tasks (full set of drill and blast activities that should be performed in a particular set-up) to the scheduler (Figure 5).

During the simulation, vacant vehicles request work from the scheduler. Work comes in the form of work orders. When machines perform work, their work status is transferred to the scheduler (start/stop of activities and expected end time). To communicate and exchange information, OMS EM and SimMine use web services. The information is presented to users in the form of a Gantt chart (Figure 2). In the chart, activities such as the current status of work, finished or future mining activities are grouped depending on the orders, type of equipment, type of material, and location. This improves the decision-making for the automatic scheduling of the production cycle by sending

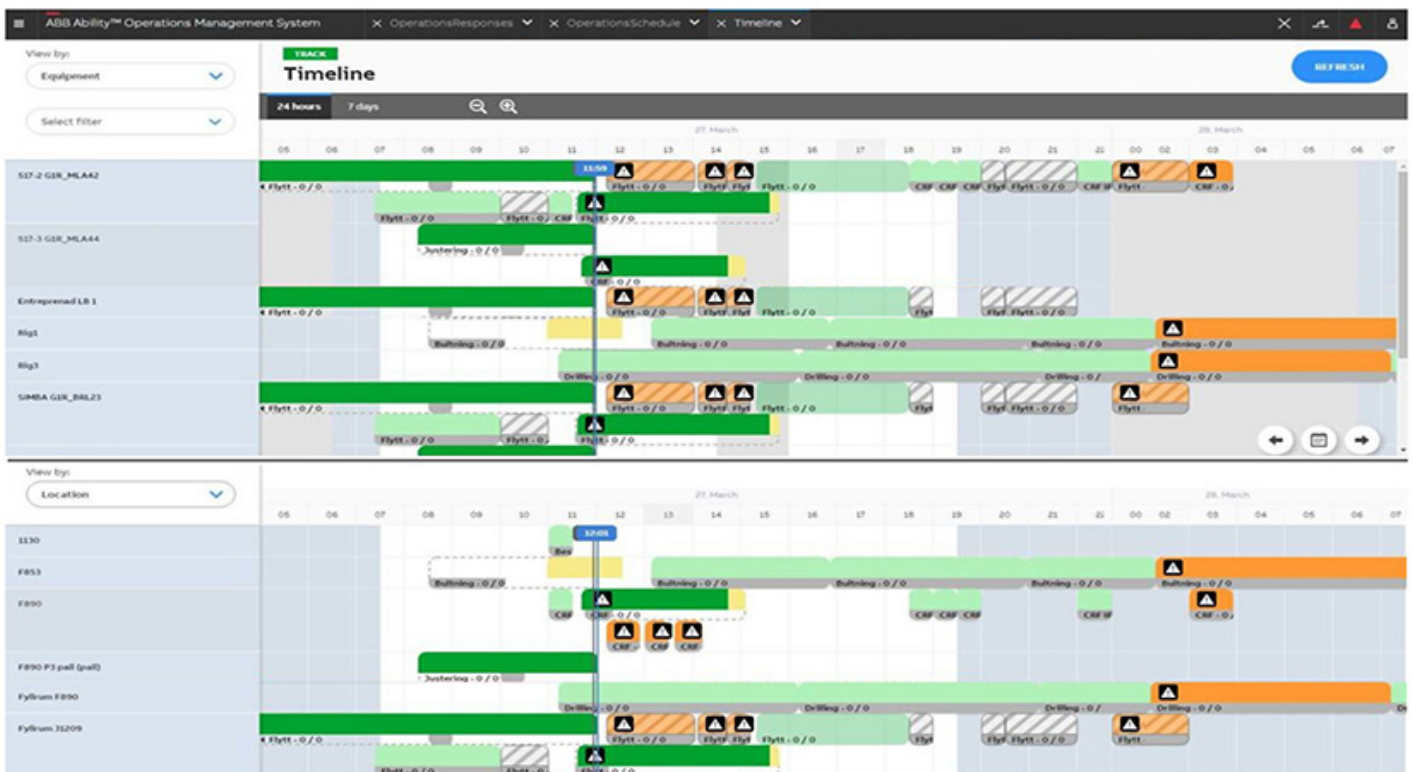


Figure 2—Views of the scheduling system. The top diagram presents a machine-centric Gantt chart; the bottom diagram presents the same information from a location-centric view

# Automatic closed-loop scheduling in underground mining using discrete event simulation

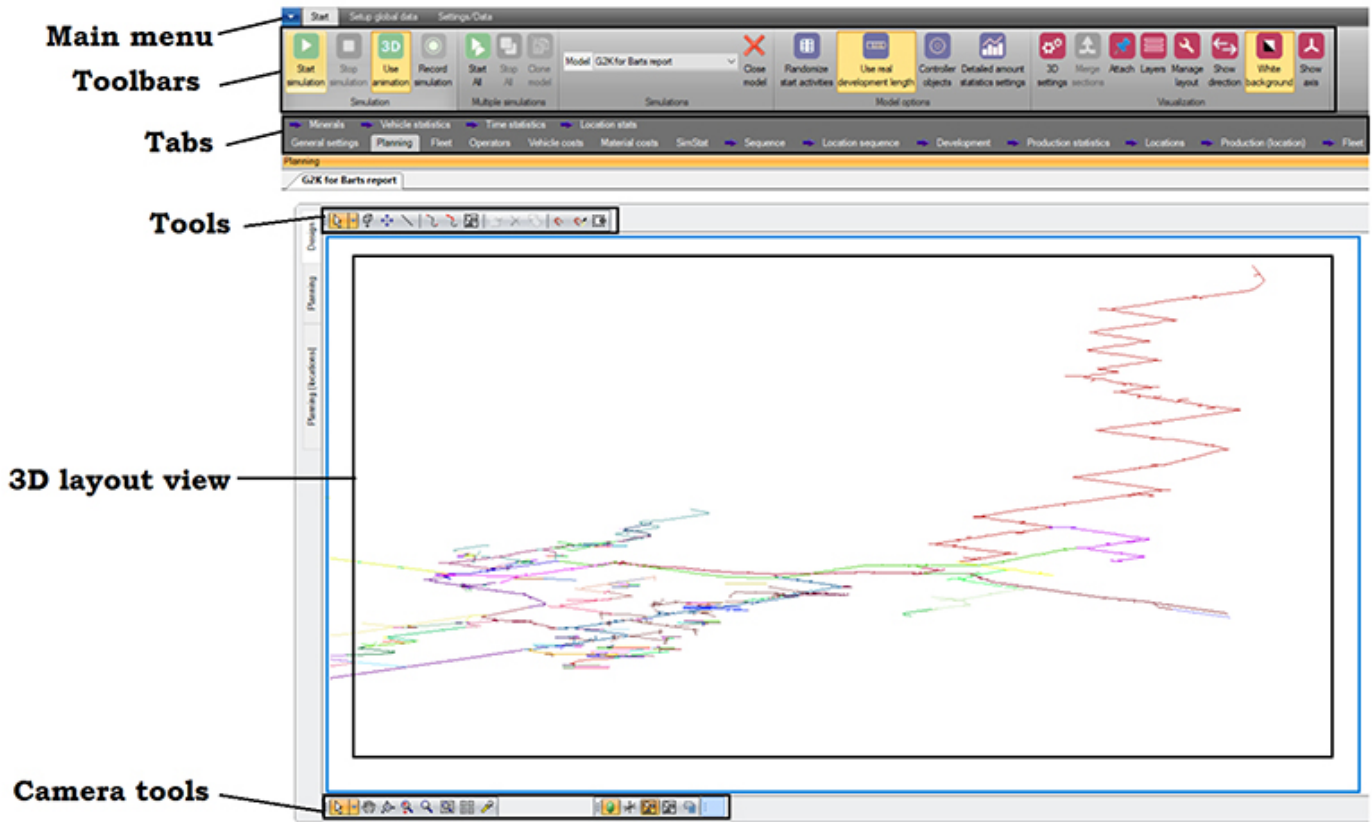


Figure 3—Simulation model

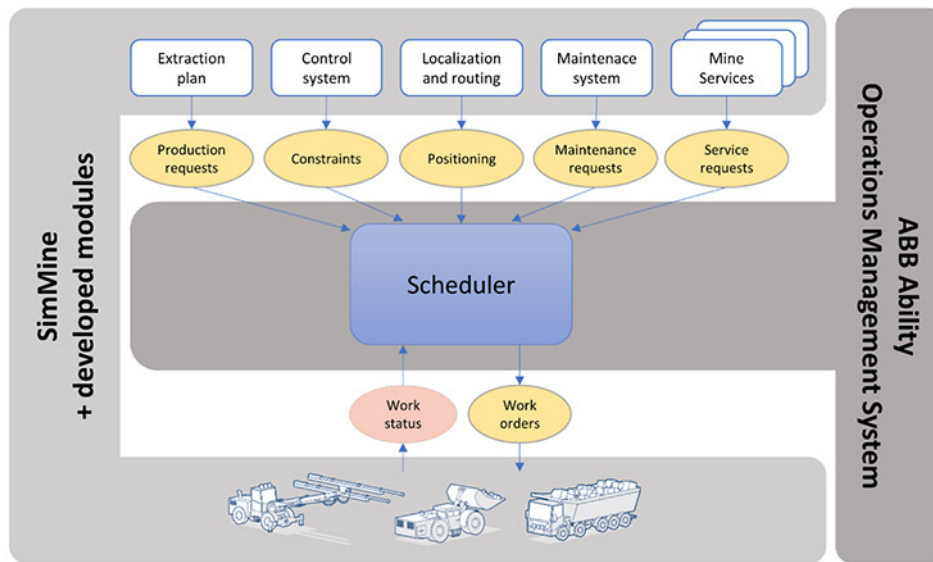


Figure 4—Layout of the integration of the scheduler and the simulator

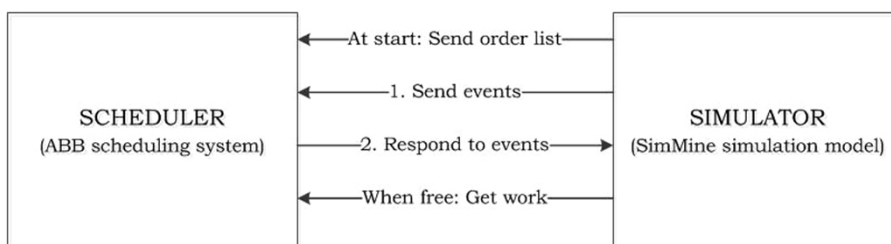


Figure 5—Platform interaction

# Automatic closed-loop scheduling in underground mining using discrete event simulation

feedback on work progress, together with reasons for machine interruptions, from each operation to the fleet management system.

## Simulation results

Multiple simulation runs are performed to check the functionality and quality of both the simulator and the scheduler. The main objective in this example is to demonstrate the joint system, and evaluate whether the automatic scheduler can achieve the same production results as schedules based on operational data. The designed system was tested on a small-scale operation (limited set of faces). The results are an example of two 2-week simulations runs.

The results presented in Figure 6 show the cumulated developed distance for both the base case scenario, using operational data with added activity switch time and working rules, and the scenario when using automatic scheduling. The activity switch time is a time penalty of around 20 minutes after a vehicle has finished a task until it can continue with the next task. The activity switch time is simulated to represent the real-life scenario where the operator is waiting to receive the next work order from the mine control centre. The work rules are the rules which prohibit the vehicle to start work at a face if there is 15 minutes or less time until a break occurs (shift ends or meal break). The developed distances achieved for the base case and the scenario when using automatic scheduling were 210 m and 217 m, respectively. For these two weeks, the comparison shows that the scenario where automatic scheduling was used produced similar results.

The results presented in Figures 7 and 8 show the machine utilization for the base case scenario and the scenario using automatic scheduling. Machine utilization is the effect of performing the work, where the work itself, shows similar results between the cases. Based on the comparison of the results between Figure 7 and Figure 8, the difference in the work time is the highest for three machines: bolter 1 (10%), drill rig, 3 (18%), and loader (11%). The results also show that the difference in the idle time is the highest for loader (24%), LHD 1 (20%), scaler 1 (18%), drill rig 3 (18%), and bolter 1 (18%). A comparison of the utilization of the machines shows that in the case of the scheduler the utilization is slightly lower compared with the base case scenario. Since the production results are almost matching, the difference in machine utilization originates from different guiding operating rules in the scheduling process.

## Concluding remarks

This study integrates an automatic scheduling system with a DES model. The joint system can achieve the same production results as schedules based on operational data. The simulator supports most of the functionality required to carry out a performance assessment, with all the required details. The proposed system can act as a test bed and a decision support system for functionality checks and quality controls. This enables the user to evaluate the schedules produced by the scheduling platform without interacting with existing systems or processes. When the scheduler is connected to the simulator, the mine operation centre can continue to update and use the simulator to test different algorithms and procedures/rules applied to the schedule or to

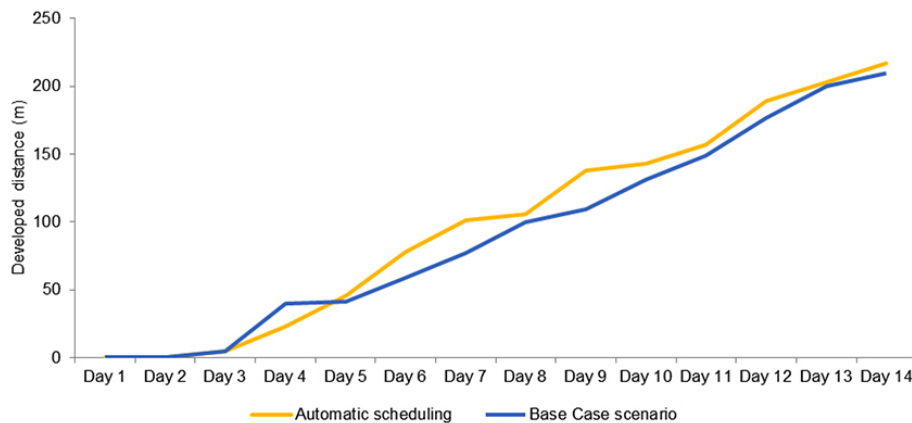


Figure 6—Cumulated developed distance

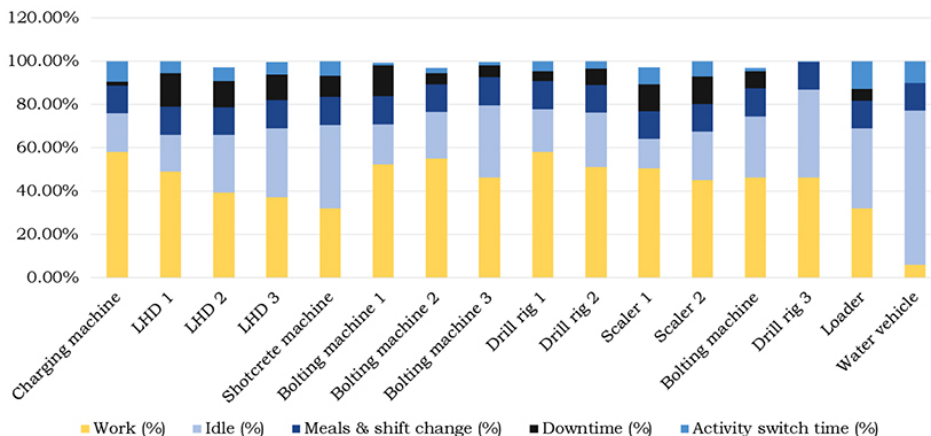


Figure 7—Base case scenario

## Automatic closed-loop scheduling in underground mining using discrete event simulation

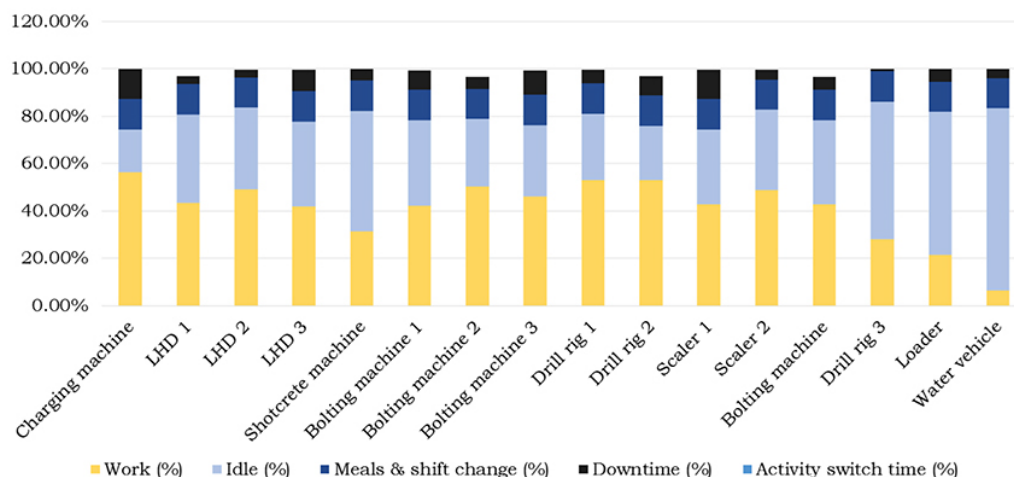


Figure 8—Scenario when using automatic scheduling

see the results of applying a specified production schedule in the simulator beforehand. In this way, the scheduling process can be tested in situations that could occur in a real environment, rather than in simple predefined scenarios. This opens the possibility to examine the impact of automatic scheduling compared to the current situations in mines, where production scheduling is highly manual.

### Future development

Formulating mathematical models to represent machine environments is very complex and subject to complex policies and rules related to sequence-dependent set-ups (Sivakumar 2001). The level of detail is an important part of the design, as it may increase the credibility of the model but also increase the complexity and execution time (Fowler and Rose 2004). The scheduler's primary function should be to reduce the time and effort necessary to produce feasible production schedules and to guide production management in the decision-making process. Therefore, future factors to consider when increasing the level of detail are rock mechanics, geological mapping, media, preventive maintenance, and material buffer capacity in different locations. An ongoing challenge in this project is to create the synchronized model representations in both the scheduler and the simulator. A future consideration is to leverage a standardization protocol for the automatic synchronization of these models.

### References

- ALBRECHT, M.C. 2010. Introduction to DES. <http://www.albrechts.com/mike/DES/Introduction%20to%20DES.pdf> [accessed 20 May 2017].
- ANSI/ISA-95.00.03-2005. Enterprise-control system integration. Part 3: Activity models of manufacturing operations management. [http://www.mecatronics.eesc.usp.br/wiki/upload/8/83/ISA-95.00.03-2000\\_Draft.pdf](http://www.mecatronics.eesc.usp.br/wiki/upload/8/83/ISA-95.00.03-2000_Draft.pdf) [accessed 13 March 2018].
- BANKS, J., CARSON, J.S., NELSON, B.L., and NICOL, D.M. 2010. Discrete Event System Simulation. Pearson Education, Hoboken, NJ.
- BANKS, J. 1998. Handbook of Simulation: Principles, Methodology, Advances, Applications, and Practice. Wiley, New York.
- BISKUP, D. and FELDMANN, M. 2001. Benchmarks for scheduling on a single machine against restrictive and unrestricted common due dates. *Computers & Operations Research*, vol. 28. pp. 781–801.
- BRUCKER, P. 2004. Scheduling Algorithms. 4th edn. Springer, Berlin.
- CUDDIHY, C. 2017. GMSG: Open mining format to improve 3D interoperability. *Global Mining Review*. <https://www.globalminingreview.com/special-reports/17112017/gmsg-open-mining-format-to-improve-3d-interoperability/> [accessed 6 March 2018].
- DUGARDIN, F., CHEHADE, H., AMODEO, L., YALAOUI, F., and PRINS, CH. 2007. Hybrid job shop and parallel machine scheduling problems: Minimization of total tardiness

criterion. *Multiprocessor Scheduling: Theory and Applications*. Levner, E. (ed.). Intech, Vienna. pp. 273–292.

- FOWLER, J.W., MÖNCH, L., and ROSE, O. 2006. Scheduling and simulation. *Handbook of Production Scheduling*. Springer. Chapter 5, pp. 109–133.
- FOWLER, J.W. and ROSE, O. 2004. Grand challenges in modeling and simulation of complex manufacturing systems. *Simulations*, vol. 80, no. 9. pp. 469–476.
- GONZALES, F.G. and DAVIS, W.J. 1998. Initializing online simulations from the state of a distributed system. *Proceedings of the 1998 Winter Simulation Conference*. Medeiros, E.F., Watson, E.F., Carson, J.S., and Manivannan, M.S., (eds). IEEE, Piscataway, NJ. pp. 507–513.
- HALL, N.G. and POSNER, M.E. 2001. Generating experimental data for computational testing with machine scheduling applications. *Operations Research*. vol. 49. pp. 854–865.
- HARTMANN, H.L. and MUTMANSKY, J.M. 2002. Introductory Mining Engineering. 2nd edn. Wiley.
- HERRMANN, J.W. 2006. Decision-making systems in production scheduling. *Handbook of Production Scheduling*. Springer. Chapter 4, pp. 91–108.
- HORIGUCHI, K., RAGHAVAN, N., UZSOY, R., and VENKATESWARAN, S. 2001. Finite-capacity production planning algorithms for a semiconductor wafer fabrication facility. *International Journal of Production Research*, vol. 39, no. 5. pp. 825–842.
- HORN, R.L. 1971. Validation of simulation results. *Management Science*. vol. 17, no. 5. pp. 247–258.
- MÖNCH, L., ROSE, O., and STURM, R. 2003. A simulation framework for the performance assessment of shop-floor control systems. *Simulations*. vol. 79, no. 3. <https://doi.org/10.1177/0037549703256039>
- PINEDO, M.L. 2002. Scheduling: Theory, Algorithms, and Systems. 2nd edn. Prentice-Hall, Englewood Cliffs, NJ.
- POTRADI, J., MASO, S., and FOWLER, J.W. 2002. Using simulation-based scheduling to maximize demand fulfilment in a semiconductor assembly facility. *Proceedings of the Winter Simulation Conference*. IEEE, Piscataway, NJ. pp. 1857–1861.
- PRITSKER, A.A.B., O'REILLY, J.J., and LAVAL, D.K. 1997. Simulation with Visual SLAM and AweSim. Wiley, New York.
- RIPPENHAGEN, C. and KRISHNASWAMY, S. 1998. Implementing the theory of constraints philosophy in highly reentrant systems. *Proceedings of the 1998 Winter Simulation Conference*. Medeiros, E.F., Watson, E.F., Carson, J.S., and Manivannan, M.S. (eds). IEEE, Piscataway, NJ. pp. 993–996.
- ROBERTS, R. 2016. BHPB: Why ISA-95 is a game changer. *Mining Magazine*. <https://www.miningmagazine.com/innovation/news/1263186/isa-bhpbps-vision> [accessed 1 February 2018].
- SCHLESINGER, P. 1974. Developing standard procedures for simulation validation and verification. *Proceedings of the Summer Computing Simulation Conference*, vol. 1. Society for Computer Simulation, San Diego, CA. p. 927.
- SIVAKUMAR, A.I. 2001. Multiobjective dynamic scheduling using discrete event simulation. *International Journal of Computer Integrated Manufacturing*, vol. 14, no. 2. pp. 154–167.
- SONG, Z., SCHUNNESSON, H., RINNE, M., and STURGUL, J. 2015. Intelligent scheduling for underground mobile mining equipment. *PLOS One*. <https://journals.plos.org/plosone/article?id=10.1371/journal.pone.0131003> [accessed 3 January 2018].
- YUCESAN, E. and FOWLER, J. 2000. Simulation analysis of manufacturing and logistics systems. *Encyclopedia of Production and Manufacturing Management*, Kluwer Academic, Boston, MA. pp. 687–697. ◆



# Synthesis of Pt-based alloy nanostructures

G.M. Leteba<sup>1</sup> and E. van Steen<sup>1</sup>

## Affiliation:

<sup>1</sup> Catalysis Institute, Department of Chemical Engineering, University of Cape Town, South Africa.

## Correspondence to:

E. van Steen

## Email:

eric.vansteen@uct.ac.za

## Dates:

Received: 30 Aug. 2020  
Revised: 24 Mar. 2021  
Accepted: 24 Mar. 2021  
Published: June 2021

## How to cite:

Leteba, G.M. and van Steen, E. 2021  
Synthesis of Pt-based alloy nanostructures.  
Journal of the Southern African Institute of Mining and Metallurgy, vol. 121, no. 6, pp. 283–286.

## DOI ID:

<http://dx.doi.org/10.17159/2411-9717/1345/2021>

## ORCID

G.M. Leteba  
<http://orcid.org/0000-0001-7982-5037>

## E. van Steen

<http://orcid.org/0000-0003-4659-8522>

## Synopsis

Optimizing the catalytic performance of multimetallic nanoparticle (NP) catalysts demands a concrete understanding of their design, while preferentially deploying wet chemical synthesis procedures to precisely control surface structural properties. Here we report the influence of reductants such as hydrogen-rich tetrabutylammonium borohydride (TBAB) and carbon monoxide-rich molybdenum carbonyl ( $\text{Mo}(\text{CO})_6$ ) on the shape and morphological evolution of Pt-based binary (PtNi and PtCo) and ternary (PtNiAu and PtCoAu) nanostructures derived from a homogeneous solution of amine-based surface active agents (surfactants) in a high boiling point solvent. We successfully synthesized nanostructures exhibiting well-defined and composition-controlled surfaces deploying a one-pot synthetic approach. The development of the surface properties was, however, observed to be alloy-specific. The resultant highly monodisperse alloy NP with narrow size distributions and facet-oriented surfaces are expected to display enhanced functionality as catalysts for utilization in specific chemical reactions.

## Keywords

catalyst. platinum alloy, nanoparticles, synthesis, mixed-metal nanostructure.

## Introduction

Alloy nanoparticles (NPs), with core-shell or alloyed structures, are emerging as better catalyst candidates than monometallic NPs (Wang *et al.*, 2019; Leteba *et al.*, 2018). Bimetallic nanocatalysts are anticipated to exhibit unique properties as a result of their solid solution state (Wang *et al.*, 2019), and also to have unusual surface structures due to synergistic effects (Wang *et al.*, 2019; Adams *et al.*, 2009). A fundamental understanding of the structure-composition-activity relationships, *i.e.* how atomic arrangement influences performance, is a key to rational catalyst design for a particular reaction process at the nanoscale (Meunier, 2008). Detailed structural characterization of mixed-metal nanostructures for the investigation of the basic structural properties comprising size, shape, dispersion, purity, composition, and structure, is thus indispensable for their utilization in many industrial processes. The reliable synthesis of Pt-based nanostructures for high-performance applications is in great demand, but is more difficult to achieve than the synthesis of monometallic NPs (Wang and Li, 2011).

When two or more metal precursors are reduced simultaneously in a wet chemical synthetic route, they can thermodynamically nucleate and grow individually. This may result in the formation of either separate NPs, or hetero-structured or core-shell structures because of the differences in the standard reduction potentials. However, alloy NPs are formed in most cases (Shan *et al.*, 2014). Simultaneous reduction of two or more metal precursor salts at nearly similar rates is achievable by using reductants at high temperatures in the presence of appropriate surface-active agents (surfactants) and solvents (Dumestre, 2004; Huang *et al.*, 2009). Although the prime objective of introducing the surfactants into the synthetic system prior to the co-reduction of different metal precursors is to control growth of the particles, prohibit the formation of NP agglomerates, and limit the degree of NP oxidation, a homogeneous mixture of two or more surfactants can be also be used to promote anisotropic growth; hence the evolution of crystallographic-facet-directed solid solutions (Leteba *et al.*, 2018, 2020). The evolution of high-index surfaces of these nanostructures can, however, be specific for a particular alloy system. Shape- and size-controlled growth of Pt-based alloy NPs can also be influenced by varying the reductants while keeping the other reaction conditions constant, but these reductants can influence the

## Synthesis of Pt-based alloy nanostructures

evolution of different morphologies, sizes, and compositions, depending on their chemical nature and strength on inducing the reduction of metal precursors (Yin and Alivisatos, 2005; Chen *et al.*, 2018; Dahl, Maddux, and Hutchison, 2007; Wang *et al.*, 2007).

Here, we show that crystallographic-facet-directed alloy nanostructures can be formed via optimal solution-based synthetic methods by varying two distinct reductants in the presence of a homogeneous mixture of ternary surfactants – oleylamine (OAm), octadecylamine (ODA), and trioctylamine (TOA) – in a high boiling point solvent, benzyl ether (BE). These Pt-based binary nanoalloys were successfully synthesized by the simultaneous reduction of Pt and *M* (*M* = Ni and Co) precursor salts using carbon monoxide (CO)-rich molybdenum carbonyl ( $\text{Mo}(\text{CO})_6$ ) and hydrogen-rich tetrabutylammonium borohydride (TBAB) as the reductants. Good manipulation over sizes, morphologies, compositions, dispersity, and surface structures of these alloy NPs was obtained through rigorous control of the synthesis parameters such as the reduction temperature, concentration and type of the surfactants, distinct metal precursors, reaction time, and (most importantly) the reductants. It should be noted that a kinetic and/or mechanistic analysis of the particle growth was beyond the scope of this study.

### Experimental

#### Synthesis of binary alloy NPs

In a typical synthesis, precursor salts  $\text{Pt}(\text{acac})_2$  (40 mg) and  $\text{Ni}(\text{Ac})_2 \cdot 4\text{H}_2\text{O}$  or  $\text{Co}(\text{Ac})_2 \cdot 4\text{H}_2\text{O}$  (24 mg) were dissolved in oleyl amine (OAm, 15 ml), trioctylamine (TOA, 10 ml), and octadecyl amine (ODA, 4.4 g) (surfactants) using benzyl ether (BE, 20 ml) as a high boiling-point solvent. The resulting metal salt-surfactant-solvent reaction mixture was heated at 150°C for 5–10 minutes under vigorous magnetic stirring in a round-bottom flask. Upon addition of  $\text{Mo}(\text{CO})_6$  (60 mg), the resultant pale-yellow homogeneous solution turned dark purple with evolving cloudy smoke, suggesting the evolution of gaseous CO. The bulk organic synthesis mixture then turned dark brown during the heat-up process to 240°C, with a heating rate of 10°C/min. Alternatively, the introduction of TBAB (60 mg) resulted in the rapid formation of the dark brown colloidal solution. In both cases, the resultant colloidal mixtures were held at 240°C for 60 minutes. Thereafter, the colloidal medium was removed from the heat source and quenched using cold water to ensure minimal structural transformations during the cooling process. Subsequently, the as-synthesized NPs were extracted from the synthesis media through flocculation by adding excess absolute ethanol. After settling (typically 2–3 days), the excess organic solvents were decanted and the particles were further cleaned by re-suspending in absolute ethanol. This colloidal precipitation-purification process was performed 3–4 times. The black product was finally re-suspended in chloroform, yielding a dark brown colloidal suspension for all alloy NPs.

#### Synthesis of ternary alloy NPs

Precursor salts  $\text{Pt}(\text{acac})_2$  (40 mg) or  $\text{H}_2\text{PtCl}_6 \cdot x\text{H}_2\text{O}$  (52 mg),  $\text{Ni}(\text{Ac})_2 \cdot 4\text{H}_2\text{O}$  or  $\text{Co}(\text{Ac})_2 \cdot 4\text{H}_2\text{O}$  (24 mg) and  $\text{HAuCl}_4$  (12 mg) were dissolved in a mixture of OAm (15 ml), TOA (10 ml), and ODA (4.4 g) (surfactants) using BE (20 ml). The synthesis conditions and precipitation-purification processes were the same as those described in the previous section.

### Results and discussion

The nature of the precursor salts, reduction temperature, reducing agents, and surfactants can dictate the nucleation and growth kinetics of metal NPs, hence influencing the final surface structural properties (size and shape). Depending on the nature of individual surfactant's functional group, the degree of adsorption of two or more surfactants on growing crystal surfaces within the organic synthetic system can differ (Yin and Alivisatos, 2005; Chen *et al.*, 2018; Dahl, Maddux, and Hutchison, 2007; Wang *et al.*, 2007). Furthermore, good manipulation of the nucleation and subsequent growth of solution-grown NPs often demands the use of some specific reducing agents or metal precursors (Dumestre, 2004; Huang *et al.*, 2009). In order to circumvent the formation of spontaneous separate or heterostructured NPs and to obtain homogeneous nucleation and subsequent crystal growth of two or more dissimilar metal atoms, the reaction kinetics must be accurately regulated to obtain well-defined and mixed solid solution NPs, which may be either ordered or disordered. Figure 1 displays the possible structures that can be obtained by the synthesis of binary and ternary nanostructures under precisely tuned synthesis parameters.

Here, we explore the influence of systematically varying the Pt precursor and reducing agent (reductant) components, on the preparation of the solid solution NPs. The reduction kinetics of Pt and *M* (Ni and Co) precursor salts were systematically influenced by introducing the reductants such as  $\text{Mo}(\text{CO})_6$  or TBAB into the bulk organic synthesis mixture. We used amine-containing surfactant mixtures (OAm, TOA, and ODA), which contain similar functional groups, for fine-tuning of composition, size distribution, monodispersity, and crystal faceting of the solid solution NPs. A high boiling-point solvent, benzyl ether (BE, boiling point: 298°C), served as a liquid phase for nucleation, growth, and controlled mixing of distinct metal atoms; hence providing an avenue for uniform crystal growth. Nanostructures prepared using  $\text{Mo}(\text{CO})_6$  are displayed in Figures 2a and b whereas those synthesized using TBAB are shown in Figures 2c and 2d.

Our synthesis strategies produced binary NPs exhibiting good monodispersity, distinct morphologies, and narrow size distribution, as revealed by the bright-field transmission electron microscopy (BR-TEM) images shown in Figure 2. Even though these binary alloys were synthesised under the same reaction parameters but only varying the reductants, the sizes and morphologies are different in all cases. This suggests that the formation of these nanoalloy particles can be dictated by the reaction parameters (such as temperature, concentration

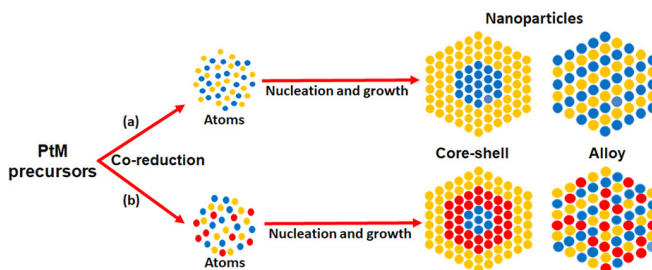


Figure 1—Illustration of possible nanostructures that can form during synthesis of (a) binary alloy nanostructures from two metal precursor salts and (b) ternary nanostructures from three metal precursor salts, under well-controlled reaction conditions

## Synthesis of Pt-based alloy nanostructures

of both hydrophilic and hydrophobic surfactants, solvents, and metal precursors) and the nature of the reductants used during synthesis. The inserts in the figures are high-resolution-TEM (HR-TEM) images showing highly crystalline alloy nanostructures, and the same orientation of lattice fringes suggests that the individual particles are single crystals.

Figures 2a and 2b are BR-TEM- images of alloy nanostructures solution-grown by co-reduction of  $\text{Ni}(\text{Ac})_2 \cdot 4\text{H}_2\text{O}$  (or  $\text{Co}(\text{Ac})_2 \cdot 4\text{H}_2\text{O}$ ) and  $\text{Pt}(\text{acac})_2$  precursors using CO-rich  $\text{Mo}(\text{CO})_6$ , which is the main source of CO gas. The resultant alloy particles display mostly cuboidal morphologies encased by {200} crystal facets. This is expected since previous studies have shown that the decomposition of  $\text{W}(\text{CO})_6$  results in the formation of  $\text{W}^0$  while at the same time liberating gaseous CO.  $\text{W}^0$  can then be used as a reductant, rapidly reducing  $\text{Pt}^{2+}$  to  $\text{Pt}^0$  (atoms/seeds). This leads to fast Pt nucleation (Zhang and Fang, 2009; LaGrow *et al.*, 2015). However,  $\text{W}^0$  does not alloy with  $\text{Pt}^0$  under the reaction conditions and thus remains as an ionic species ( $\text{W}^{n+}$  or  $\text{W}^{6+}$ ) in the organic synthesis mixture (Zhang and Fang, 2009), but facilitates growth of the nanoparticles (Zhang *et al.*, 2010). CO is known to adsorb selectively onto Pt, with stronger preferential binding on {100} facets and weaker adsorption on {111} facets (Wu, Zheng, and Fu, 2011; Chen *et al.*, 2012). Such preferential adsorption on Pt{100} crystal facets encourages the formation of cubic Pt and Pt alloy nanostructures (Wu, Zheng, and Fu, 2011; Chen *et al.*, 2012). Our studies indicate that  $\text{Mo}(\text{CO})_6$ -assisted reduction of metal precursors is an applicable synthetic technique for the production of not only monodisperse NPs with a narrow size distribution, but also well-defined and facet-directed NP morphologies. It is therefore reasonable to conclude that  $\text{Mo}(\text{CO})_6$ , similar to  $\text{W}(\text{CO})_6$ , plays an essential role

in the production of high-quality cuboidal alloy nanostructures. The NP uniformity obtained from the different metal salts to zero-valent metal states ( $\text{Pt}^0/\text{M}^0$ ) is expected to originate from the contribution of both CO gas and MoO species generated from the thermolytic decomposition of  $\text{Mo}(\text{CO})_6$ , with Mo species serving as the sacrificial reductant in the nucleation stages of alloy NPs. The measured mean particle sizes from TEM images of randomly chosen 300 NP populations were  $7.1 \pm 0.5$  nm (PtNi) and  $12.5 \pm 0.7$  nm (PtCo), exhibiting narrow particle size distributions.

Simultaneous reduction of  $\text{Ni}(\text{Ac})_2 \cdot 4\text{H}_2\text{O}$  (or  $\text{Co}(\text{Ac})_2 \cdot 4\text{H}_2\text{O}$ ) and  $\text{Pt}(\text{acac})_2$  precursors using the  $\text{H}_2$ -rich reducing agent TBAB ( $\text{C}_{16}\text{H}_{36}\text{N}(\text{BH}_4)$ ) resulted in the production of predominantly spherical particles (Figures 2c and 2d). The measured average sizes of these binary NPs were  $3.6 \pm 0.9$  nm (PtNi) and  $4.5 \pm 0.4$  nm (PtCo), with narrow size distributions. Our studies indicate that TBAB-assisted reduction of metal precursors is a fast and facile synthetic approach for the formation of monodisperse small-sized NPs with a narrow size distribution. Based on these experiments, it is therefore reasonable to deduce that the co-reduction of metal precursors proceeds at a faster rate in the presence of reductant TBAB and nucleation of NPs thus occurs faster, followed by slow crystal growth. The significant influence of TBAB, resulting in synthesis of uniform small-sized NPs, could be associated with  $\text{H}_2$  gas, which is released during the decomposition of TBAB and serves as a powerful reductant.

We also investigated the effect of the addition of a third metal component on size evolution and morphological selectivity of the alloy NPs. The simultaneous reduction of  $\text{Pt}(\text{acac})_2$  and  $\text{HAuCl}_4$  in the presence of  $\text{Ni}(\text{Ac})_2 \cdot 4\text{H}_2\text{O}$  and  $\text{Co}(\text{Ac})_2 \cdot 4\text{H}_2\text{O}$ , using  $\text{Mo}(\text{CO})_6$ , produced ternary PtNiAu and PtCoAu alloy NPs displaying well-defined and uniform, near spherical morphologies, as shown in

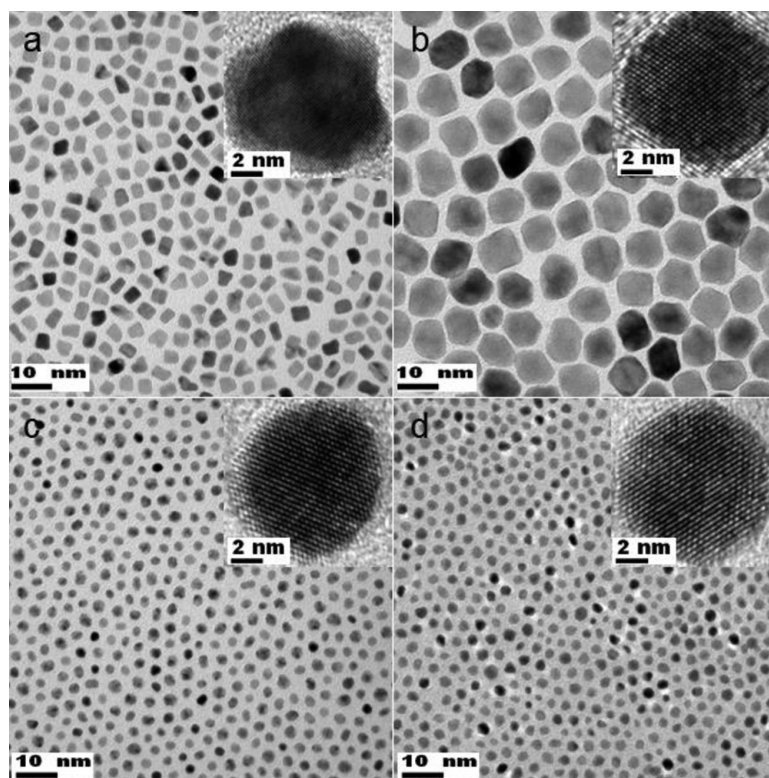
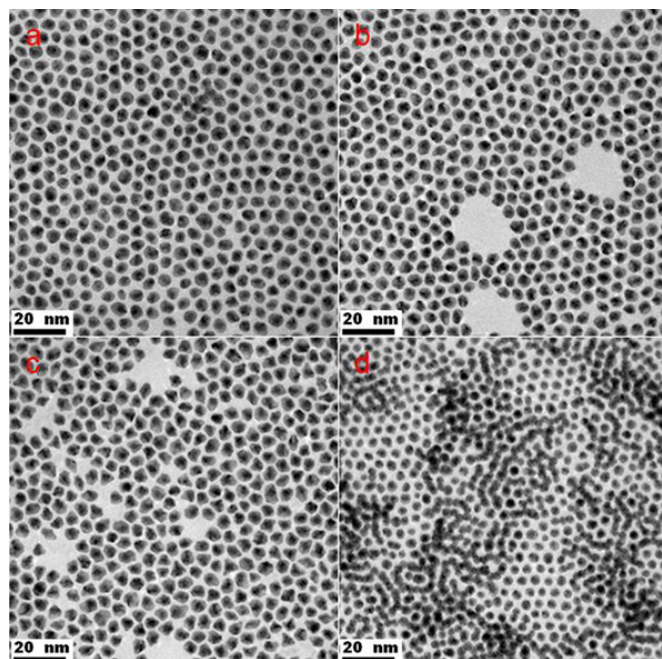


Figure 2—Bright-field TEM images of as-synthesised binary (a) PtNi and (b) PtCo bimetallic NPs using  $\text{Mo}(\text{CO})_6$  as a reducing agent. PtNi (c) and PtCo (d) were prepared using TBAB. The inserts show the HR-TEM images of these alloy NPs, displaying a high degree of crystallinity, and the same orientation of lattice fringes suggests that these particles are single crystals



**Figure 3**—BF-TEM images of ternary (a) PtNiAu and (b) PtCoAu NPs obtained from the co-reduction of Pt(acac)<sub>2</sub> and HAuCl<sub>4</sub> in the presence of Ni(Ac)<sub>2</sub>·4H<sub>2</sub>O and Co(Ac)<sub>2</sub>·4H<sub>2</sub>O respectively, using Mo(CO)<sub>6</sub> as the reductant. (c) and (d) are TEM-BF images of PtNiAu and PtCoAu ternary NPs respectively, formed by substituting Pt(acac)<sub>2</sub> with H<sub>2</sub>PtCl<sub>6</sub>·xH<sub>2</sub>O under fixed experimental conditions and using Mo(CO)<sub>6</sub> reductant

Figures 3a and 3b, respectively. The measured mean edge lengths of these ternary NPs were PtNiAu 14.5 ± 0.9 nm and 14.7 ± 0.8 nm, displaying narrow size distributions. When Pt(acac)<sub>2</sub> was substituted with H<sub>2</sub>PtCl<sub>6</sub>·xH<sub>2</sub>O under fixed experimental conditions and using Mo(CO)<sub>6</sub> reductant, the PtNiAu system produced mostly irregular shapes, whereas the ternary PtCoAu system yielded spherical nanostructures as shown in Figures 3c and 3d, respectively. Thus, variation in Pt precursors did not result in any significant size and morphological differences between the ternary PtNiAu (average particle sizes 16.1 ± 1.2 nm) and PtCoAu (average particle sizes 10.7 ± 0.8 nm) systems. However, the cubic symmetry of binary alloy structures (Figures 3a and 3b) is broken, with the resultant ternary structures adopting spherical morphologies. This could be associated with the distinct chemical behaviour of Au, interfering with complete CO adsorption or contribution of Mo species on the nucleation stage of Pt.

### Conclusion

Our findings clearly demonstrate the preparation of alloy nanostructures with distinct surfaces is achievable via precisely-controlled synthetic approaches. Good control over size, morphology, composition, dispersity, and surface structure of these alloy NPs was achieved using a one-pot synthetic approach and manipulating the experimental parameters. Although varying the reductants such as Mo(CO)<sub>6</sub> and TBAB under fixed reduction conditions resulted in the evolution of well-defined morphologies of binary (PtNi and PtCo) and ternary (PtNiAu and PtCoAu) NPs, these morphologies were found to be alloy-specific. This synthetic strategy to produce high-quality alloys of binary and ternary structures offers great potential for the successful synthesis of

highly nanomaterials with controllable compositions to substitute pure Pt for use in current and future industrial applications.

### Acknowledgement

This project was funded through the SARChI chair in Reaction Engineering (NRF grant number 114606).

### Author contributions

Eric van Steen conceived the idea and supervised the project. Gerard Malefane Leteba synthesized nanoparticles. Gerard Malefane Leteba and Eric van Steen processed, interpreted TEM data and wrote the manuscript. All authors commented on the manuscript.

### References

- ADAMS, B.D., WU, G., NIGRO, S., and CHEN, A. 2009. Facile synthesis of Pd–Co nanostructures with high capacity for hydrogen storage. *Journal of the American Chemical Society*, vol. 131. pp. 6930–6931.
- CHEN, Y., FAN, Z., ZHANG, Z., NIU, W., LI, C., YANG, N., CHEN, B., and ZHANG, H. 2018. Two-dimensional metal nanomaterials: Synthesis, properties, and applications. *Chemical Reviews*, vol. 118. pp. 6409–6455.
- DAHL, J.A., MADDUX, B.L.S., and HUTCHISON, J.E. 2007. Toward greener nanosynthesis. *Chemical Reviews*, vol. 107. pp. 2228–2269.
- DUMESTRE, F. 2004. Superlattices of iron nanocubes synthesized from Fe[N(SiMe<sub>3</sub>)<sub>2</sub>]<sub>2</sub>. *Science*, vol. 303. pp. 821–823.
- HUANG, X., ZHANG, H., GUO, C., ZHOU, Z., and ZHENG, N. 2009. Simplifying the creation of hollow metallic nanostructures: One-pot synthesis of hollow palladium/platinum single-crystalline nanocubes. *Angewandte Chemie International Edition*, vol. 48. pp. 4808–4812.
- LAGROW, A.P., KNUDSEN, K.R., ALYAMI, N.M., ANJUM, D.H., and BAKR, O.M. 2015. Effect of precursor ligands and oxidation state in the synthesis of bimetallic nanoalloys. *Chemistry of Materials*, vol. 27. pp. 4134–4141.
- LETEBA, G.M., MITCHELL, D.R.G., LEVEQUE, P.B.J., and LANG, C.I. 2018. Solution-grown dendritic Pt-based ternary nanostructures for enhanced oxygen reduction reaction functionality. *Nanomaterials*, vol. 8. p. 462. <https://doi.org/10.3390/nano8070462>
- LETEBA, G.M., MITCHELL, D.R.G., LEVEQUE, P.B.J., MACHELI, L., VAN STEEN, E., and LANG, C.I. 2020. High-index core-shell Ni–Pt nanoparticles as oxygen reduction electrocatalysts. *ACS Applied Nano Materials*, vol. 3. pp. 5718–5731.
- MEUNIER, F.C. 2008. Bridging the gap between surface science and industrial catalysis. *ACS Nano*, vol. 2. pp. 2441–2444.
- SHAN, S., LUO, J., YANG, L., and ZHONG, C.J. 2014. Nanoalloy catalysts: Structural and catalytic properties. *Catalysis Science and Technology*, vol. 4. pp. 3570–3588.
- WANG, C., DAIMON, H., LEE, Y., KIM, J., and SUN, S. 2007. Synthesis of monodisperse Pt nanocubes and their enhanced catalysis for oxygen reduction. *Journal of the American Chemical Society*, vol. 129. pp. 6974–6975.
- WANG, D. and LI, Y. 2011. Effective octadecylamine system for nanocrystal synthesis. *Inorganic Chemistry*, vol. 50. pp. 5196–5202.
- WANG, Y.-C., SLATER, T.J.A., LETEBA, G.M., ROSEMAN, A.M., RACE, C.P., YOUNG, N.P., KIRKLAND, A.I., LANG, C.I., and HAIGH, S.J. 2019. Imaging three-dimensional elemental inhomogeneity in Pt–Ni nanoparticles using spectroscopic single particle reconstruction. *Nano Letters*, vol. 19. pp. 732–738.
- WU, B., ZHENG, N., and FU, G. 2011. Small molecules control the formation of Pt nanocrystals: A key role of carbon monoxide in the synthesis of Pt nanocubes. *Chemical Communications*, vol. 47. pp. 1039–1041.
- YIN, Y. and ALIVISATOS, A.P. 2005. Colloidal nanocrystal synthesis and the organic–inorganic interface. *Nature*, vol. 437. pp. 664–670.
- ZHANG, J. and FANG, J. 2009. A general strategy for preparation of Pt 3d-transition metal (Co, Fe, Ni) nanocubes. *Journal of the American Chemical Society*, vol. 131. pp. 18543–18547.
- ZHANG, J., YANG, H., FANG, J., and ZOU, S. 2010. Synthesis and oxygen reduction activity of shape-controlled Pt<sub>3</sub>Ni nanopolyhedra. *Nano Letters*, vol. 10. pp. 638–644. ◆



# A Bayesian network approach for geotechnical risk assessment in underground mines

R. Mishra<sup>1</sup>, L. Uotinen<sup>2</sup>, and M. Rinne<sup>2</sup>

## Affiliation:

<sup>1</sup> First Quantum Minerals Limited, Zambia.

<sup>2</sup> Aalto University, Department of Civil Engineering, Finland.

## Correspondence to:

R. Mishra

## Email:

riteshmining@gmail.com

## Dates:

Received: 14 Jan. 2019

Revised: 15 Apr. 2020

Accepted: 14 Mar. 2021

Published: June 2021

## How to cite:

Mishra, R., Uotinen, L., and Rinne, M. 2021

A Bayesian network approach for geotechnical risk assessment in underground mines.

Journal of the Southern African Institute of Mining and Metallurgy, vol. 121, no. 6, pp. 287–294.

## DOI ID:

<http://dx.doi.org/10.17159/2411-9717/581/2021>

## Synopsis

Underground mining gives rise to geotechnical hazards. A formal geotechnical risk assessment can help to forecast and mitigate these hazards. Frequentist probability methods can be used when the hazard does not have many variables and a lot of data is available. However, often there is not enough data for probability distributions, such as in the case of new projects. The risk assessment is often subjective and qualitative, based on expert judgement. The purpose of this research is to present the use of Bayesian networks (BNs) as an alternative to existing risk assessment methods in underground mines by combining expert knowledge with data as it becomes available. Roof fall frequency forecasting using parameter learning is demonstrated with 1141 sets of roof fall data across 12 coal mines in the USA. The prediction is nearly identical for individual mines, but when multiple mines are evaluated it is difficult to find a single best fit distribution for annual roof fall frequency. The BN approach with TNormal distribution was twice as likely to fit the observed data compared to the Poisson distribution assumed in the past. A hybrid approach using BN combining multiple probability distribution curves from historical data to predict annual roof fall is proposed. The BN models can account for variability for multiple parameters without increasing the complexity of the calculation. BNs can work with varying amounts of data, which makes them a good tool for real-time risk assessment in mines.

## Keywords

Bayesian network; expert opinion models; geotechnical risk; incident forecasting; parameter learning; roof fall risk.

## Introduction

Geotechnical risks increase as mines progress deeper, and these risks are commonly managed using probability-based risk assessment (Dershowitz and Einstein, 1984; Galvin, Hebblewhite, and Salmon, 1999; Baecher and Christian, 2003; Mishra *et al.*, 2017). The challenge with this approach is the lack of suitable data. Often there is not enough data for probability distributions, and historical data cannot be used for new projects in areas with no prior mining activities. The risk assessment is often subjective and qualitative, based on expert judgement. This paper aims to present the use of Bayesian networks (BNs) as an alternative method for risk assessment in underground mines. Spalling depth and roof collapse predictions are used as examples.

While qualitative assessment helps to carry out a quick risk assessment in the absence of data, it can be very broad and vague and can be highly influenced by personal opinion and bias. The variability of the condition of the rock mass compounds the problem as operations can run into previously unknown geological structures. Mining at great depth also means that collecting geotechnical information through conventional methods such as core drilling is very expensive. Non-intrusive geophysical methods involve limitations of coverage, range, and accuracy. Because of the uncertainty of geotechnical conditions with increased depth (*e.g.* geological contacts, rock properties), a formal geotechnical risk assessment outlining the scope, methodology, and resource requirement is preferable (Mishra and Rinne, 2014). The risk management framework should have a feature that enables it to learn from the data gained as mining progresses deeper.

Where historical frequencies of incidents are available, appropriate probability distributions can be used to forecast future failures. Duzgun and Einstein (2004) demonstrated the use of the Poisson distribution to forecast roof collapses in coal mines. Given the variability in mining conditions associated with each roof failure, it is often difficult to select one distribution which best describes all roof collapses. This paper extends their work by performing parameter learning on roof fall data across 12 mines and 1141 roof fall incidents to create probability distributions.

When extensive data is available, analytical design methods can be used to calculate the factor of safety. Significant variability in data can lead to conservative and expensive reinforcement design.

## A Bayesian network approach for geotechnical risk assessment in underground mines

Probabilistic analyses (PoF) account for the variability in data and are often used today, as opposed to deterministic analyses. This paper combines the factor of the safety method for reinforcement design against roof collapse in underground mines with a Bayesian network to address the variability of the underlying data.

Risk assessment methodologies and approaches for the underground mining industry have been discussed extensively in the past (Brown, 2012; Mishra and Rinne, 2014; Eskesen *et al.*, 2004; Paté-Cornell and Dillon, 2006; Paté-Cornell, 2007). Einstein and Baecher (1983) proposed that mining projects should be evaluated for their geotechnical risk levels through Geotechnical Risk Classification (GRC) from as early as the pre-feasibility study, and these values should be updated as the project progresses and more data becomes available. Kelly and Smith (2009) discussed the current state of the art of Bayesian inference in probabilistic risk assessment. Work has been done in the past using Bayesian networks to model major accidents using near misses (Khakzad, Khan, and Paltrinieri, 2014). Bayesian networks have also been used in dam risk assessment (Smith, 2006; Li, Yan, and Shao, 2007), tunnel risk assessment (Sousa and Einstein, 2007; Spackova and Straub, 2011), modelling uncertainties in rockfall hazards (Sousa and Einstein, 2012), safety assessment in construction projects (Zhang *et al.*, 2014), and dynamic failure assessment in process plants (Meel and Seider, 2006). This paper discusses the use of BNs to convert probabilistic risk assessment from a frequentist approach to a Bayesian approach. It demonstrates how BNs can be used as an alternative to test the goodness of fit of competing probability distributions.

### Methodology

Geotechnical risk is defined as a product of the likelihood of the geotechnical hazard and the severity of the consequence if the hazard were to be realized. Bayesian networks can be used to carry out both the likelihood and consequence assessment for a given hazard. In this paper, a BN has been used only to evaluate the likelihood of a roof or block collapse.

Bayesian networks or Bayesian belief networks are based on Bayes' theorem (Bayes and Price, 1763). They describe the conditional relationship between two or more variables using probability as defined in Equation [1].

$$P(H|E) = [P(E|H) \times P(H)]/P(E) \quad [1]$$

where  $H$  and  $E$  represent a hypothesis ( $H$ ) being tested and corresponding evidence ( $E$ ) to support this hypothesis.  $P(H|E)$  is called the posterior probability, which is the probability of the hypothesis ( $H$ ) being true given particular evidence ( $E$ ).  $P(E|H)$  is called the likelihood, which is the probability of observing evidence ( $E$ ) if the hypothesis were true.  $P(H)$  is called the priori, which is the prior belief in the hypothesis.  $P(E)$  is called the marginal likelihood, which represents the prevalence of the evidence in the base population. For instance, in a mining context, it is assumed that large angular discontinuities cause roof collapse. This assumption can be treated as one of several hypotheses in BNs that lead to roof collapse.  $P(H|E)$  for this hypothesis can be written as  $P(\text{large angular discontinuity} / \text{roof collapse})$ .  $P(\text{large angular discontinuity})$ , or the priori, would be the frequency rate of large angular discontinuities in the mine, such as an 'average of 10 discontinuities per mine'.  $P(\text{roof collapse})$ , or the marginal likelihood, would be the frequency rate

of the roof collapses, such as 'two roof collapses per year'.  $P(\text{roof collapse} / \text{large angular discontinuity})$ , or the likelihood, would be the number of times a large angular discontinuity caused a roof collapse, such as 'one out of two roof collapses was caused by large discontinuities'.

Figure 1 shows the structure of a BN which has been modified from work by Smith (2006) to split the model into a causal model, a BN, and a decision-making model.  $H_1$  and  $H_2$  are examples of two hypothesis nodes leading to the evidence node  $E$ . The hypothesis and evidence nodes, along with the solid directional arrows, form the causal model. The circular nodes and solid arrows form the BN causal model, while the dotted arrows represent the flow of information in a BN. The circular nodes at the origin of the solid arrows are called 'parent' nodes ( $P(H_1)$ ,  $P(H_2)$ ), while the nodes at the end of the solid arrows are called 'child' nodes.

Relationships between the nodes are defined with the use of priors and conditional probability tables or cause-effect relationship tables. This model can now be used to evaluate the likelihood of the evidence if the hypothesis is true. This form of inferencing from hypothesis to evidence is called forward inferencing. Observed data can be fed into the same model to back-calculate the likelihood of the hypothesis being true through backward inferencing. This process of forward and backward inferencing creates a decision-making model. The process helps to evaluate and update our prior beliefs in the light of new evidence and thus improve predictions.

The network shown in Figure 1 can now be converted to carry out risk assessment by defining the risk being assessed as the evidence and the contributing factors as hypotheses. The same model can also be used to carry out backward inferencing and parameter learning (Fenton and Neil, 2012). To carry out parameter learning, the unknown parameter is defined as the evidence, such as the mean and variance for a normal distribution. The available data is entered into the hypothesis nodes, and the model is solved using Equation [1] to arrive at the likely value for the unknown parameter. All the BNs in this paper are created and solved using Agena Risk version 7 (Agena, 2017). Several Bayesian network modelling software packages are available to carry out the modelling. Agena Risk was chosen over the others because of its ability to deal with continuous

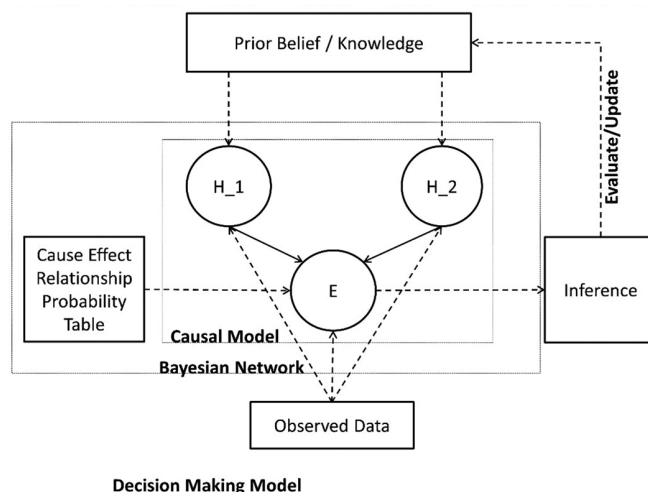


Figure 1—Decision-making model using a Bayesian network. Circular nodes and solid arrows show the causal model, and dotted arrows show the flow of information (after Smith, 2006)

# A Bayesian network approach for geotechnical risk assessment in underground mines

variables along with non-numeric nodes. Comprehensive literature on the use of Agena Risk (Fenton, Neil, and Caballero, 2007; Fenton and Neil, 2012) across multiple cases was available, which assisted in the modelling of incidents.

## Spalling depth forecasting using BN and analytical methods

This section discusses the concept of combining analytical methods for estimating the potential for spalling depth in tunnels with BNs. The usage of BNs allows the variability in the collected data to be taken into account better. To enable a direct comparison with existing frequentist methods, we have chosen a case example where a lot of data is available. To demonstrate the use of a BN in conjunction with the analytical method, we have used the spalling estimation method as described by Martin and Christiansson (2009) and the Olkiluoto case data from Siren *et al.* (2011). The Olkiluoto case describes a high-level spent nuclear fuel repository at a depth of 420 m in hard crystalline rock in Finland.

The failure mechanism that is studied is the formation of thin slabs. Progressively, these slabs form a continuous wedge of spalled material. To establish the size of the wedge to be supported with tunnel reinforcement, the analytical method requires the uniaxial compressive strength (UCS) of the rock and local principal stresses to be known. The factor of safety (FoS) for the roof reinforcement can then be calculated using Equation [2]:

$$FOS = \frac{\sigma_{sm}}{\sigma_{\theta\theta}} \quad [2]$$

where  $\sigma_{sm}$  is the rock spalling strength and  $\sigma_{\theta\theta}$  is the tangential stress at the rock surface. The spalling strength is extracted from the UCS of the rock by multiplying by a scaling factor,  $k$ . For Olkiluoto, UCS is represented by a normal distribution with a mean of 115 MPa and a standard deviation of 23 MPa (Siren *et al.*, 2011), and  $k = 0.57 \pm 0.02$  has been used for crystalline rock (Martin and Christiansson, 2009). At a depth of 400 m, the major horizontal stress and minor vertical stresses were taken as in Posiva (2009), and to account for data variability both of these were represented by triangular distributions with corners in the lower 10% fractile, the mean, and the upper 90% fractile (Table 1). Using the Kirsch (1898) equations (Equation [3]), these values can be used to calculate the resulting tangential stress at the rock surface. The shape factor  $A = 2.60$  was obtained as a median value calculated from the profiles listed in Siren *et al.* (2011). The uncertainty of the stress direction is omitted for the sake of simplicity.

$$\sigma_{\theta\theta} = A\sigma_1 - \sigma_3 \quad [3]$$

The FoS (Equation [2]) can now be calculated (Equation [4]). Using the mean values the FoS becomes

$$FOS = \frac{\sigma_{sm}}{\sigma_{\theta\theta}} = \frac{k \cdot UCS}{A\sigma_1 - \sigma_3} = \frac{0.57 \cdot 115 \text{ MPa}}{2.60 \cdot 25.6 \text{ MPa} - 10.6 \text{ MPa}} = 1.17 \quad [4]$$

indicating a small risk of spalling damage at Olkiluoto, according to Siren *et al.* (2011). The damage depth can be calculated with Equation [5] modified after Martin and Christiansson (2009):

$$S_d = a \left( 0.5 \frac{\sigma_{\theta\theta}}{\sigma_{sm}} - 0.52 \pm 0.1 \right) \quad [5]$$

Assuming the nominal tunnel radius to be  $a = 5$  m, the corresponding mean damage depth ( $S_d$ ) is zero ( $-0.46$  m) and the extreme value using the  $+0.1$  upper limit would, at a maximum, be 0.037 m.

The empirical factor  $0.52 \pm 0.1$  describing the observed damage depth in Martin and Christiansson (2009) was modelled using a triangular distribution with a lower limit of 0.42, mode of 0.52, and upper limit of 0.62. The empirical factor is based on nine published case histories (Andersson, 2005; Martin *et al.*, 2001) in a wide range of rock mass conditions and major *in-situ* stresses ranging from 10 MPa to 140 MPa. The rock types consisted of limestone (UCS 80 MPa), andesite (UCS 100 MPa), granite (UCS 220 MPa), and quartzite (UCS 350 MPa). The variability of  $\sigma_1$ ,  $\sigma_3$ , and  $k$  means that there will be combinations that exhibit spalling despite the FoS being greater than unity.

For spalling strength, the factor  $k$  was modelled using a triangular distribution with a lower limit of 0.55, mode of 0.57, and upper limit of 0.59, as suggested in Martin and Christiansson (2009) for crystalline rocks. It should be noted that the factor  $k$  is defined for the mean UCS and the UCS is not entered as a distribution. The model allows for any combination of strength and stress, while in reality high stresses are more likely in strong rock and low stresses in weak rock. For weak rocks, the model may result in conservative results. The model may incorrectly predict the spalling phenomenon occurring in weak rocks or the occurrence of high stresses in weak rocks. The analytical method does not reveal what the spatial extent or probability of such damage is. The site-specific acceptance criteria as a function of FoS can be selected based on site-specific observations of FoS when there is no spalling, very minor spalling, or extensive spalling, as suggested in Martin and Christiansson (2009).

For a true deterministic example, the FoS will need to be calculated individually for all combinations of variables. This method requires extensive data collection. In reality, frequentist probability methods are used in conjunction with random sampling (*e.g.* Monte Carlo) or structured sampling (*e.g.* Latin hypercube sampling). The disadvantage of the frequentist probabilistic method is that the complexity of the model grows exponentially as the number of uncertain variables increases beyond two (Matarawi and Harrison, 2017). Additionally, the FoS values do not directly give the probability of failure (PoF), but prescribed tables can be used to compare FoS and PoF (Galvin, Hebblewhite, and Salmon, 1999).

Bayesian networks can be used to take the variability into account directly. Accounting for variability eliminates any need to use FoS and establishes the PoF directly. Figure 2 shows the PoF calculation using the BN. The  $\sigma_1$  and  $\sigma_3$  nodes were used to calculate  $\sigma_{\theta\theta}$  using Equation [3]. The  $\sigma_{sm}$  node was obtained by multiplying the empirical factor  $k$  by the mean UCS of 115 MPa. Factor of safety and spalling depth nodes were obtained using Equations [2] and [5] respectively. The BN model predicts a 92.3% chance that the FoS will be greater than unity, while

Table 1

### Major horizontal stress and minor vertical stress at Olkiluoto at a depth of 400 m. (Posiva, 2009)

Variable parameter	Lower bound 10%	Upper bound 90%	Mean
Major horizontal stress, $\sigma_1$ [MPa]	19.6	31.6	25.6
Minor vertical stress, $\sigma_3$ [MPa]	9.6	11.7	10.6

## A Bayesian network approach for geotechnical risk assessment in underground mines

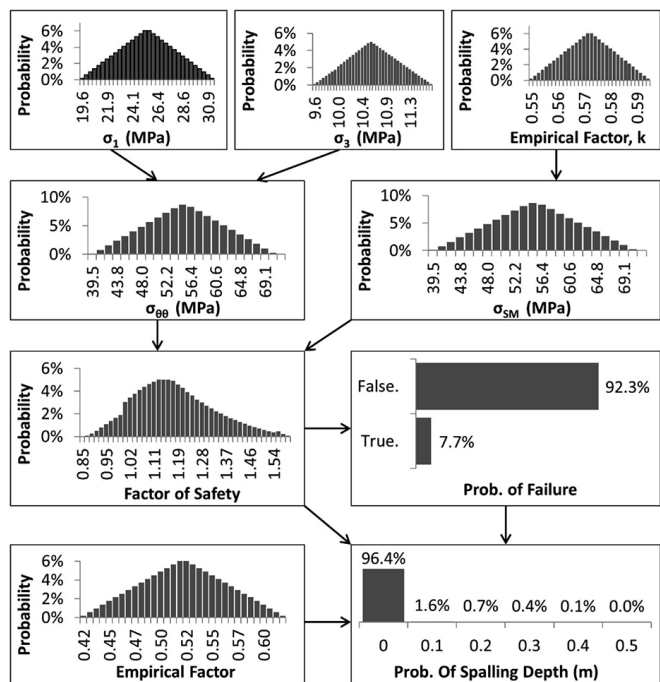


Figure 2—Bayesian network model to forecast spalling and spalling depth using Equations [2], [3], and [4]. Equations [2] and [3] are solved to give 'factor of safety' nodes. Equation [5] is solved using the 'factor of safety' and 'empirical factor' nodes to provide the spalling depth

deterministic calculation using Equation [2] would have resulted in a single FoS value of 1.17. BNs can thus take into account the variability of multiple variables in analytical assessment to make failure predictions. In the presented example, the analysis was carried out in the least favourable direction. If the actual tunnel direction is known, the BN can be expanded to include the variability of the stress orientations. The current approach with the empirical factor  $k$  requires the usage of the mean UCS value. If the distribution of UCS is known, the crack initiation strength can be taken as a lower bound estimate for the spalling initiation strength as formation of cracks precedes the onset of spalling.

### Roof collapse forecasting using BN with roof fall frequency data

#### Parameter learning on roof fall frequency data for roof fall forecasting

This section discusses the use of parameter learning in a BN to learn distributions from historical roof collapse data in coal mines. It considers the example of roof fall risk estimation using roof fall frequency data collected by the Mine Safety and Health Administration (MSHA) in coal mines situated in the USA. The data is from the period between 1979 and 1997 across 12 anonymized underground mines in the Appalachian region (Duzgun and Einstein, 2004; Mine Safety and Health Administration, 2000). This data has been analysed in the past by curve fitting the accident frequency to an appropriate probabilistic distribution to forecast failure (Duzgun and Einstein, 2004; Einstein, 1997). Mine ID 4601816 was considered for the parameter learning demonstration as it had the largest sample size, with 108 roof fall incidents. Figure 3 shows the annual frequency of the number of roof falls (NoF) in Mine ID 4601816.

Duzgun and Einstein (2004) used an exponential distribution for the time between failures and a Poisson distribution for

the annual roof fall frequency (NoF) to fit the roof fall data for roof fall prediction. The Poisson distribution is a one-parameter probability distribution as shown in Equation [6] for annual roof fall frequency.

$$P(NoF) = e^{-\lambda} \times (\lambda^{NoF} / NoF!) \quad [6]$$

The Poisson parameter lambda ( $\lambda$ ) is the mean roof fall frequency per year and NoF is the annual roof fall frequency whose probability of occurrence ( $P(NoF)$ ) is being evaluated. Parameter  $\lambda$  for the roof fall frequency for the abovementioned mine is 5.68, using data from Figure 3. In the frequentist approach to risk assessment one value of  $\lambda$  is used to plot the probability distribution. Any frequentist interpretation of a statistical parameter is referred as the 'classical approach' in this paper.

The Bayesian approach to solving this problem considers the  $\lambda$  parameter of the Poisson distribution as a variable itself. The parameter learning capabilities of the BN can then be used to learn the lambda parameters from the population. Figure 4 shows the BN used to learn the probability distribution of  $\lambda$ . The parent node lambda ( $\lambda$ ) was assumed to have a uniform prior probability between 0 and 20. Uniform prior probability implies that all values between 0 and 20 had the same probability of being equal to  $\lambda$ . The child nodes to this parent are the number of roof failures occurring in different years, with the annual roof fall frequency on the x-axis and probability distribution (PD) on the y-axis. The conditional probability between lambda and roof fall node is defined by the Poisson equation as shown in Equation [6]. Nineteen child nodes were added to the BN to enter roof fall frequency data available for 19 years, as shown in Figure 4 from Y1 to Y19. An additional node named 'forecasted NoF' was added to show the results of the parameter learning to give the revised roof fall frequency. The BN was solved using the parameter learning to revise the  $\lambda$  distribution from the prior uniform distribution. The revised distribution, in turn, provided the 'predicted roof fall frequency'. As the evidence for year 20 becomes available, it can then be added as an additional child node, which will then revise both the  $\lambda$  and predicted roof fall frequency distribution in the light of the additional evidence.

When the Bayesian prediction of annual roof fall frequency (NoF) probability distribution (PD) is compared with the classical Poisson distribution obtained from Equation [6], the Bayesian prediction is nearly identical, as shown in Figure 5. Despite being almost identical in probability distribution, both the classical

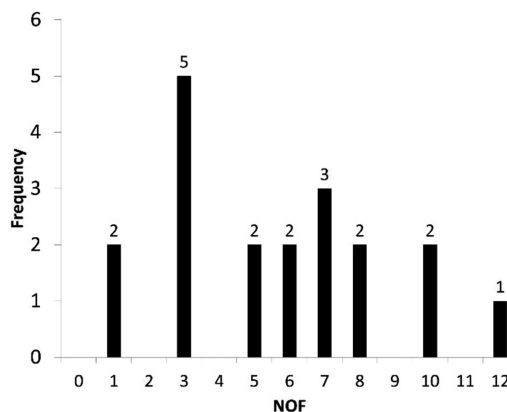


Figure 3—Annual roof fall frequency in Mine 4601816. Number of roof falls (NoF)

# A Bayesian network approach for geotechnical risk assessment in underground mines

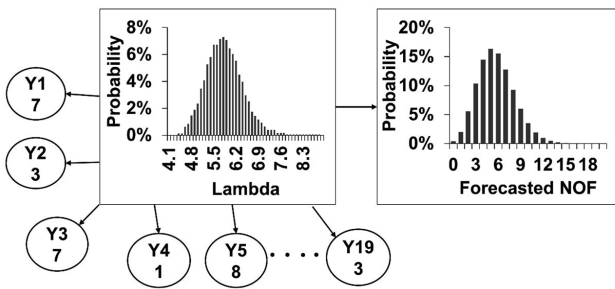


Figure 4—Parameter learning BN to learn lambda ( $\lambda$  = mean roof falls per year) from observed roof falls. The y-axis shows the probability distribution, while the x-axis shows the different values of lambda and forecast annual roof falls for the left and right nodes

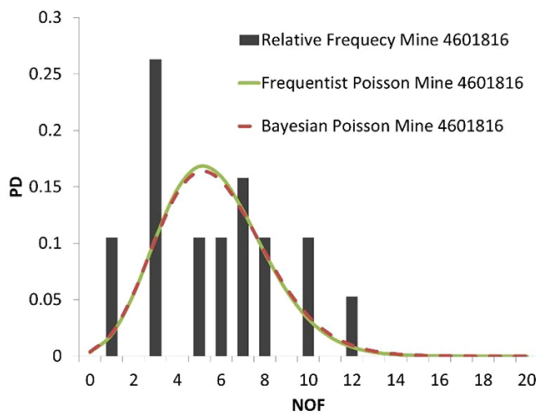


Figure 5—Classical Poisson vs Bayesian Poisson comparison for annual roof fall (NoF) probability for Mine 4601816

and Bayesian curves are a poor fit to the observed data when a Poisson distribution is assumed. A mathematical comparison of goodness of fit of competing distributions is discussed later in the paper.

The data for Mine 460186 was then assumed to follow a normal distribution with mean and variance replacing  $\lambda$  as the parent node. The normal distribution was limited to a lower tolerance of zero annual roof falls and an upper tolerance of 20 annual roof falls, resulting in a truncated normal or TNormal distribution (Thompson, 1950). In order to avoid unreal results of non-integer annual roof falls, the TNormal distribution was constructed using integer intervals in Agena Risk (Agena, 2017). The mean and variance parameters were assumed to have uniform priors. The mean and variance parameters for the normal distribution were learned using parameter learning from the observed data for 19 years, similarly to that carried out in Figure 4. The resulting Bayesian network is shown in Figure 6, while a comparison of the classical Poisson distribution, Bayesian TNormal distribution, and the actual observed data is shown in Figure 7.

The relative error of the forecast value was carried out using Equation [7] for both the Poisson and normal distribution (ISO, 1993).

$$E = \frac{\sqrt{(P_n - RF_n)^2}}{RF_n} \quad [7]$$

where  $E$  is the relative error in the forecast data,  $P_n$  is the forecast probability of  $n$  roof falls in a year, and  $RF_n$  is the relative frequency of  $n$  roof falls. Using Equation [7], the average relative

error in the forecast using classical Poisson distribution was 55%, which was reduced to 37% when the Bayesian TNormal distribution was used.

## Using 'goodness of fit' results from multiple distributions for roof fall forecasting

There are mathematical tests, such as Kolmogorov-Smirnov test and the chi-square goodness of fit test, that can be carried out to evaluate how well a proposed distribution fits the data (Ang and Tang, 1984). These tests use statistical parameters such as the mean, which is not directly observed in the population but is inferred from a sample population. An alternative method using BN is to evaluate the frequency with which the historical data (evidence) occurs in the assumed probability distribution (hypothesis) (Fenton and Neil, 2012). This can be modelled using a BN where several probability distributions, in this case truncated normal and Poisson distribution, form the node states for a parent node (Figure 8).

The child nodes are values observed in each of the 19 years for Mine 4601816. The prior probability of the parent node 'Competing distributions' is considered to be 50% for each, meaning that both the distributions are equally likely to be correct. The conditional probability table for the child node is conditional on the parent nodes as shown in Table II for the node 'Roof fall Y\_1'.

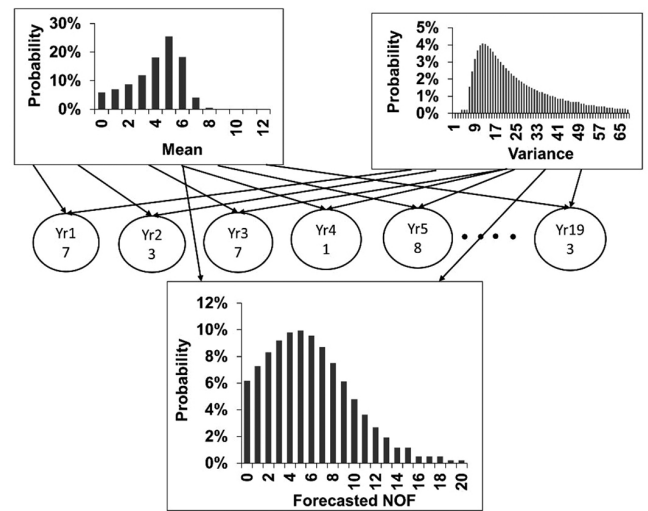


Figure 6—Parameter learning BN to learn normal distribution parameters from observed roof falls

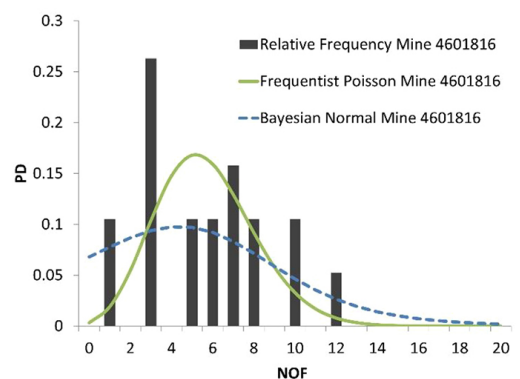


Figure 7—Classical Poisson vs Bayesian normal comparison for roof fall probability in Mine 4601816. Summary statistics of the two graphs are shown in Table II

## A Bayesian network approach for geotechnical risk assessment in underground mines

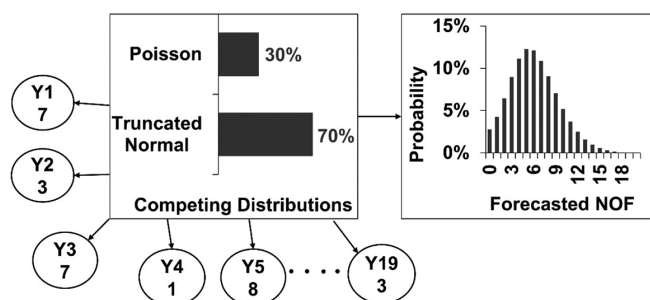


Figure 8—Goodness of fit test for competing distributions using BN. Roof fall data from 19 years is used to determine the goodness of fit of the competing distribution. Goodness of fit results are used to provide a weighted roof fall forecast

Table II

### Node probability table showing the relation between competing distributions and roof fall frequency

Competing distribution	Probability distribution
Truncated normal	TNormal (5.75, 16.4, 0, 20)
Poisson	Poisson (5.68)

The values in parentheses for TNormal represent the mean, variance, lower bound, and upper bound respectively, while the values in parentheses for Poisson show the  $\lambda$ . These are statistical summary parameters of the Poisson and normal distributions shown in Figure 7. This BN is solved by entering roof fall values from year 1 to year 19, resulting in a posterior probability of 70% for the Bayesian TNormal distribution and 30% for the classical Poisson distribution. The posterior probabilities imply that there is a 70% probability of observing the given data under the Bayesian normal distribution, compared to 30% under the classical Poisson distribution. In other words, the observed data is more than twice as likely under the Bayesian TNormal distribution compared to the Poisson distribution. Therefore, Bayesian TNormal is a better model for forecasting the roof fall frequency in Mine 4601816. This goodness of fit test using the observed parameters was carried out for all 12 mines, and the Bayesian TNormal distribution was found to be a better fit compared to classical Poisson distribution in seven of the 12 mines. The results of this analysis are shown in Table III.

These results indicate that it is unlikely to have one distribution that is the best fit for roof fall data across different mines. Bayesian networks can overcome this problem by creating a hybrid distribution curve weighted according to the goodness of fit test results. The percentage probability values indicate which of the two distributions is more likely to fit the data better when they are compared. For example, if both truncated normal and Poisson distributions are used to forecast a roof fall in Mine 4601816, the forecast is weighted 70% in favour of normal distribution and 30% in favour of Poisson distribution as obtained from the goodness of fit test. Hybrid distributions can be useful in early stages of data collection, where limited data makes it difficult to identify a unique distribution that correctly represents the population. The number of distribution should be limited to two or three as the intention of the hybrid model is to evaluate potential distributions that are expected to describe the population. As additional information becomes available over time, the one distribution that best describes the population should be chosen from the hybrid distribution.

### Discussion

#### Bayesian networks for real-time risk assessment

Geotechnical incidents in deep mines can have severe consequences due to both unfavourable mining conditions and the difficulty of rescue and recovery operations following an incident. Real-time risk assessment can help mitigate both the hazard and the consequences through advance warning. Bayesian networks can work with varying amounts of data, which makes them a good tool to carry out a real-time risk assessment at mine sites. Bayesian networks can either be integrated with the existing on-site information management system or strategic instrumentation and monitoring can be implemented once the Bayesian model has been defined.

The process of incorporating real-time risk assessment using BNs is shown in Figure 9. The first step in the process is to define a causal model for a failure such as stope collapse using nodes and probability tables. The contributing nodes can be numeric nodes with continuous values such as stress around the stope, the number of discontinuities, roof convergence, *etc.* Alternatively, these nodes can be non-numeric, with subjective states such as the quality of the filling in of the discontinuities. If the nodes are non-numeric, the prior probability of each of the nodes will have to be defined. Numeric nodes can consist

Table III

### Goodness of fit test results for classical Poisson and Bayesian TNormal distribution for roof fall frequency

Mine ID	Poisson parameter $\lambda$	Bayesian TNormal parameter		Probability of observed data	
		Mean	Variance	Classical Poisson	Bayesian TNormal
4601816	5.68	5.75	16.40	30%	70%
1502709	3.26	3.42	5.06	62%	38%
1503178	3.00	6.19	20.83	10%	90%
0100758	5.36	5.39	5.84	58%	42%
1502132	1.89	2.35	4.20	68%	32%
1502502	3.80	3.85	5.31	27%	73%
1504020	1.81	2.51	5.25	81%	19%
1512941	2.43	3.10	7.12	52%	48%
1513920	4.75	5.97	20.71	18%	82%
1514492	7.15	8.21	30.41	1%	99%
3600958	3.53	4.02	10.00	19%	81%
4605978	2.70	2.25	4.21	29%	71%

## A Bayesian network approach for geotechnical risk assessment in underground mines

of information which is collected, in real time, such as roof convergence measurement using an extensometer, or seismicity using geophones. For these nodes, appropriate site-wide instrumentation needs to be planned in such a way that sufficient data is collected, and their prior probabilities are defined using probability distribution. Numeric nodes can also consist of data, which is collected intermittently through inspection and is not continuous. Joint set numbers, joint roughness, blast vibrations, *etc.* fall into the category of non-continuous numeric nodes. Either these nodes can be defined using a probability distribution or the distribution can be learnt using parameter learning.

After the nodes and their prior probabilities have been defined, the BN is solved for the current risk level on the basis of the available information. As data is fed from real-time instrumentation, the risks are updated in real time to inform the relevant stakeholders. The same network can also be used to feed information on incidents and near misses that occur in the mine to carry out backward inferencing and revise all the prior probabilities. This method also assists with incident investigation to identify the most likely cause of the incident and improve the accuracy of the forecasting model.

### Advantages and limitations of Bayesian network-based risk assessment

Bayesian networks offer the flexibility of working in the absence of historical data by replacing it with expert opinion-based prior probabilities. In conventional frequentist risk assessment, a summary of statistical parameters such as the mean and median is often used to carry out the risk assessment. Even when the full probability distribution is used, the computational requirements increase significantly as the number of parameters increases. BNs, however, can work with complex causal models where each node uses a probability distribution instead of summary statistics. Expert opinion-based risk assessment implies that a BN can quickly adapt to an existing subjective risk assessment practice in the mine. This improves the repeatability of the risk assessment process when performed by different personnel for

the same mine. Its ability to perform backward inferencing on a risk assessment model allows the BN to be used for incident investigation. This iterative process of risk forecasting and incident investigation improves the reliability of the model by updating the assumed prior probabilities. Backward inferencing also encourages improved collection of data and rigorous incident investigations. The ability of BNs to work with site instrumentation opens up the possibility of creating a real-time risk assessment and warning system in a mine.

The use of expert opinions in the absence of data is also one of the main disadvantages of BN-based risk assessment. Incorrect prior probabilities lead to incorrect incident forecasts, which need to be validated through incident investigations in the future. The additional poor understanding of incident causation and failure mechanism also results in incorrect forecasts. Given the reliance on experts, it is prone to human error and expert biases. Real-time risk assessment using BNs can be challenging if a large part of the mine needs to be monitored for risk, as this would require extensive instrumentation, which can be expensive. Additionally, BNs can only work on the basis of an underlying causal model. Modelling error or the omission of key influencing factors can lead to incidents not predicted by the warning system. However, after every incident, backward inferencing should be carried out to test whether the causal model explains the incident. If not, additional investigation and instrumentation are necessary in order to improve the warning system.

### Conclusions

Bayesian networks provide a flexible framework for carrying out risk assessment from zero to scarce to an abundant amount of measured data available. They can take into account the full variability of source data by the use of probability distributions. Spalling depth and the risk of roof fall were analysed using the Bayesian approach as an alternative to the analytical method. This approach was also used to convert the factor of safety calculation for spalling into a probability of whether spalling will happen. If spalling takes place, what are the probabilities of

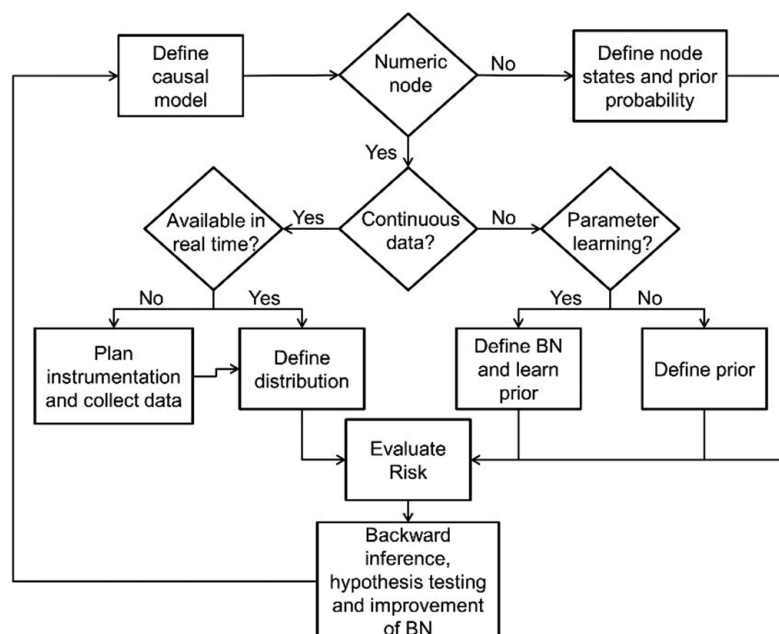


Figure 9—Real-time risk management process flow using BN

# A Bayesian network approach for geotechnical risk assessment in underground mines

various spalling depths?

Parameter learning using BNs was demonstrated using roof fall data across 12 mines over 19 years. The results show the weakness in applying a single type of probability distribution that provides the best fit for roof fall frequency in all the mines that were studied. A methodology of combining multiple distributions to produce a weighted forecast was proposed to overcome the challenge of a best fit from a single probability distribution in the presence of limited data. This study indicates that BNs may present a good platform for a real-time risk assessment tool by combining expert knowledge with available data, including online measurements from the field.

## Acknowledgement

The authors gratefully acknowledge the financial support provided by the Online Risk Management in Deep Mines (ORMID) project funded by the Academy of Finland under the grant no. 297770.

## References

- AGENA. 2017. AgenaRisk: Bayesian network and simulation software for risk analysis and decision support. 7th edn. Cambridge, UK.
- ANDERSSON, C. 2005. Äspö pillar stability experiment. Bergmekanikdag. Franzén, T. (ed.). SveBeFo, Stockholm. pp. 69–78.
- ANG, A.H. and TANG, W.H. 1984. Probability Concepts in Engineering Planning and Design. Wiley, New York.
- BAECHER, G.B. and CHRISTIAN, J.T. 2003. Reliability and Statistics in Geotechnical Engineering. Wiley, Chichester.
- BAYES, M. and PRICE, M. 1763. An essay towards solving a Problem in the Doctrine of Chances. by the late Rev. Mr. Bayes, F.R.S. communicated by Mr. Price, in a letter to John Canton, A.M.F.R.S. *Philosophical Transactions (1683-1775)*. pp. 370–418.
- BROWN, E.T. 2012. Risk assessment and management in underground rock engineering—An overview. *Journal of Rock Mechanics and Geotechnical Engineering*, vol. 4. pp. 193–204.
- DESHOWITZ, W.S. and EINSTEIN, H.H. 1984. Application of artificial intelligence to problems of rock mechanics. *Proceedings of the 25th US Symposium on Rock Mechanics (USRMS)*, Evanston, Illinois. American Rock Mechanics Association, Alexandria, VA.
- DUZGUN, H.S.B. and EINSTEIN, H.H. 2004. Assessment and management of roof fall risks in underground coal mines. *Safety Science*, vol. 42. pp. 23–41.
- EINSTEIN, H. 1997. Landslide risk - Systematic approaches to assessment and management. *Proceedings of the International Workshop on Landslide Risk Assessment*, Hawaii, USA. A.A. Balkema, Rotterdam. pp. 25–50.
- EINSTEIN, H.H. and BAECHER, G.B. 1985. Probabilistic and statistical methods in engineering geology. *Rock Mechanics and Rock Engineering*, vol. 16. pp. 39–72.
- ESKESEN, S.D., TENGBORG, P., KAMPMANN, J., and VEICHERTS, T.H. 2004. Guidelines for tunnelling risk management: International Tunnelling Association, Working Group No. 2. *Tunnelling and Underground Space Technology*, vol. 19. pp. 217–237.
- FENTON, N. and NEIL, M. 2012. Risk Assessment and Decision Analysis with Bayesian Networks. CRC Press, Boca Raton, FL.
- FENTON, N.E., NEIL, M., and CABALLERO, J.G. 2007. Using ranked nodes to model qualitative judgments in Bayesian networks. *IEEE Transactions on Knowledge and Data Engineering*, vol. 19. pp. 1420–1432.
- GALVIN, J., HEBBLEWHITE, B., and SALMON, M. 1999. Coal pillar strength determinations for Australian and South African mining conditions. *Proceedings of the Second International Workshop on Coal Pillar Mechanics and Design*, Colombia. DHHS (NIOSH) Publications. Washington, D.C. pp. 63–70.
- ISO. 1995. Guide to the Expression of Uncertainty in Measurement. International Organization for Standardization, Geneva.
- KHAKZAD, N., KHAN, F., and PALTRINIERI, N. 2014. On the application of near accident data to risk analysis of major accidents. *Reliability Engineering & System Safety*, vol. 126. pp. 116–125.
- KELLY, D.L. and SMITH, C.L. 2009. Bayesian inference in probabilistic risk assessment—The current state of the art. *Reliability Engineering & System Safety*, vol. 94. pp. 628–643.
- KIRSCH, C. 1898. Die theorie der elastizität und die bedürfnisse der festigkeitslehre. *Zeitschrift des Vereines Deutscher Ingenieure*, vol. 42. pp. 797–807.
- LI, D., YAN, L., and SHAO, D. 2007. Reliability evaluation of earth-rock dams using Bayesian network. *Engineering Journal of Wuhan University*, vol. 40. pp. 24–29.
- MARTIN, C. and CHRISTIANSSON, R. 2009. Estimating the potential for spalling around a deep nuclear waste repository in crystalline rock. *International Journal of Rock Mechanics and Mining Sciences*, vol. 46. pp. 219–228.
- MARTIN, C.D., CHRISTIANSSON, R., and SÖDERHÄLL, J. 2001. Rock stability considerations for siting and constructing a KBS3 repository: based on experiences from Äspö HRL, AECL's URL, tunnelling and mining. Technical Report TR-01-38. Swedish Nuclear Fuel and Waste Management Co., Stockholm.
- MATARAWI, A.E. and HARRISON, J.P. 2017. Calibrated partial factors for support of wedges exposed in tunnels. *Procedia Engineering*, vol. 191. pp. 802–810.
- MEEL, A. and SEIDER, W.D. 2006. Plant-specific dynamic failure assessment using Bayesian theory. *Chemical Engineering Science*, vol. 61. pp. 7036–7056.
- MINE SAFETY AND HEALTH ADMINISTRATION. 2000. MSHA's mine data retrieval system <https://www.msha.gov/mine-data-retrieval-system> [accessed 15 April 2020].
- MISHRA, R. and RINNE, M. 2014. Guidelines to design the scope of a geotechnical risk assessment for underground mines. *Journal of Mining Science*, vol. 50. pp. 745–756.
- MISHRA, R.K., JANISZEWSKI, M., UOTINEN, L.K.T., SZYDLOWSKA, M., SIREN, T., and RINNE, M. 2017. Geotechnical risk management concept for intelligent deep mines. *Procedia Engineering*, vol. 191. pp. 361–368.
- PATÉ-CORNELL, M.E. 2007. The Engineering Risk Analysis Method and Some Applications. Cambridge University Press, New York.
- PATÉ-CORNELL, M.E. and DILLON, R.L. 2006. The respective roles of risk and decision analyses in decision support. *Decision Analysis*, vol. 3. pp. 220–232.
- POSIVA. 2009. Olkiluoto site description 2008. Report 2009-01. Eurajoki, Finland.
- SIREN, T., UOTINEN, L.K.T., and MARTINELLI, D. 2011. Assessment of the potential for rock spalling in the technical rooms of the ONKALO. Posiva, Eurajoki, Finland.
- SMITH, M. 2006. Dam risk analysis using Bayesian networks. *Proceedings of the ECI Conference on Geohazards*, Lillehammer, Norway. <https://dc.engconfintl.org/cgi/viewcontent.cgi?article=1030&context=geohazards>
- SOUSA, R. and EINSTEIN, H. 2007. Risk analysis for tunneling projects using Bayesian networks. *Proceedings of the 11th Congress of the International Society of Rock Mechanics, Lisbon*. Taylor and Francis. pp. 1301–1304.
- SOUSA, R.L. and EINSTEIN, H.H. 2012. Risk analysis during tunnel construction using Bayesian networks: Porto Metro case study. *Tunnelling and Underground Space Technology*, vol. 27. pp. 86–100.
- SPACKOVA, O. and STRAUB, D. 2011. Probabilistic risk assessment of excavation performance in tunnel projects using Bayesian networks: A case study. *Proceedings of the 3rd International Symposium on Geotechnical Safety and Risk*. Bundesanstalt für Wasserbau, München. pp. 651–660.
- THOMPSON, H. 1950. Truncated normal distributions. *Nature*, vol. 165. pp. 444–445.
- ZHANG, L., WU, X., SKIBIEWSKI, M. J., ZHONG, J., and LU, Y. 2014. Bayesian-network-based safety risk analysis in construction projects. *Reliability Engineering & System Safety*, vol. 131. pp. 29–39. ◆



# Navigation and positioning technology in underground coal mines and tunnels: A review

Y. Cui<sup>1,2</sup>, S. Liu<sup>1,2</sup>, and Q. Liu<sup>1</sup>

## Affiliation:

<sup>1</sup> School of Mechatronic Engineering, China University of Mining and Technology, Xuzhou, Jiangsu, 221116, China.

<sup>2</sup> Jiangsu Collaborative Innovation Center of Intelligent Mining Equipment, China University of Mining and Technology, Xuzhou, Jiangsu 221116, China.

## Correspondence to:

Y. Cui

S. Liu

## Email:

Cuiyuming1122@163.com

lsycumt@163.com

## Dates:

Received: 10 Dec. 2019

Revised: 23 Feb. 2021

Accepted: 29 Apr. 2021

Published: June 2021

## How to cite:

Cui, Y., Liu, S., and Liu, Q. 2021 Navigation and positioning technology in underground coal mines and tunnels: A review. *Journal of the Southern African Institute of Mining and Metallurgy*, vol. 121, no. 6, pp. 295–304.

## DOI ID:

<http://dx.doi.org/10.17159/2411-9717/1065/2021>

## ORCID

Y. Cui

<https://orcid.org/0000-0001-5648-1825>

## ORCID

S. Liu

<https://orcid.org/0000-0002-2801-7969>

## ORCID

Q. Liu

<https://orcid.org/0000-0002-7426-715X>

## Synopsis

To reduce the frequency of mining incidents and improve safety and production efficiency, it is important to develop technology for the autonomous positioning and navigation of mining equipment, without the assistance of satellite navigation signals. In this study we review the current technological environment for positioning and navigation underground and present several integrated navigation strategies. Existing underground positioning and navigation technology is described, and the performances of different methods based on this technology analysed and compared. The combination types and positioning effects of underground positioning and navigation strategies are discussed. Recent research directions for filtering methods and positioning estimation algorithms for underground positioning and navigation are reviewed. Finally, we summarize the future direction of underground positioning and navigation technology and related algorithms.

## Keywords

coal mining; underground positioning and navigation, integrated navigation strategy, inertial navigation, positioning algorithms.

## Introduction

Energy is the material basis for human survival and economic development. Coal, the demand for which continues to increase, accounts for approximately 25% of the world's primary energy supply. China's annual coal output from underground mines reached 3.3 billion tons in 2015. Shirong, Zhongbin, and Shibo (2016) surmised that there are more than 3 million miners in underground coal mines, working in harsh and dangerous conditions.

Figure 1 shows schematically the most important items of equipment. To ensure the coal mining and tunnelling equipment travels along the planned path and direction, the spatial position and running track of the equipment must be accurately determined. In the absence of satellite navigation signals, it is a difficult task to accurately determine the positioning and navigation of equipment and miners in underground coal mines due to the closed space and complex electromagnetic environment. Therefore, to mitigate mining safety risk and promote the technological revolution in coal mining, the development of intelligent and automatic navigation and positioning technology for miners and underground mining equipment is of great significance.

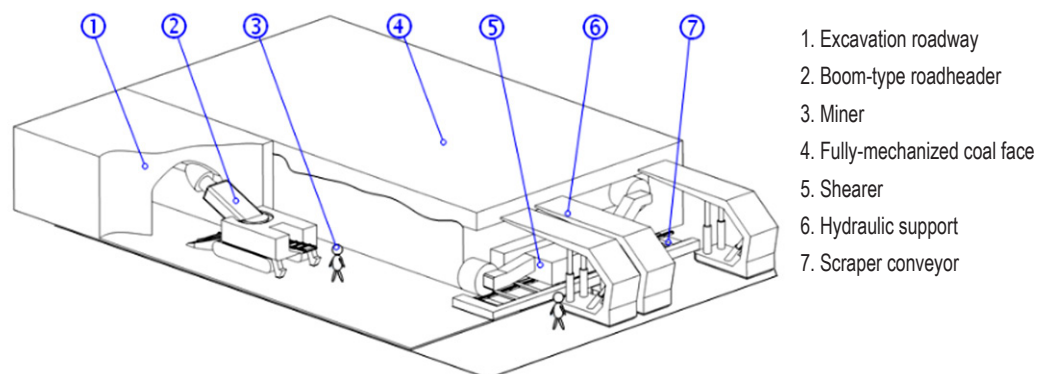


Figure 1—Schematic diagram of equipment and personnel layout in an underground coal mine

# Navigation and positioning technology in underground coal mines and tunnels: A review

## Underground positioning and navigation technology

According to the literature (Liu and Shi 2018), indoor navigation and location technology has become an important research topic internationally in recent years, and organizations and publications are keeping a watchful eye on developments. By the end of 2018, the number of intelligent mining faces in China had reached 145.

Numerous types of positioning and navigation technology and algorithms have been proposed and used for equipment and personnel positioning and navigation in underground mines and tunnels. According to the different detection principles, the existing technologies can be divided into the following categories:

- Intersection technology based on wireless communication signals
- Positioning technology based on visual image features
- Navigation technology based on inertial devices
- Positioning technology based on visible light communication (VLC).

The implementation difficulty and basic accuracy of several positioning and navigation technologies are shown in Figure 2 and Table I (Yassin *et al.*, 2016).

### Intersection measuring technology based on wireless communication signals

Technologies include laser scanning positioning, radio frequency

identification (RFID), Zigbee wireless, ultra-wideband (UWB), ultrasonic, and infrared positioning. This category of technologies can be divided into two kinds of distance measurement methods depending on the way in which signals are processed. Both methods estimate the specific positioning of the object by using the principle of trilateral and triangular positioning; however, the arrival time of spread spectrum signals and the attenuation of signal reception energy are used to complete the positioning methods.

### Positioning technology using visual image features

This kind of positioning technology relies mainly on the motion analysis of image features collected by a visual sensor. The distance between the object to be positioned and the environmental background features can be determined using the visual distance projection model or the background image difference method. Current research suggests that this technology can generally achieve decimetre-scale accuracy (Yassin *et al.*, 2016).

### Navigation technology using inertial devices

Inertial devices are important for navigation, orientation, and motion carrier control. They can be used to detect acceleration, angle, impact, vibration, rotation, and multiple degrees-of-freedom motion. Inertial navigation technology is a kind of autonomous navigation, which can continuously determine

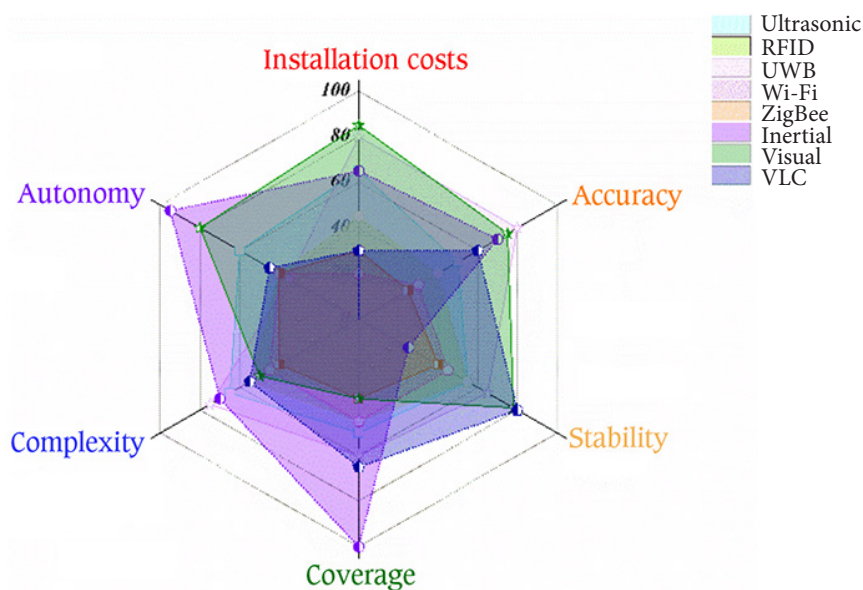


Figure 2—Practical performance of existing positioning and navigation technology (Yassin *et al.*, 2016)

Technology	Measures	Accuracy	Advantages	Disadvantages
Ultrasonic	TOA/TDOA	0.5 m	No NLOS / no electromagnetic interference	Limited coverage / poor anti-interference
RFID	RSS/PDOA	1.7 m	Indoor coverage / low power / low cost	Low precision / one label per position
UWB	TOA/ TDOA/ AOA	0.1 m	Indoor coverage / high accuracy	High cost / LOS limitation / limited coverage
Wi-Fi	RSS–fingerprinting	2–5 m	Indoor coverage / low cost	Database needed / low accuracy
ZigBee	RSS/PDOA	1–5 m	Indoor coverage / low power/low cost	Low accuracy
Inertial	Acceleration/angular velocity/geomagnetic field	1 m	Adaptable / autonomous	Position drift / indoor magnetic interference
Visual	Image recognition	0.2 m	Relatively low cost / high accuracy	LOS limitation / limited coverage
VLC	Photoelectric modulation and identification	0.5 m	Strong applicability / low power / low cost	Low accuracy

# Navigation and positioning technology in underground coal mines and tunnels: A review

the carrier position, attitude, speed, and other information in real time. This technology is not affected by climatic conditions or external interference factors and can offer high short-term accuracy. However, it is susceptible to serious long-term error accumulation problems.

## Positioning technology using VLC

VLC is a new technology with the characteristics of high bandwidth, high frequency, and low electromagnetic radiation. The distance calculation methods include signal arrival angle, signal arrival time, signal image characteristics, light intensity, and light source ID. Transmitted information is compiled into a photoelectric signal and attached to the driving current of the light source by means of pulse width modulation. VLC, a potential downhole positioning technology, improves the positioning accuracy to the 1 m scale while enhancing the lighting effect in a coal mine.

However, the accuracy of the positioning technology described is seriously reduced in an uncontrolled indoor environment due to problems of signal attenuation caused by wireless signal reflection, non-line-of-sight (NLOS), and multi-path propagation effects (Zhou, Kavehrad, and Deng, 2012). Other signal sensors such as inertial measurement units (IMUs), cameras, and rangefinders can be incorporated to compensate for these problems. This improves the accuracy and robustness of the positioning system by fusing information from different positioning systems.

## Integrated positioning and navigation strategies

Increasing the number of locating nodes and readers is helpful in improving the positioning accuracy, although the deployment, management, and maintenance costs of such a system are high, and more than 75% of the installation time is spent on cables (Lynch and Loh, 2006). A combination of different location technologies can be used to address the limitations of single sensor positioning technology in practical applications (Retscher and Thienelt, 2004; Retscher and Kealy, 2006). Therefore, scholars are constantly working on integrated navigation and positioning strategies based on wireless sensor networks (WSNs). Recently, integrated positioning and navigation strategies have been proposed for the positioning and navigation of underground mining equipment and personnel (Retscher and Thienelt al, 2004). The characteristics of integrated strategies are shown in Table II.

## Positioning strategies based on WSN

Fink and Beikirch (2012) incorporated link quantity information (LQnI) into weighted centroid localization technology with redundant sensor information based on distance estimation to improve indoor positioning. Redundant distance estimation based on the reciprocal sum of squares (RSS) combined with the LQnI method needs more infrastructure or processing power and can then easily improve the accuracy of location estimation. As shown in Figure 3, Song *et al.* (2014) proposed a kind of multiple sensor fusion positioning strategy for tunnel vehicles based on RFID and onboard sensors. RFID is used to estimate the initial position of vehicles in tunnels. Least mean squares (LMS), a federated Kalman filter, is adopted to provide initial position information to the global convergence algorithm. The global convergence algorithm based on the interactive multiple model fuses the preliminary position estimation results and low-cost automotive sensor data such as electronic compass and wheel speed sensor readings. The strong tracking extended Kalman filter algorithm is adopted to replace the traditional extended Kalman filter (EKF) algorithm and is used to ensure the robustness of the actual system parameters in the whole vehicle operation (Song *et al.*, 2014).

The precision and accuracy of UWB from both a theoretical and a practical perspective using real data was assessed by MacGougan, O'Keefe, and Klukas (2009).

Wang and Li (2017) combined UWB and IMU data to achieve indoor positioning through particle filtering in an NLOS environment (Figure 4). The velocity and direction are obtained through integrating the acceleration and angular velocity based on the zero velocity update algorithm. The positioning strategy is executed by treating the IMU signal as the prior information of the particle filter and taking UWB observations as the basis for updating the weight. Experimental results show that the prior information provided by the IMU can suppress the observation error of UWB under an NLOS condition and that the positioning accuracy can be improved from the 1.6 m of a single UWB system to about 0.7 m. The IEEE 802.15.4a impulse radio UWB system achieves a ranging performance of under 30 cm (Oh, Park, and Kim, 2009).

## Strategies based on visual image features

The concept of arranging RFID tag arrays in a known location is used to provide initial position information for the

Table II

Comparison of integrated navigation strategies in recent years

Strategy	Year	Measurement method	Positioning accuracy (m)
RFID/INS	2009	EKF	1.700
RFID/Visual SLAM	2010	MLE	0.755
RFID/ speed odometer	2014	LMS+IMM+STEKF	1.440
WSN/SIINS	2014	Integrated navigation filter	0.200
INS/UWB	2014	FAKF	0.270
VLC/ visual	2015	Background difference method + LMS	0.274
Laser radar/ visual SLAM	2016	TMLE	0.050
UWB/IMU	2017	ZUPT+ PF	0.700
Ultrasonic / visual	2017	Geometric distance location algorithm	0.381
Laser radar/INS	2017	/	0.260
VLC/INS	2017	EKF	0.140
VLC/ visual SLAM	2018	Multi-sensor fusion technology	0.100
WiFi/SINS	2018	Reduced kalman filter	0.500
Camera/INS/speedometer	2018	Federated filter	0.480

# Navigation and positioning technology in underground coal mines and tunnels: A review

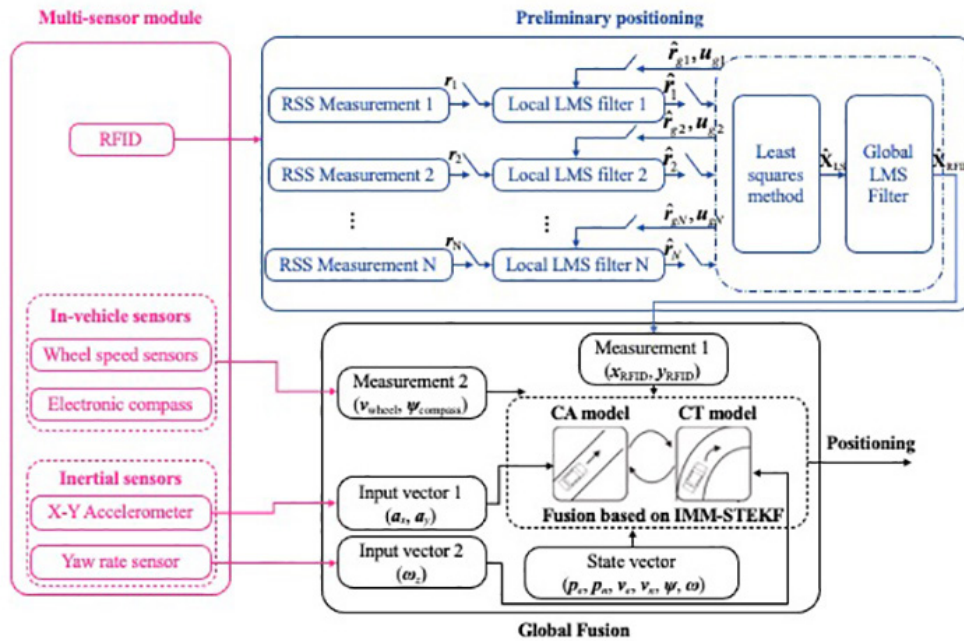


Figure 3—The proposed multi-sensor fusion strategy by Song *et al.* (2014)

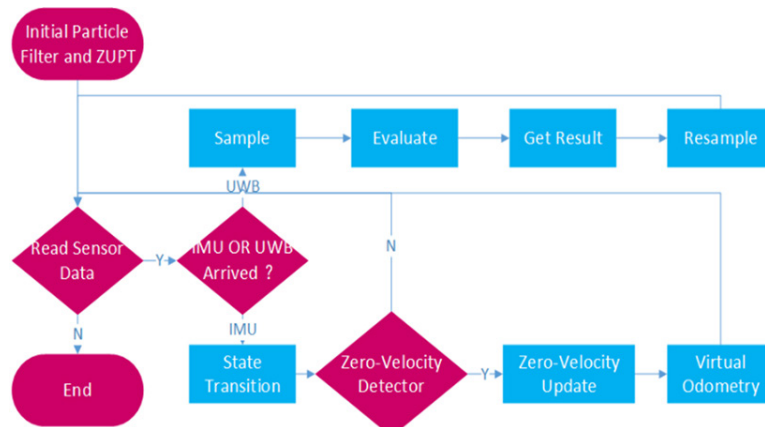


Figure 4—Integrated strategy combined UWB and IMU data according to Wang and Li (2017)

simultaneous localization and mapping (SLAM) algorithm. Errington, Daku, and Prugger (2010) presented a model for tag reception likelihood based on Fourier tesseral harmonics and a least-squares-based position estimator and evaluated it in underground and indoor experiments. A lowest average error of 20.49 cm was achieved in the underground experiment, and 75.53 cm in the indoor experiment.

Kaiming, Wei, and Ruisong (2015) proposed a video-based collaborative positioning strategy (Figure 5) using miners' lamps for positioning miners under conditions of roadway turnout structures and poor illumination. To accurately detect the mining lamp image, the difference between the underground tunnel background image and the acquired video sequence image was obtained using a background difference method. Lines were established between the camera position point and the corresponding projection mapping point of the miner's lamp on the camera imaging plane. The least squares method was used to locate the miners by finding the optimal intersection of the lines. The plane error of the proposed strategy reached 0.274 m in a positioning test (Kaiming, Wei, and Ruisong, 2015).

Chen *et al.* (2016) applied the onboard lidar SLAM technology to a coal mining environment. They successfully generated 2D

and 3D tunnel models using laser scanning matching technology and developed an improved, probabilistically motivated maximum likelihood estimation algorithm with an accuracy limited to approximately 5 cm under practical conditions. Indirect observation shows that the positioning accuracy of this method is at least one level higher than that of traditional methods.

Kai and Xianmin (2017) used a control strategy combining ultrasonic ranging technology and binocular machine vision image processing methods to improve the obstacle avoidance accuracy of a robot underground. Ultrasonic ranging technology and image processing methods are used to detect and observe remote obstacles, and the shape of the closed ranging, respectively. The binocular vision obstacle identification system based on a neural network and the obstacle avoidance strategy combining machine vision with image processing gave good experimental results for the inspection and avoidance of obstacles by the underground inspection robot.

Xu *et al.* (2017) presented an autonomous positioning strategy for local region vehicles in coal mine tunnels based on visual and ultrasonic sensors (Figure 6). Unique barcode labels designed on the UPC-A code were arranged in pairs at intervals on the wall on each side of the tunnel and were recognized by

# Navigation and positioning technology in underground coal mines and tunnels: A review

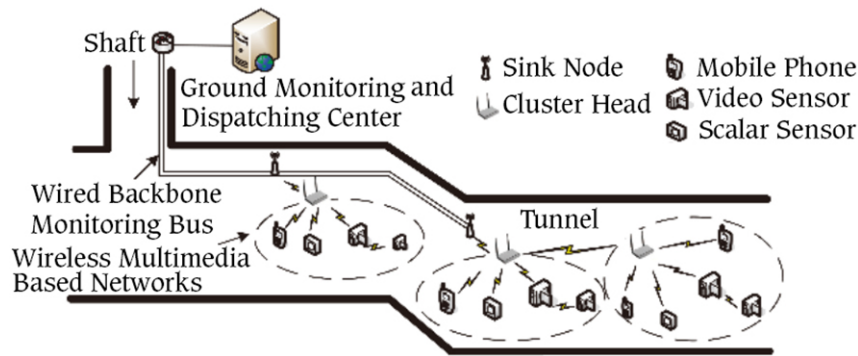


Figure 5—The strategy combining ultrasonic and binocular machine vision technology exploited by Kaiming, Wei, and Ruisong (2015)

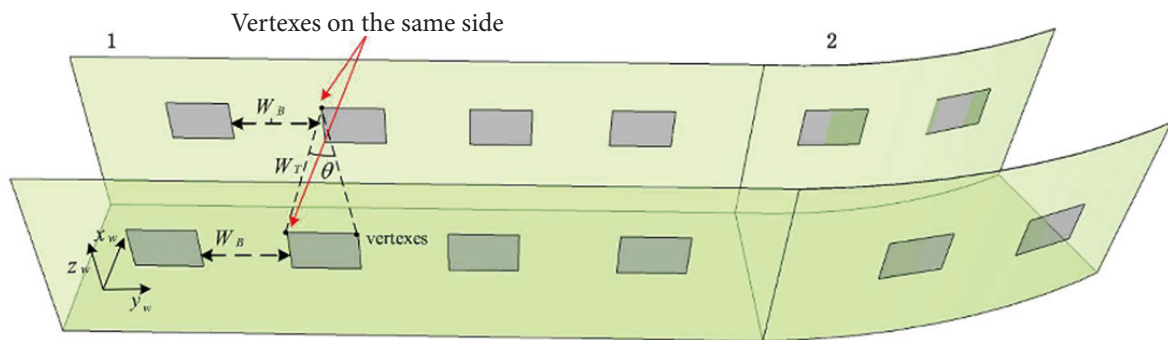


Figure 6—Local positioning strategy composed of visual sensor and ultrasonic sensor (Xu et al., 2017)

two onboard visual sensors. An ultrasonic sensor was used to detect the distance between the vehicle centre and the left side of the tunnel wall. The distance between each barcode label feature frame and the vehicle centre point was determined using a visual distance projection model. Once the spatial geometric relationship between the barcode labels and the vehicle centre point was established, the 3D coordinates of the vehicle centre point in the tunnel global coordinate system were obtained. The average plane positioning error of the vehicle centre point was proved to be under 0.381 m in a localization test of autonomous vehicles in a coal mine tunnel.

### Strategies based on inertial devices

Zhang et al. (2009) combined an EKF with a 3D RFID positioning method and inertial navigation system (INS) to achieve accurate and continuous positioning and provide a 1.7 m accuracy for indoor positioning. Fan et al. (2014) presented a new dynamic location strategy (Figure 7) based on the coupling of a strapdown INS (SINS) and a WSN. A WSN positioning strategy is adopted to eliminate the accumulated error of SINS, after which the coupling model is established. Tracking performance on the attitude and position of a coal mining shearer was verified virtually and experimentally in real time with a positioning accuracy of 0.2 m.

Implementation of a positioning system based on WiFi technology and SINS is highly complex and difficult to engineer. Luo (2016) therefore proposed a new reduced-order ten-state-variables integrated positioning system (Figure 8) and a reduced Kalman filter positioning algorithm by combining a micro IMU and WiFi. Belyaev (2017) proposed a method for underground measurement tasks using a mobile scanning system with inertial navigation. Position information for underground equipment relative to the environment determined by the mobile scanning system is a supplementary to motion parameters obtained by

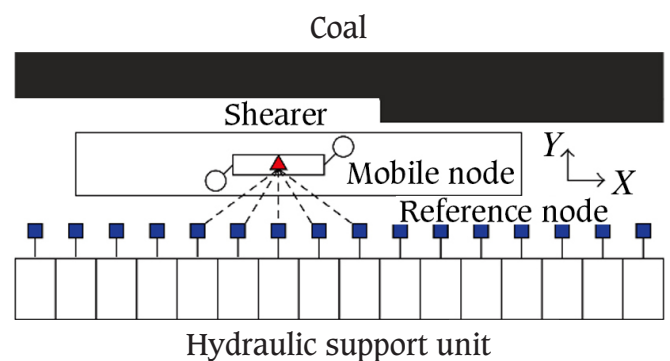


Figure 7—The dynamic strategy based on SINS and WSN proposed Fan et al. (2014)

the inertial system. The experimental results showed that the maximum root mean square of the position error is within 0.26 m per 515 m. A high positioning accuracy with 0.5 m positioning error can be achieved based on the reduced-order integrated positioning system. Wan et al. (2018) proposed an integrated navigation method composed of a stereo camera, IMU, and odometer based on federal filtering. The method, shown in Figure 9, improves the positioning robustness of the system by forming two sub-filters of the IMU-odometer and camera-odometer, respectively. It was experimentally proved that the proposed method effectively improved the navigation and positioning accuracy of the moving platform to 0.48 m and achieved continuous positioning even if there were a failure of the stereo vision positioning system.

The multi modal mapping unit described by Mascarich et al (2018) tightly synchronizes visible light cameras with inertial sensors. Dense mapping of a GPS-denied, dark and visually degraded environment was achieved.

# Navigation and positioning technology in underground coal mines and tunnels: A review

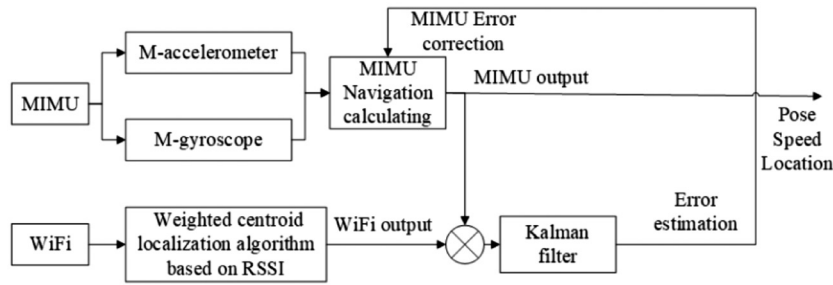


Figure 8—A reduced-order integrated positioning system composed of WiFi and SINS by Luo (2016)

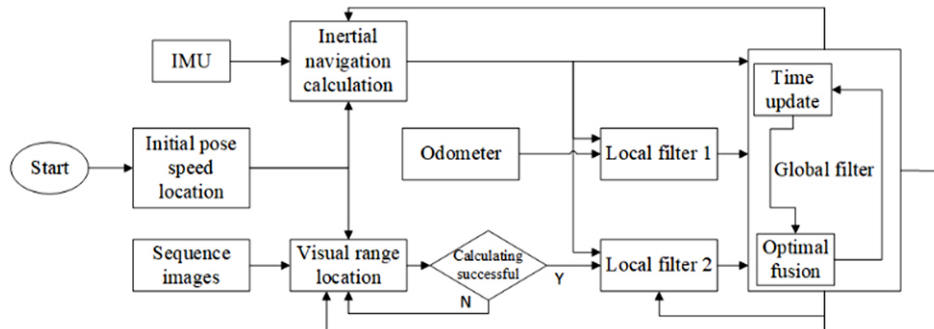


Figure 9—The integrated navigation method composed of stereo camera, IMU, and odometer presented by Wan *et al.* (2018)

## Strategies based on VLC

A fusion positioning system of VLC positioning and inertial navigation has been proposed (Li, Feng, and Yang, 2017; Li *et al.*, 2017) based on an EKF to reduce the error caused by the multipath effect (Figure 10). The maximum positioning error of the system is 0.41 m and the average error is 0.14 m. A comparative analysis proved that the positioning accuracy of the fusion system is twice that of a VLC-based positioning system, and four times that of an INS.

To reduce the high cost and prevent wall blocking in indoor positioning, a low-cost, high-efficiency, and high-precision indoor positioning system has been proposed by Wen *et al.* (2018). High-precision indoor positioning is achieved by adopting indoor LED lights as the positioning base station and using visual RGB depth (RGB-D) SLAM technology for 2D or 3D indoor mapping.

## Research progress in positioning algorithms

According to the information needed in the process of positioning, sensor node localization algorithms commonly used in positioning systems can be divided into two broad categories: those based on distance and those that are not (Wang *et al.*, 2011). Currently, signal processing and localization algorithms are required to be constantly updated for several of the proposed integrated navigation positioning systems to satisfy the reliability and robustness requirements of high-accuracy positioning systems. New methods of signal processing and filtering technology have appeared in recent years. System layouts and position estimation are described below.

## Signal processing and filtering technology

Motion state constraints of multi-sensor navigation systems need to be considered to improve the positioning accuracy and reliability. Yang, Gao, and Zhang (2010) applied state constraints to the standard and robust Kalman filters to produce a robust Kalman filter with state constraints existing among the states

of the multi-sensors in integrated navigation systems. It has been theoretically proved that the covariance matrix of the state vector estimated from the Kalman filter with constraints is indeed smaller than that from the unconstrained filters (Yang, Gao, and Zhang, 2010). To solve the problem that the filtering accuracy decreases rapidly and even diverges using the traditional linear Kalman filter strategy, Fan *et al.* (2014) proposed a fuzzy adaptive Kalman filter (FAKF) by ignoring the accurate measurement of noise prior data. INS/UWB systems using a FAKF filtering algorithm have better stability and real-time performance than traditional Kalman filters with the dynamic positioning error limited to 0.27 m (Fan, *et al.*, 2014).

Aiming at the characteristics of nonlinear and non-Gaussian noise during indoor movement of people and equipment, Ruotsalainen *et al.* (2018) added the correct error probability density function, found through a maximum likelihood method, to the particle filter to build the bootstrap filter. The horizontal localization performance was significantly improved based on the measurement error statistical models of inertial and vision sensors.

Studies have shown (Dorais, Gawdiak, and Clancy, 2002; Heidari and Pahlavan, 2008) that ranging and positioning errors of time of arrival (TOA) were mainly affected by multi-path

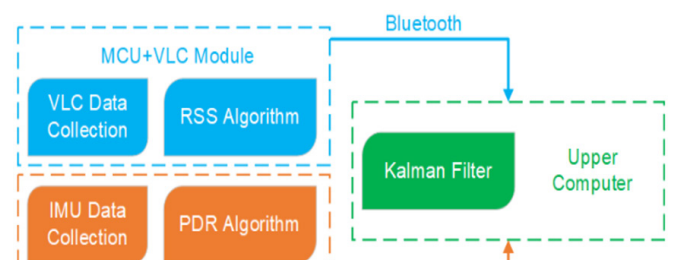


Figure 10—The fusion positioning system of VLC and IMU put forward by Li *et al.* (2017)

# Navigation and positioning technology in underground coal mines and tunnels: A review

phenomena and propagation characteristics in NLOS scenes, and large-scale errors were common when a direct path pulse could not be detected. Aiming at the mismatch between Gaussian white noise and coloured noise, a channel classification-Kalman filter (CC-KF), a new distance mitigation algorithm, combining real channel classification and Kalman filtering, has been proposed to improve the distance mitigation performance under the indoor extreme environment of NLOS and the multi-path effect. The performance of CC-KF and four traditional TOA distance mitigation algorithms was compared in six typical indoor and underground environments. The minimum average absolute distance measurement error of the CC-KF algorithm has a minimum absolute ranging error of 1.01 m, which is obviously better than other algorithms (He *et al.*, 2014). Bhatt *et al.* (2012) demonstrated that the knowledge-based source difference artificial neural network improves the navigation performance of low-cost sensors by 81% compared to the multi-layer perception, with or without external aiding sources.

## System arrangement and location estimation

Problems caused by the low precision and instability of node layout models in WSN positioning are solved through a new beacon nodes arrangement method for underground coal mines proposed by Wang *et al.* (2015). Compared with traditional positioning methods, the method (Figure 11) needs fewer node resources on the premise of satisfying the positioning requirements. The time difference of arrival/angle of arrival hybrid algorithm is a 3D precise positioning algorithm used in coal mines. It is formed by the arrival time information and arrival angle information between the base station and the unknown node, and is used to achieve node positioning. Simulation results show that, based on the new node arrangement model, the algorithm has good positioning accuracy and stability and meets the positioning requirements in a coal mine.

Yi, Tao, and Jun (2017) treated the reciprocal of the sum of the target nodes RSS values received by each anchor node participating in positioning as the weight factor, and proposed a weighted trilateration method based on the traditional trilateration algorithm. By adopting the Grubbs deviation test to reduce the influence of the Kalman filter on the peak value of the pulse deviation, a hybrid filtering algorithm was designed. It is surmised that the improved positioning method together with the hybrid filtering algorithm has a high positioning accuracy of 0.95 m (Yi, Tao, and Jun, 2017).

To achieve unmanned position and pose detection of a boom-type roadheader in a coal mine, Fu *et al.* (2017) designed a UWB pose detection system composed of four UWB positioning base stations and three roadheader positioning nodes, and proposed a fusion positioning algorithm based on the Caffery transform and Taylor series expansion (CTFPA). Three attitude angles (heading angle, pitching angle, and rolling angle) of the machine body are solved based on the system TOA location model (shown in Figure 12) using 12 groups of distance measurement information between every base station and the nodes. The ranging accuracy experiment of the UWB P440 module was conducted in a narrow and closed tunnel. The experimental data showed that the mean error and standard deviation of this module can reach 2 cm (Fu *et al.*, 2017). Combined with the shearer cutting process as a non-holonomic constraint, an optimal error compensation model of system positioning closed path was established by Zhang

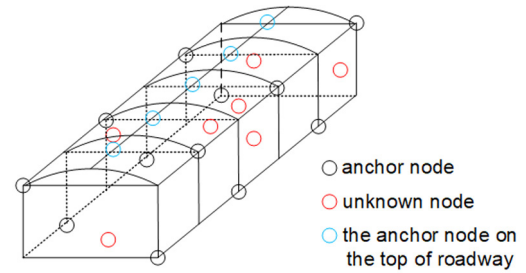


Figure 11 – The new anchor node layout model raise by Wang *et al.* (2015)

(2017) based on the nondeterministic study on the position and pose drift of the inertial positioning navigation system for a coal shearer. The optimal error compensation model of the system-positioning closed path was established to improve the positioning accuracy of the inertial navigation system by nearly 50% (Zhang, 2017).

## Summary and future studies

The progress made through the latest research on underground positioning and navigation technologies has been introduced and recently proposed integrated navigation strategies and positioning methods summarized. The propagation of underground signals suffers serious attenuation, reflection interference, and environmental sensitivity due to the NLOS phenomenon, the multipath effect, and wall interference. Current single navigation and positioning technologies are unable to meet the requirements in coal mine positioning. Underground positioning technology based on multi-sensor fusion and independent navigation systems without external node information are extremely promising to improve the accuracy and robustness of underground navigation and positioning systems. In addition, research into navigation and positioning algorithms may focus on calibration methods for position error estimation and refinement filtering processing of nonlinear signals to improve the stability and timeliness of the integrated navigation strategy.

## Acknowledgements

This work is supported by the National Natural Science Foundation of China (No. 51975570), the Xuzhou Science and Technology Achievements Transformation Plan (KC20203), the Top-notch Academic Programs Project of Jiangsu Higher Education Institutions (TAPP) and Project Funded by the Priority Academic Program Development of Jiangsu Higher Education Institutions (PAPD).

## Disclosure statement

No potential conflict of interest was reported by the authors.

## References

- BELYAEV, E.N. 2017. Extended investigation into continuous laser scanning of underground mine workings by means of Landis inertial navigation system. *IOP Conference Series: Earth and Environmental Science*, vol. 87, no. 5. 052002.
- BHATT, D., AGGARWAL, P., DEVABHAKTUNI, V., and PRABIR, B. 2012. A new source difference artificial neural network for enhanced positioning accuracy. *Measurement Science and Technology*, vol. 23, no. 10. pp. 105101–105111.
- CHEN, Y., TANG, J., HYYPPÄ, J., WEN, Z., LI, C., and ZHU, T. 2016. Mobile laser scanning based 3D technology for mineral environment modeling and positioning. *Proceedings of the Fourth International Conference on Ubiquitous Positioning, Indoor Navigation and Location Based Services (UPINLBS)*, Shanghai, 2–4 November 2016. IEEE, Piscataway, NJ. pp. 289–294.

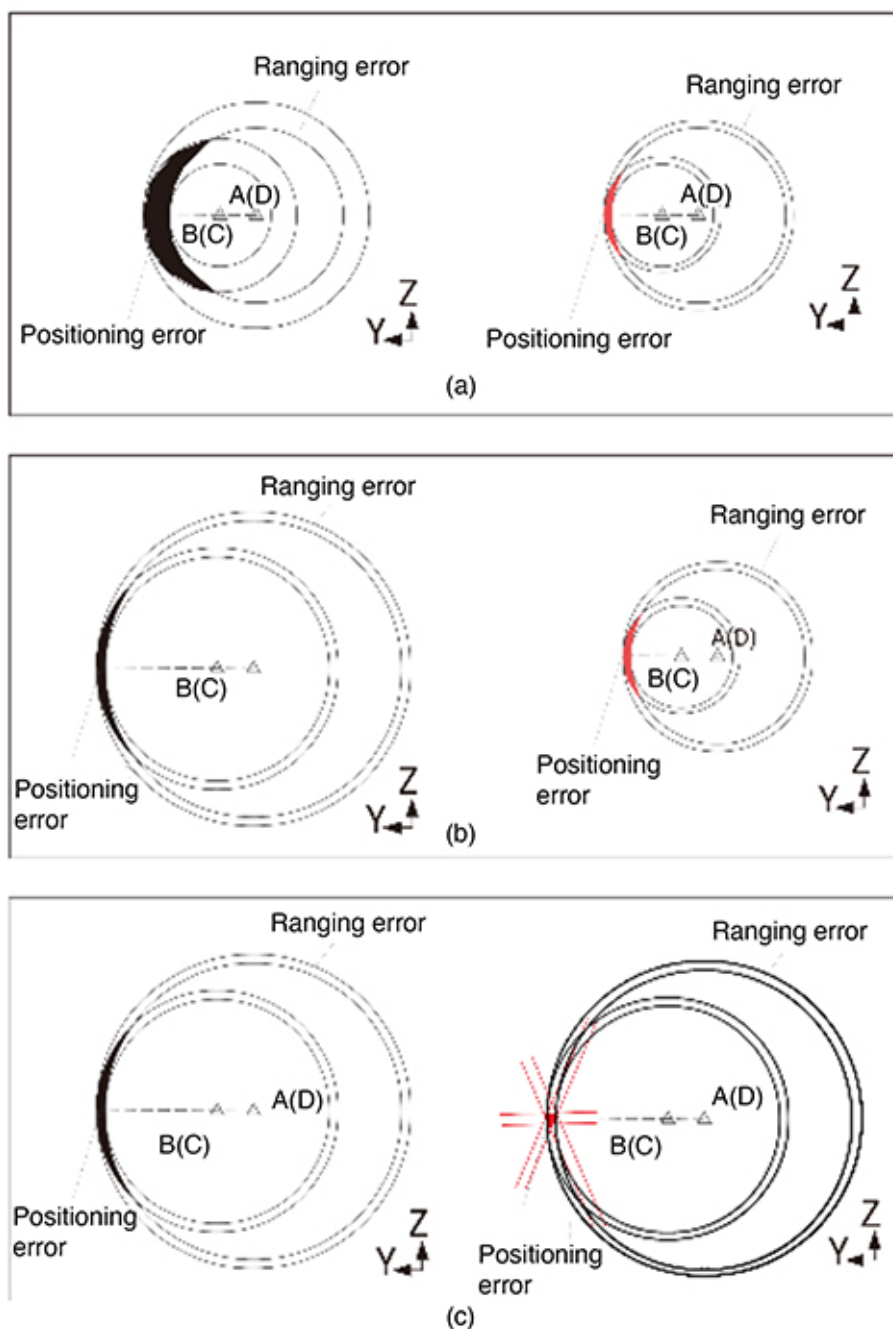


Figure 12—Positioning error analysis of the fusion positioning algorithm (CTFPA) proposed by Fu *et al.* (2017)

DORAIS, G.A., GAWDIAK, Y., and CLANCY, D. 2002. The challenge of planning and execution for spacecraft mobile robots, *NTRS Technical Report*, 2002. <https://ntrs.nasa.gov/search.jsp?R=20020052409>

ERRINGTON, A.F.C., DAKU, B.L.F., and PRUGGER, A. 2010. Initial position estimation using RFID tags: A least-squares approach. *IEEE Transactions on Instrumentation and Measurement*, vol. 59, no. 11. pp. 2863–2869.

FAN, Q., YAHENG, W., JING, H., WU, L., YU, Z., and ZHOU, L. 2014. Integrated navigation fusion strategy of INS/UWB for indoor carrier attitude angle and position synchronous tracking. *The Scientific World Journal*, vol. 2014. pp. 1–13.

FAN, Q., LI, W., HUI, J., WU, L., YU, Z., YAN, W., and ZHOU, L. 2014. Integrated positioning for coal mining machinery in enclosed underground mine based on SINS/WSN. *The Scientific World Journal*, vol. 2014. doi: 10.1155/2014/460415

FINK, A. and BEIKIRCH, H. 2012. Adding link quantity information to redundant RF signal strength estimates for improved indoor positioning. *Proceedings of the International Conference on Indoor Positioning and Indoor Navigation (IPIN)*, Sydney, Australia. IEEE, Piscataway, NJ. pp. 1–6.

FU, S., LI, Y., ZHANG, M., ZONG, K., CHENG, L., and WU, M. 2017. Ultra-wideband pose detection system for boom-type roadheader based on Caffery transform and Taylor series expansion. *Measurement Science and Technology*, vol. 29, no. 1. <https://iopscience.iop.org/article/10.1088/1361-6501/aa91c0/pdf>.

GE, S.R., WANG, Z.B., and WANG, S.B. 2016. Study on key technology of internet plus intelligent coal shearer. *Coal Science & Technology*, vol. 44, no. 7. pp. 15–21.

HE, J., GENG, Y., LIU, F., and XU, C. 2-14. CC-KF: enhanced TOA performance in multipath and NLOS indoor extreme environment. *IEEE Sensors Journal*, vol. 14, no. 11. pp. 3766–3774.

HEIDARI, M. and PAHLAVAN, K. 2008. Identification of the absence of direct path in TOA-based indoor localization systems. *International Journal of Wireless Information Networks*, vol. 15, no. 3-4. pp. 117–127.

KAI, H. and XIANMIN, M. 2017. Research on avoidance obstacle strategy of coal underground inspection robot based on binocular vision. *Proceedings of the 29th Chinese Control and Decision Conference (CCDC)*, Chongqing. IEEE, Piscataway, NJ. pp. 6732–6737.

# Navigation and positioning technology in underground coal mines and tunnels: A review

- KAIMING, Y., WEI, Y., and RUISONG, H. 2015. The video collaborative localization of a miner's lamp based on wireless multimedia sensor networks for underground coal mines. *Sensors*, vol. 15, no. 10. pp. 25103–25122.
- LI, Z., FENG L., and YANG A. 2017. Fusion based on visible light positioning and inertial navigation using extended Kalman filters. *Sensors*, vol. 17, no. 5. doi: 10.3390/s17051093 .
- LI, Z. YANG, A., LV, H., FENG, L., and SONG, W. 2017. Fusion of visible light indoor positioning and inertial navigation based on particle filter. *IEEE Photonics Journal*, vol. 9, no. 5. pp. 1–13.
- LIU, G. and SHI, L. 2018. An overview about development of indoor navigation and positioning technology. *Journal of Navigation and Positioning*, vol. 6, no. 2. pp. 7–14.
- LUO, Y. and YANG, Y. 2016. Mine personnel position algorithm based on reduced-order integrated positioning system. *Electronic Measurement Technology*, vol. 36, no. 5. pp. 93–96.
- LYNCH, J.P. and LOH, K.J. 2006. A summary review of wireless sensors and sensor networks for structural health monitoring. *Shock and Vibration Digest*, vol. 38, no. 2. pp. 91–130.
- MACGOGAN, G., O'KEEFE, K., and KLUKAS, R. 2009. Ultra-wideband ranging precision and accuracy. *Measurement Science and Technology*, vol. 20, no. 9. pp. 1–13.
- MASCARICH, F., KHATTAK, S., PAPACHRISTOS, C., and ALEXIS, K. 2018. A multi-modal mapping unit for autonomous exploration and mapping of underground tunnels. *Proceedings of the IEEE Aerospace Conference*, Big Sky, MT. IEEE, Piscataway, NJ. pp. 1–7.
- OH, M., PARK, J., and KIM, J. 2009. IR-UWB packet-based precise ranging system for u-Home networks. *IEEE Transactions on Consumer Electronics*, vol. 55, no. 1. pp. 119–125.
- RETSCHER, G. and KEALY, A. 2006. Ubiquitous positioning technologies for modern intelligent navigation systems. *Journal of Navigation*, vol. 59, no. 1. pp. 91–103.
- RETSCHER, G. and THIENELT, M. 2004. NAVIO – A navigation and guidance service for pedestrians. *Positioning*, vol. 3, no. 1–2. pp. 208–217.
- RUOTSALAINEN, L., KIRKKO-JAANKOLA, M., RANTANEN, J., and MÄKELÄ, M. 2018. Error modelling for multi-sensor measurements in infrastructure-free indoor navigation. *Sensors*, vol. 18, no. 2. pp. 590.
- SONG, X., LI, X., TANG, W., ZHANG, W., and LI, B. 2014. A hybrid positioning strategy for vehicles in a tunnel based on RFID and in-vehicle sensors. *Sensors*, vol. 14, no. 12. pp. 23095–23118.
- WAN, W., LI Y., HU, W., ZHAO, Q., SUN, X., ZHANG, Q., DI, K., GUO, H., and WU, L. 2018. Mobile platform localization by integration of stereo cameras, IMU and wheel odometer based on federated filter. *Geomatics and Information Science of Wuhan University*, vol. 43, no. 1. pp. 101–106.
- WANG, F., WANG, C., WANG, Z.J., ZHANG, X., and SHANG, C. 2015. Research on 3D localization algorithm of wireless sensor networks in underground coal mine. *Proceedings of the Sixteenth Workshop on Mobile Big Data*, Hangzhou, China. Association for Computing Machinery, New York. pp. 53–57.
- WANG, G., LIU, H., HU, H., and SHEN, S. 2011. Indoor localization algorithm: A survey. *Journal of Nanjing University of Posts and Telecommunications (Natural Science)*, vol. 31. pp. 16–22.
- WANG, Y. and LI, X. 2017. The IMU/UWB fusion positioning algorithm based on a particle filter. *ISPRS International Journal of Geo-Information*, vol. 6, no. 8. pp. 235.
- WEN, C., YOU, C., PENG, L., WU, T., SONG, B., and LV, B. 2018. Research on indoor visible light positioning system based on SLAM maps. *Proceedings of the International Conference on Image and Video Processing, and Artificial Intelligence*, Shanghai. International Society for Optics and Photonics. doi: 10.1117/12.2512460
- XU, Z., YANG, W., YOU, K., and KIM, Y. 2017. Vehicle autonomous localization in local area of coal mine tunnel based on vision sensors and ultrasonic sensors. *PLoS One*, vol. 12, no. 1. https://doi.org/10.1371/journal.pone.0171012.
- YANG, Y., GAO, W., and ZHANG, X. 2010. Robust Kalman filtering with constraints: A case study for integrated navigation. *Journal of Geodesy*, vol. 84, no. 6. pp. 373–381.
- YASSIN A , NASSER Y , AWAD M , AL-DUBAI, A., LIU, R., YUEN, C., RAULEFS, R., and ABOUTANIOS, E. 2016. Recent advances in indoor localization: A survey on theoretical approaches and applications. *IEEE Communications Surveys & Tutorials*, vol. 19, no. 2. pp. 1327–1346.
- YI, L., TAO, L., and JUN, S. 2017. RSSI localization method for mine underground based on RSSI hybrid filtering algorithm. *Proceedings of the IEEE 9th International Conference on Communication Software and Networks (ICCSN)*. Guangzhou, China. IEEE, Piscataway, NJ pp. 327–332.
- ZHANG, B. 2017. Research on dynamic accurate positioning method of shearer. Master's thesis, School of Mechatronic Engineering, China University of Mining and Technology, Beijing.
- ZHANG, K., ZHU, M., RETSCHER, G., WU, F., and CARTWRIGHT, W. 2009. Three-dimension indoor positioning algorithms using an integrated RFID/INS system in multi-storey buildings. *Location Based Services and TeleCartography II*. Springer, Berlin, Heidelberg. pp. 373–386.
- ZHOU, Z., KAVEHRAD, M., and DENG, P. 2012. Indoor positioning algorithm using light-emitting diode visible light communications. *Optical Engineering*, vol. 51, no. 8. p. 085009. ◆

Abbreviations			
Acronym	Meaning	Acronym	Meaning
TOA	Time of arrival	LOS	Line-of-sight
TDOA	Time difference of arrival	NLOS	Non-line-of-sight
AOA	Angle of arrival	ID	Identity
RSS	Received signal strength	LQnI	Link quantity information
PDOA	Phase difference of arrival	WCL	Weighted centroid localization
RFID	Radio frequency identification	LS	Least square
UWB	Ultra-wideband	LMS	Least mean square
VLC	Visible light communication	IMM	Interactive multiple model
INS	Inertial navigation system	KF	Kalman filter
SINS	Strapdown inertial navigation system	PF	Particle filter
IMU	Inertial measurement unit	EKF	Extended Kalman filter
WSN	Wireless sensor network	STEKF	Strong tracking extended Kalman filter
UPDS	Ultra-wideband pose detection system	FAKF	Fuzzy sdaptive Kalman filter
CC-KF	Channel classification and Kalman filter	ZUPT	Zero velocity update
CTFPA	Caffery transform and Taylor series expansion based fusion Positioning algorithm	SLAM	Simultaneous localization and mapping
TMLE	Targeted maximum likelihood estimation	MSSs	Mobile scanning systems
IMLE	Improved probabilistically-motivated maximum likelihood estimation	RMS	Root mean square

# Tailings Facility Management Research

## Call for expressions of interest

The failure of the Brumaldinho tailings dam in Brazil, and other recent failures, has precipitated global attention on the design and stability of tailings storage facilities (TSFs).

The International Council on Mining and Minerals (ICMM) has produced the Global International Standard on Tailings Management (GISTM), which addresses issues beyond technical design and monitoring, covering socio-economic and environmental topics such as the principles governing affected communities, emergency response, long-term recovery, and disclosure and information sharing.

The SAIMM is participating in the Global Mining Professional Alliance (GMPA) Global Action on Tailings Group, which is promoting and coordinating global research. The results will translate into learning and training, and appropriate competency development and registration of professionals.

This shift in perspective requires research work to be conducted on all of these aspects, as well as in terms of design, monitoring and management.

The ICMM Standard sets out global guidance on these issues, which can be cascaded to local or regional standards and guidelines. In this regard the SAIMM has partnered with the South African Council of Civil Engineers (SAICE) to revise and update the South African Standard on mine residue deposits (SANS 10286), which was last revised in 1998.

This revision will then inform the potential development of a Southern African Code for TSF management.

All of this work has been moved to a higher level as a result of requests for more disclosure from investors and NGOs, and the raising of the issue to Board levels. Although the probability of a TSF failure may appear low, the consequences of an incident could be catastrophic.

The GISTM has broad implications, impacting many issues that have previously not been considered in depth, including highly technical issues concerning design and monitoring. This requires work in the fields of instrumentation, management, geotechnical and civil engineering design, soil mechanics, metallurgy, engineering, and the social sciences. Ultimately, it involves research into the mine of the future, where tailings dams are not constructed.

Tertiary institutions are invited to express their level of support for, and involvement in, research in this area, and to identify potential research topics. In addition, industry is requested to support the research initiatives through the identification of research subject and the provision of resources supporting research in this area, which is of paramount importance to the broader mining industry in Southern Africa.

The research is also of interest to all stakeholder groups, and the aim of the SAIMM is to provide a platform where open dialogue and independent investigations can be conducted.

Expressions of interest can be addressed and written submissions submitted to the SAIMM Secretariat by the end of August.

### FOR FURTHER INFORMATION, CONTACT:

Camielah Jardine,  
Head of Conferencing

E-mail: [camielah@saimm.co.za](mailto:camielah@saimm.co.za)  
Web: [www.saimm.co.za](http://www.saimm.co.za)



**SAIMM**  
THE SOUTHERN AFRICAN INSTITUTE  
OF MINING AND METALLURGY



# Investigation of the mechanism for fire-side corrosion in coal-fired boilers in South Africa

K.G. Moloko<sup>1,2</sup> and J.W. van der Merwe<sup>1</sup>

## Affiliation:

<sup>1</sup> School of Chemical and Metallurgical Engineering, Faculty of Engineering and Built Environment, University of the Witwatersrand, Johannesburg, South Africa.

<sup>2</sup> Eskom, Research & Innovation Centre, Johannesburg, South Africa.

## Correspondence to:

J.W. Van der Merwe

## Email:

josias.vandermerwe@wits.ac.za

## Dates:

Received: 2 Oct. 2019

Revised: 18 Mar. 2021

Accepted: 30 Mar. 2021

Published: June 2021

## How to cite:

Moloko, K.G. and van der Merwe, J.W. 2021

Investigation of the mechanism for fireside corrosion in coal-fired boilers in South Africa.

Journal of the Southern African Institute of Mining and Metallurgy, vol. 121, no. 6, pp. 305–316.

## DOI ID:

<http://dx.doi.org/10.17159/2411-9717/951/2021>

## ORCID

J.W. Van der Merwe

<https://orcid.org/0000-0003-4563-8078>

## Synopsis

Furnace wall tubes from 600 MW subcritical boilers at three coal-fired power stations were sampled and the fireside deposits examined to determine the mechanism of fireside corrosion. This involved an in-depth investigation into the morphology and composition of the fireside deposits and the conditions of the furnace that enable this type of attack. SEM-EDS analysis revealed high concentrations of oxygen, iron, and sulphur, QEMSCAN and XRD analyses identified the presence of Fe<sub>3</sub>O<sub>4</sub>, Fe<sub>2</sub>O<sub>3</sub>, FeS, and FeS<sub>2</sub>. Differential thermal analysis showed thermal activities at temperatures of 500–600°C, 900–1100°C, and 1100–1250°C, which are associated, respectively, with FeS<sub>2</sub> oxidation to FeS and Fe<sub>2</sub>O<sub>3</sub>, at 475–525°C, formation of aluminosilicates at 925–1100°C, and melting of FeS around 1190°C. The absence of sodium and potassium eliminates the contribution of molten alkali sulphates to the corrosion. The consistent coexistence of iron sulphide and iron oxide is indicative of the substoichiometric conditions in the furnace, while the detection of pyrite suggests that the coal is not completely combusted, which points to a poor combustion process. These observations were affirmed by gas analysis at one of the stations, where very high levels of carbon monoxide were measured at the furnace wall ( $\geq 14\,000$  ppm) and furnace exit ( $\geq 3500$  ppm). The high CO concentrations are indicative of limited combustion caused by limited O<sub>2</sub>. These reducing conditions promote the formation of FeS-rich deposit, which is the corrosive species responsible for degradation.

## Keywords

fireside corrosion, sulphidation, coal-fired boiler, furnace wall tubes.

## Introduction

Fireside corrosion is the metal loss from tubes due to chemical attack on the fireside of heat exchanging surfaces in fossil fuel-fired furnaces. It is due to high temperatures and the unique environment encountered in the furnaces, which is caused by the complex interaction of the combustion gases at temperatures varying between 400 and 1200°C (Syed, Simms, and Oakey, 2011), the distribution of pulverized fuel, elements released from the fuel, the type and nature of the ash carried over in the gas stream, and the materials of construction of the boiler.

Fireside corrosion in boilers is commonly divided into two categories by location, namely furnace wall corrosion in the lower furnace and fuel ash corrosion of superheaters in the upper furnace. This type of corrosion was first recognized as a serious problem in the early 1940s, when some of the power stations in the USA using pulverized coal-fired furnaces, experienced an increased number of furnace wall tube failures (Harb and Smith, 1990). In South Africa, the corrosion phenomenon was identified in the early 1990s when a few coal-fired subcritical boilers (600 MW units) suffered damage and tube failures in the furnace area.

Despite efforts to manage the effects of fireside corrosion, through (i) measuring and monitoring of the remaining wall thickness of the tubes by ultrasonic tests during unit outages and (ii) replacing tubing below the minimum wall thickness, the level and extent of damage have been increasing and resulting in high costs and extensive outage times. In addition, future trends such as the installation of low-NO<sub>x</sub> burners to control SO<sub>x</sub> and NO<sub>x</sub> emissions and an increase in the steam temperatures to raise the thermal efficiency, *i.e.* through the construction of supercritical boilers, are likely to increase fireside corrosion within Eskom boilers, as has been seen in other power plants globally (Bakker, 1998; Hatt, 1990). To comply with air pollution control legislation, coal-fired power generation industries have found it necessary to apply technologies that reduce NO<sub>x</sub> and SO<sub>x</sub> emissions. Low excess air combustion and two-stage combustion are commonly applied as means of realizing low-NO<sub>x</sub> combustion (Bakker, 1998; Dooley and MacNaughton, 2007). Although these combustion methods can reduce NO<sub>x</sub> emissions from a boiler, a strong reducing atmosphere is formed in the region between the burners and air ports in the case of two-stage combustion. This atmosphere promotes the formation of hydrogen sulphide (H<sub>2</sub>S),

## Investigation of the mechanism for fireside corrosion in coal-fired boilers in South Africa

which causes sulphidation corrosion at the boiler wall (Bakker, 1998; Dooley and MacNaughton, 2007). In addition, to meet the high demand for electricity, supercritical boilers are increasingly being introduced. At higher temperatures, boiler tubes are at a higher risk of suffering high-temperature corrosion, which includes fireside corrosion.

Owing to the limited knowledge and understanding regarding the actual mechanisms of this phenomenon in Eskom coal-fired boilers, this investigation was initiated with the aim of determining the mechanism of fireside corrosion and the drivers of and contributors to the phenomenon. The investigation was aimed at ascertaining:

- Whether the fireside corrosion attack within the boiler units of the selected power stations is by sulphidation and/or by formation of low-melting alkali sulphate salts
- The influence of the environment in the furnace
- The role of the combustion process in promoting the fireside corrosion mechanism.

### Experimental procedure

Coal composition and the subsequent release of gaseous, molten, or solid components via the combustion process are primary determinants of the potential severity of fireside corrosion (Dooley and MacNaughton, 2007). The most important corrodents are (i) sulphur, present as sulphur dioxide and sulphur trioxide, or as hydrogen sulphide, (ii) vapours of alkali metal salts in the form of oxides, hydroxides, or sulphates, and (iii) chlorine compounds. Knowing the mineralogy of the ash deposit is important in understanding the fireside deposits and their relationship to corrosion. The mechanism of fireside corrosion was investigated by collecting and evaluating samples of fireside deposit and performing *in-situ* gas analysis, which due to limited availability of boiler units was applied only on one unit of one power station.

### Sampling

During plant shut-downs at three power stations (A, B, and C), tubing samples were removed from the areas that are historically known to suffer from fireside corrosion. The samples were selected using the following criteria:

- Tubing that failed during operation
- Tubing with wall thicknesses below the required minimum, as measured by ultrasonic testing.

The sampling areas selected were where fireside corrosion-related failures occurred or tube replacements were required due to low remaining wall thicknesses. A minimum of two units per power station were sampled for representability and repeatability of results. Figure 1 shows the areas sampled at the respective power stations.

In order to ensure that the fireside deposit was preserved during sampling, the in-house procedure for cutting, storage, and transportation of samples was applied (Chabula, 2009). The tubes were cut to a minimum of 1 m length with a saw, at a position 300 mm away from damage in order to prevent contamination by debris and overheating. Subsequent to cutting, tubes were marked clearly to show the boiler unit number, location, level, tube number, and sample orientation. The tubes were restricted from movement during transportation in order to avoid spalling of the fireside deposit. The tubes were also kept away from contact with water or any other liquid during storage and transportation.

### Sample descriptions

Two sidewall tubes were tested and analysed from units 1, 3, and 4 of power station A, units 1, 3, and 8 of power station B, and units 4 and 6 of power station C.

### Condition of the tubes investigated

Specimens were sectioned from the tubes for testing and verification of the material, which was done by means of chemical analysis with spark emission spectroscopy, microstructural examination, and hardness testing with a Leco Macro Vickers hardness tester with an applied load of 10 kg. Verification of calibration was done using a 109 HV10 kg Yamamoto hardness test block. The results obtained were benchmarked against the standard specification BS EN 10216- 2 (2013), which is equivalent to the original code used in the design of the tubes.

### Analysis of deposits

Mechanical (cutting and scraping) and metallographic methods (grinding, polishing, and etching) were employed during the preparation of the fireside deposit specimens. The steps in the preparation of specimens were as follows.

- Ring samples were cut out to prepare for analysis of the cross-sectional area of the tubes. A Struers Labotom-15 abrasive cutter was used.
- Deposit powder was scraped off the tubes using a sharp steel blade.
- Tubing cross-sections were ground with silicon carbide paper with grit size ranging from 220  $\mu\text{m}$  to 2400  $\mu\text{m}$ .
- Ground specimens were subsequently polished with diamond suspension to a surface finish of up to 1  $\mu\text{m}$ .
- After polishing, specimens prepared for microstructural examination were etched with 5% Nital to expose the general microstructure of the material.

The analysis and characterization of the fireside deposits were performed as follows.

- Scanning electron microscopy (SEM) with energy-dispersive X-ray spectroscopy (EDX) to map out the concentration and distribution of elements within each layer of the fireside deposit, using an FEI – QUANTA 600 instrument. The fireside deposits were analysed and mapped along the cross-section of the tube. The data from the analysis was processed and interpreted using INCA Feature version 1.1 software. The chemical compositions of the deposits and corrosion products on the metal surfaces were studied using EDX by elemental mapping line profiles.
- Chemical date was obtained by Quantitative Evaluation of Minerals By Scanning Electron Microscopy (QEMSCAN™), using a QEMSCAN 650F instrument, and X-ray diffraction (XRD). The data was processed with Discover version 5.3 software.
- Differential thermal analysis (DTA) was used to determine the thermal behaviour of the compounds in the fireside deposit. The powder specimens were mounted onto sample holders and analysed by single crystal X-ray diffraction (SC-XRD) with a Bruker D8 Venture Photon CMOS. The data was processed, and interpreted using the Diffrac.Suite EVA version 4.2.2 (Bruker brand) software.

Cross-sections of the tubes with attached fireside deposit were prepared for SEM-EDS and QEMSCAN evaluations as shown in Figure 1. Two tube ring cross-sections were removed from each

# Investigation of the mechanism for fireside corrosion in coal-fired boilers in South Africa

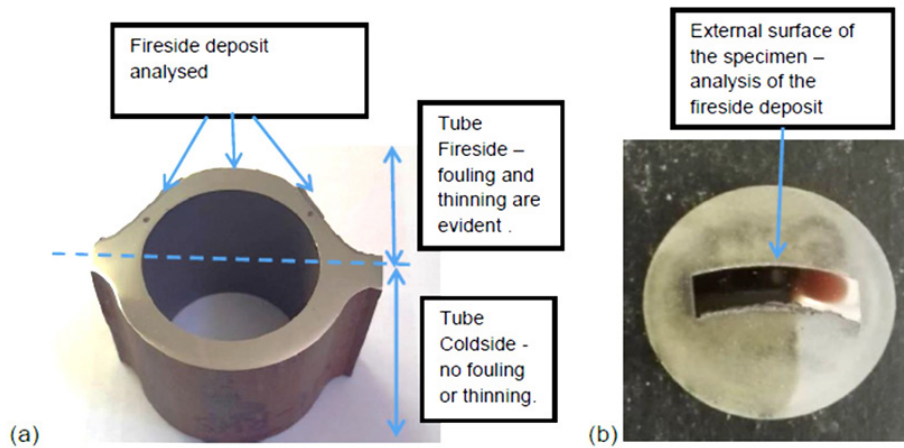


Figure 1—Cross-section of the tube prepared for microstructural examination and SEM analysis (a) at 10 o'clock, 12 o'clock, and 2 o'clock positions, and (b) mounted QEMSCAN specimen

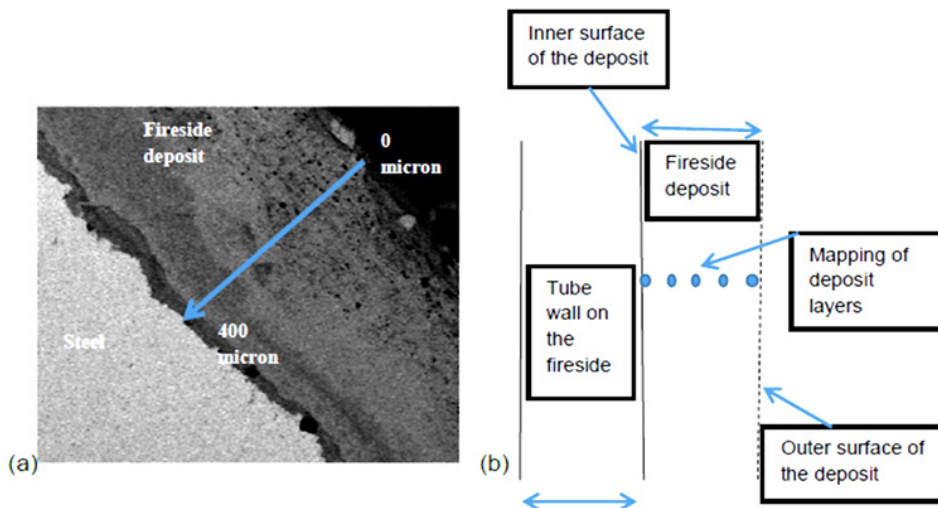


Figure 2— (a) SEM fireside deposit mapping from outer to inner layer, (b) layout of EM and QEMSCAN deposit analysis on the fireside of the steel surface

tube with the deposit still intact. Figure 2 illustrates the way the fireside deposit was analysed and characterized. The cutting was done under dry conditions to avoid contamination from fluids.

Powder samples of at least 3 g (for XRD) and 10 g (for DTA) analyses were obtained by scraping off the fireside deposit. The DTA analysis was performed in alumina crucibles 6 × 2.5 mm in size. A maximum testing temperature of 1400°C was used with a heating rate of 10°C/min in a nitrogen atmosphere.

### In-situ gas analysis

The actual conditions of the flue gas were determined at one boiler, by performing *in-situ* combustion tests, which involved analysis of the composition of the flue gas, measurements of the tube temperature, and analysis of the distribution of air (or excess oxygen) in the furnace. The *in-situ* gas analysis was conducted at unit 1 of Station A over a period of three days at different excess air levels with oxygen (O<sub>2</sub>) at 2.48%, 2.82%, and 3.1% on a dry basis. The in-furnace probing positions were located at gun blower 12 (one of the areas where fireside corrosion has occurred repetitively), the furnace exit, superheater 3, and reheater 2 to cover different levels of the boiler. Temperature traverses were conducted on both the left-hand side (LHS) and right-hand side (RHS) of the economiser inlet and

outlet areas. Oxygen and carbon monoxide measurements were taken at the furnace exit (RHS) and both sides of the economiser outlet ducts. The results of the gas analysis were checked against the fireside deposit analysis at the same station to determine the link between the furnace environment and the type of fireside corrosion taking place.

### Results

#### Tube conditions – visual inspection

The hard and thick sintered deposits with loosely bonded ash on the fireside of the tubes from the three power stations are shown in Figure 3. The deposit thicknesses were a maximum of 0.975 mm, 0.6 mm, and 0.57 mm for stations A, B, and C respectively. Wall thinning was observed on the cross-sections of the tubes, with the fireside generally showing significant thinning and the cold side exhibiting a uniform wall with minimal thinning. Figures 4 and 5 show the localized wall thinning on the fireside of tubes from stations A and C at the location encompassing a 120° angle of the tube circumferentially (referred to as the 10 o'clock and 2 o'clock positions). One of the ruptured tubes from Station A is shown in Figure 3a. This tube failed due to significant wall thinning and excessive build-up of pressure.

## Investigation of the mechanism for fireside corrosion in coal-fired boilers in South Africa

The wall thickness measured on the fireside of Station A tubing varied from 0.1 to 4.93 mm. This implies that the tubes with the original wall thickness of 5.6 mm experienced wall losses ranging from approximately 11.9 to 98.2%. Station C, having tubes, with original wall thickness of 7.5 mm and remaining wall

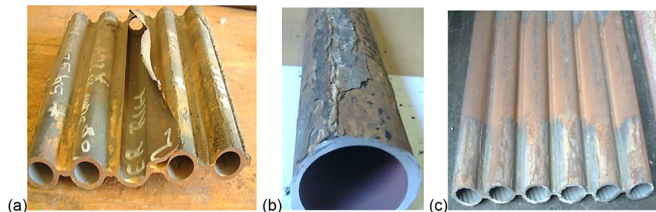


Figure 3—Furnace wall tubes from (a) Station A, (b) Station B, and (c) Station C, showing the fireside deposit. Ruptured tube from Station A is shown in (a)

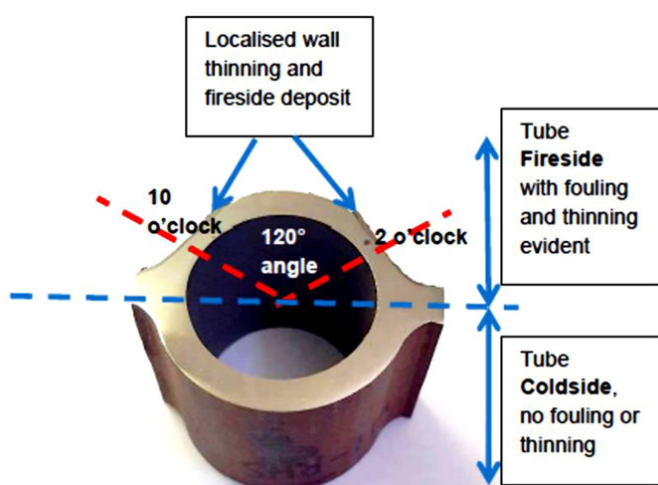


Figure 4—Samples prepared for SEM analysis with fireside deposit located at the 10 o'clock and 2 o'clock positions of the fireside of the tube

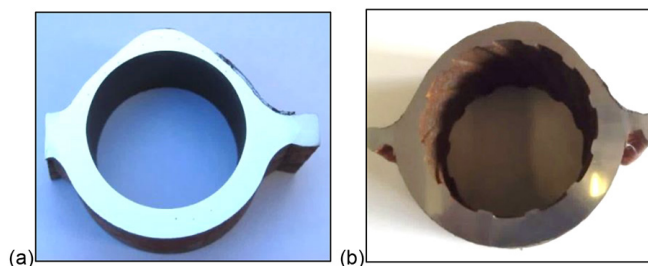


Figure 5—Cross-section specimens of tubing from (a) Station A and (b) Station C showing localized wall thinning on the fireside

thicknesses of 2.92 to 3.4 mm, experienced relatively lower wall loss, estimated at 45.2 to 65.33%.

Tubes from Station B showed different features compared to stations A and C. Unit 1 tubes revealed general wall thinning around the circumference. Unit 8 showed wall thinning only on the fireside. Unit 3, on the other hand, showed a completely different picture; inconsistent wall thinning was observed on both the fireside and non-fireside as shown in Figure 6. Observations on tubing from Station B suggest that in addition to fireside corrosion, there may be other forms of attack taking place. Different fireside deposits were also observed on Station B tubing. Units 1 and 3 had hard and thin sintered brown deposits, whereas unit 8 had loosely bonded grey ash deposits. The wall thickness of the tubing from Station B ranged from 1.76 to 5.54 mm. Based on a 6 mm installed wall thickness, the highest wall thinning was measured at 68.57%.

### Tube conditions – chemical analysis and hardness measurement

Table I shows compliance between the chemical composition of station A and B tubes and the standard specification of 16Mo3 steel as defined in BS EN 10216-2 (2013). Station C matches

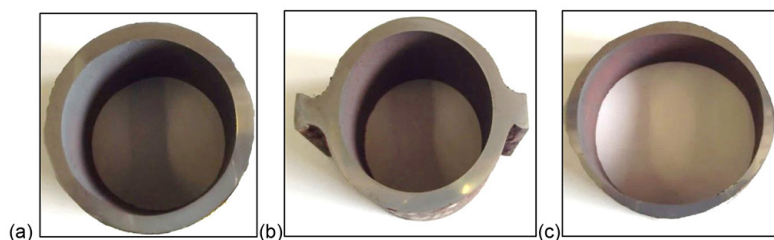


Figure 6—Cross section specimens of Station B tubing showing (a) uniform wall thinning on fire- and cold sides of unit 1, (b) wall thinning on fireside of unit 8, and (c) inconsistent wall thinning around the tube of unit 3

Table I

### Chemical analysis of tubing samples from stations A, B, and C (wt.%)

	Station A	Station B	Station C	BS EN 10216-2 (2013): 16Mo3	ASTMA106 (2018) A106M Grade B	Permissible variation
C	0.16	0.17	0.15	0.12–0.20	0.35 max.	±0.02
Mn	0.56	0.72	1.09	0.40–0.90	0.60–1.05	±0.05 (16Mo3) ±0.10 (A106)
S	0.013	0.005	0.047	≤ 0.01	0.040 max.	+0.005
P	0.018	0.009	0.024	≤ 0.025	0.035 max.	+0.005
Si	0.31	0.24	0.22	≤ 0.35	0.10–0.35.	±0.05
Cr	0.05	0.05	0.12	≤ 0.30	0.30 max.	±0.05
Mo	0.29	0.06	0.03	0.25–0.35	0.12 max.	±0.03
Ni	0.006	0.15	0.12	≤ 0.30	0.40 max.	±0.005
Cu	0.008	0.18	0.25	≤ 0.30	0.40 max.	±0.05

# Investigation of the mechanism for fireside corrosion in coal-fired boilers in South Africa

the standard specification of St 45.8 as defined in ASTM A106/A106M (2018). Table II outlines the average hardness of the tubing on the fire- and cold sides, which are similar and well within the specification for 16Mo3 and St 45.8 when converted from ultimate tensile strength of 450–600 MPa and 415 MPa respectively using a conversion guideline in ASTM A370 (2019). The error margin of  $\pm 1$  HV was measured on the calibration block. The outcome from chemical analysis and hardness tests confirms that the correct material was used, thus the corrosion is mainly due to furnace conditions and less due to the material of the tubes.

### Microstructural examination

The microstructures observed on tubing samples from the three power stations were the same on both fireside and cold side, as shown in Figure 7. They consisted of well-spheroidized and degenerated carbides, still grouped in the original pearlitic pattern, in a ferrite matrix. A spheroidized microstructure is typical of service-exposed 16Mo3 and A106 Grade B tubing operating at moderately elevated temperatures. A similar appearance between the fireside and cold side indicates that the flame-exposed (fire-) side of the tubing was not significantly hotter than the casing (cold) side.

### Deposit analysis

Subsequent to visual inspection and examination under light microscopy, the fireside deposits were analysed with SEM-EDS, SEM-QEMSCAN, XRD, and DTA. The results are presented in the four sections below.

### SEM-EDS analysis of the fireside deposit

A three-layered fireside deposit was consistently seen in all the tubing samples from all three power stations, with similar elemental profiles as shown in Figure 8 to 15. A high concentration of oxygen was seen in the thin inner layer – immediately adjacent to the metal, as well as in the outer layer. Sulphur was mostly concentrated in the middle layer. High iron was detected throughout the thickness of the fireside deposit. The distribution of elements was as follows:

- Inner layer: High concentration of iron and oxygen and no or traces of sulphur.
- Middle layer: Rich in iron and sulphur with low to moderate concentration of oxygen.
- Outer layer: High levels of iron and sulphur with low concentration of oxygen and Al, Si, and Ca (fly ash particles).

Table II

Hardness values for stations A, B, and C measured at HV10

Tube identity	Fireside (HV)	Cold side (HV)	Hardness standard specification
Station A	146 $\pm$ 1	144 $\pm$ 1	BS EN10216-2 for 16Mo3: 131–186 HV
Station B	143 $\pm$ 1	137 $\pm$ 1	
Station C	155 $\pm$ 1	147.6 $\pm$ 1	ASTM A106 Grade B: 123 HV

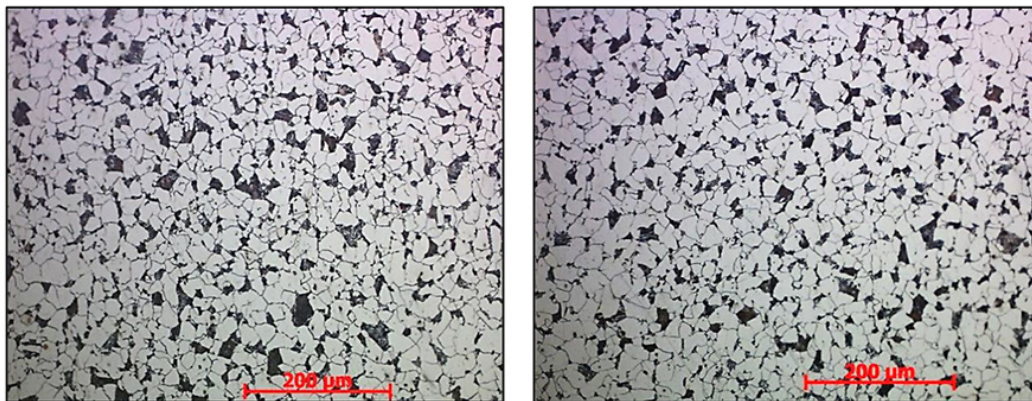


Figure 7—Microstructure of sidewall tubing from Station A on (left) fireside, and (right) cold side

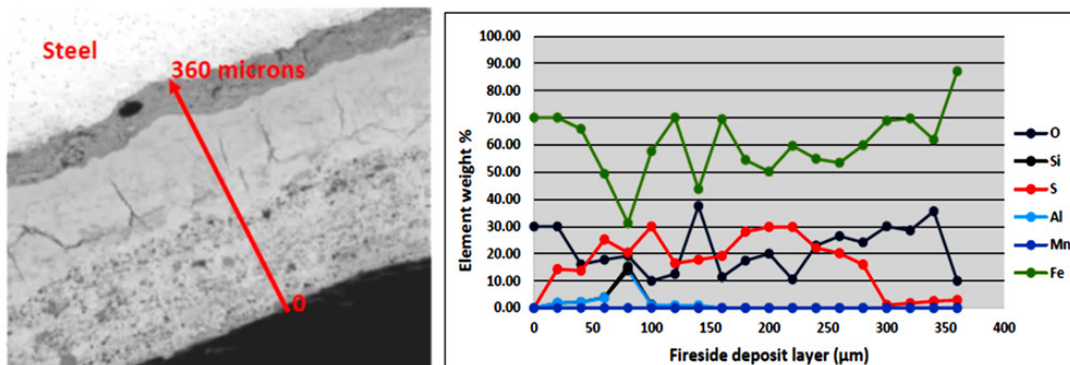


Figure 8—Unit 3 of Station A showing Fe-O rich inner layer, moderate Fe-S and Fe-O middle layer, and Fe-S, Fe-O, and fly ash outer layer

# Investigation of the mechanism for fireside corrosion in coal-fired boilers in South Africa

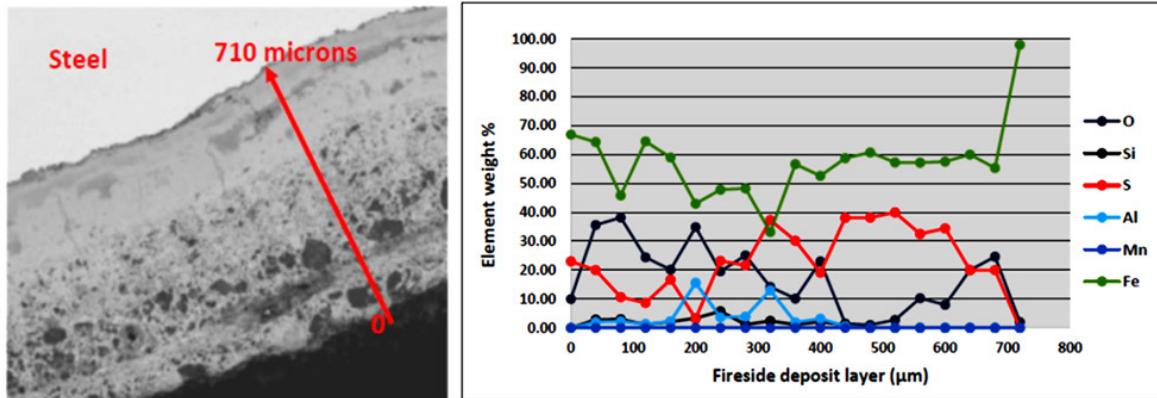


Figure 9—Unit 1 of Station A showing Fe-O rich inner layer, Fe-S middle layer, Fe-S and Fe-O outer layer with particles of fly ash and unburned coal

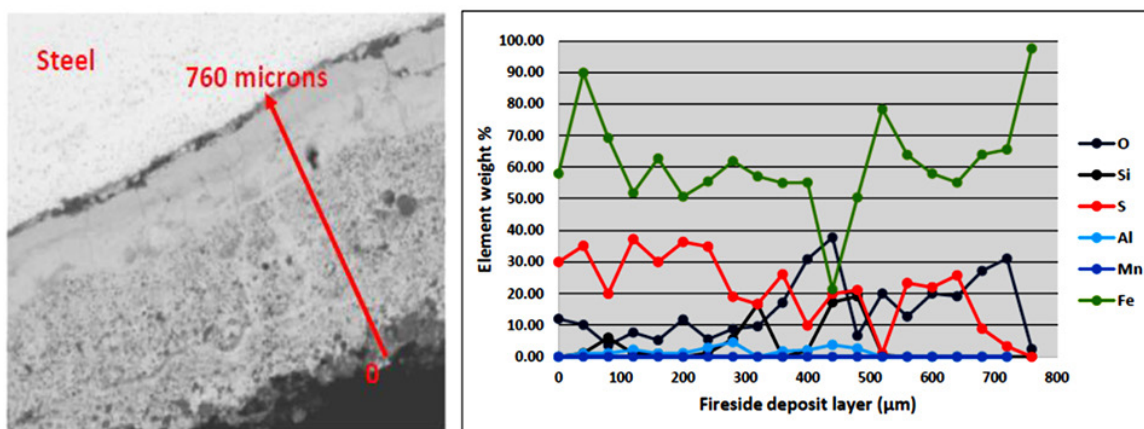


Figure 10—Unit 4 of Station A showing Fe-O rich inner layer, Fe-S rich middle layer, Fe-S/Fe-O outer layer with fly ash particles

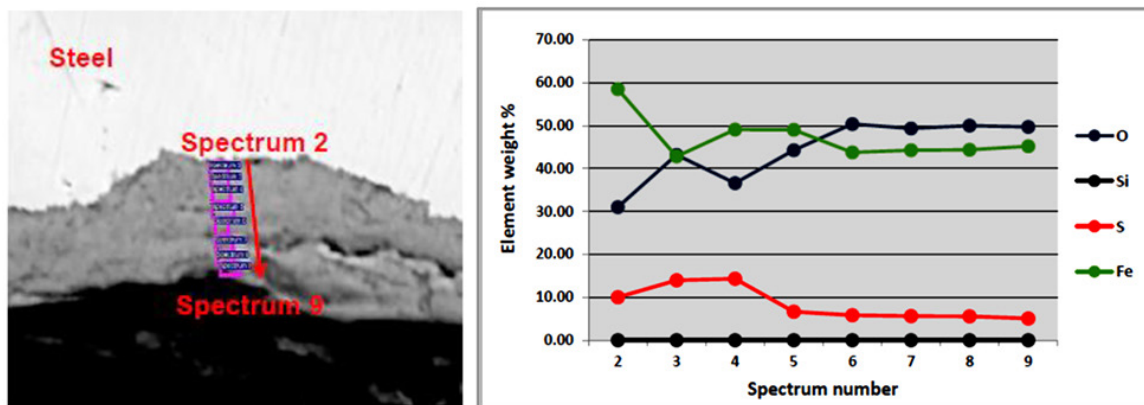


Figure 11—Unit 8 of Station B showing Fe-O rich inner layer with moderate S, and Fe-O rich outer layer with low concentration of S

## QEMSCAN

QEMSCAN analysis was performed on the fireside of the tubes from stations A and C. Due to the lack of samples from Station B during this analysis, the mineralogy of Station B tubes was analysed with XRD only. A similar morphology was observed on the fireside deposits from stations A and C. As shown in Figures 16 and 17 respectively, a three-layered deposit with a consistent band of Fe-sulphide rich phase was observed on the interface to the steel extending to the middle section. The outer layer was predominantly iron oxide with fly ash particles: quartz ( $\text{SiO}_2$ ), kaolinite ( $\text{Al}_2\text{O}_3 \cdot 2\text{SiO}_2 \cdot 2\text{H}_2\text{O}$ ), Ca/Mg aluminosilicate, and pyrite

( $\text{FeS}_2$ ). These results correlate with the high iron and sulphur concentrations in the middle and innermost layers detected by SEM-EDS. Figure 18 and 19 give the mineralogical composition of the fireside deposits from stations A and C respectively. The fireside deposit thickness was measured at a maximum of 1.2 mm for Station A and 0.53 mm for Station C.

There was no evidence of sodium or potassium associated with the sulphur in any of the samples from stations A and C. The presence of sulphide phases coexisting with iron oxide is indicative of substoichiometric conditions in the furnace and/or on the tube surfaces.

# Investigation of the mechanism for fireside corrosion in coal-fired boilers in South Africa

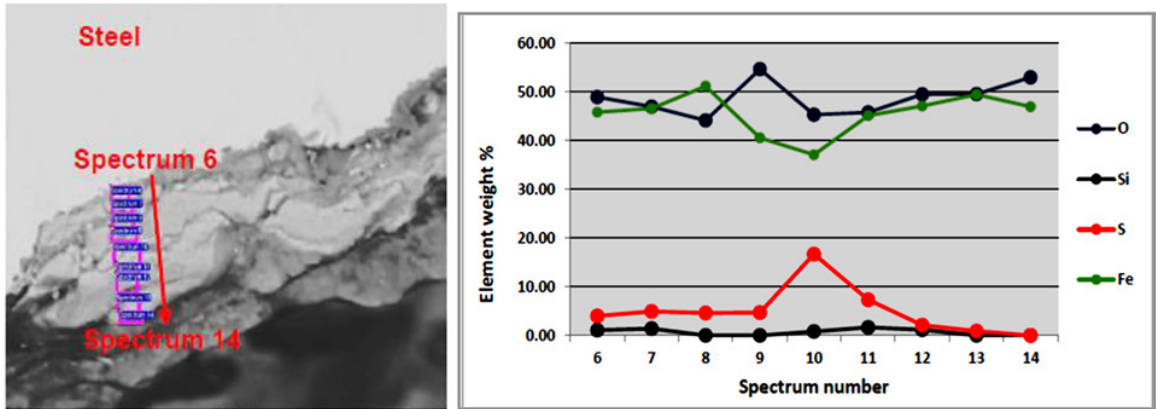


Figure 12—Unit 3 of Station B showing Fe-O rich inner and outer layers with low S, and Fe-O rich middle layer with higher levels of S

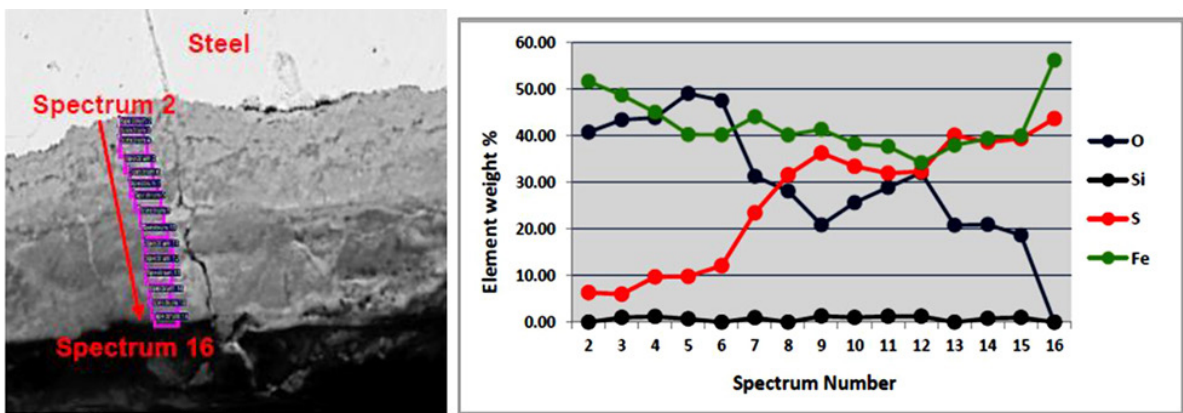


Figure 13—Unit 1 of Station B showing Fe-S rich inner and middle layers with low O, outer layer rich in Fe oxide with higher levels of sulphur and fly ash

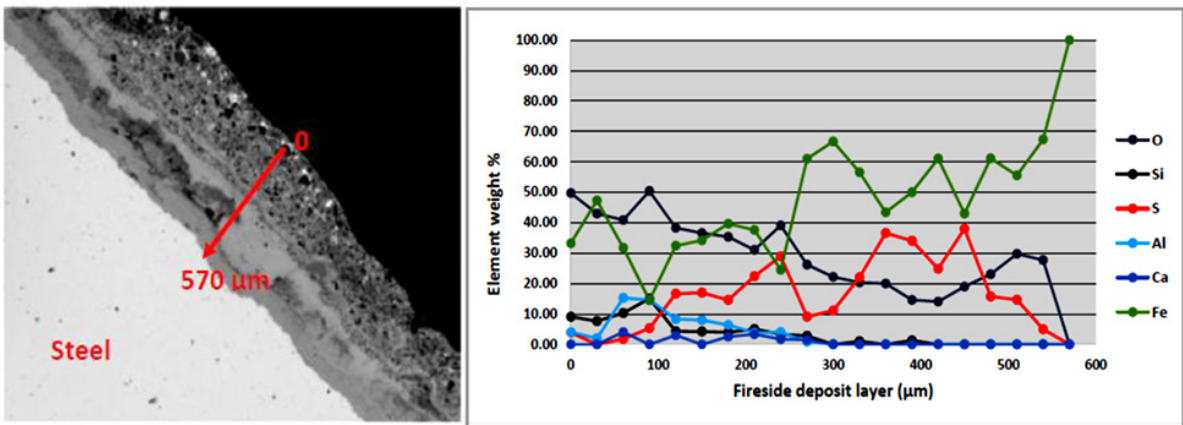


Figure 14—Unit 4 of Station C showing Fe-O rich inner and outer layers and moderate levels of Fe-O and Fe-S in the middle layer. High concentration of fly ash in the outer layer

### X-ray diffraction (XRD)

XRD analysis of the fireside deposits from the three power stations produced correlating results. A high content of haematite and magnetite was detected, with consistent detection of pyrrhotite (FeS). Fly ash particles were also identified (predominantly quartz and mullite) as well as coal constituents such as pyrite, galena, and anglesite (PbSO<sub>4</sub>).

*Station A:* The XRD analysis revealed high levels of Fe<sub>2</sub>O<sub>3</sub> and Fe<sub>3</sub>O<sub>4</sub> with pyrrhotite in small quantities (1.4–3.7 wt.%). Small quantities of quartz and mullite (fly ash) were also detected.

*Station B:* The fireside deposit consisted predominantly of Fe<sub>3</sub>O<sub>4</sub> and low levels of Fe<sub>2</sub>O<sub>3</sub>. Iron-sulphur rich phases were detected, and these included pyrrhotite, pyrite, and traces of galena (PbS). Fly ash particles identified include mullite, quartz, and jarosite (K<sub>2</sub>O·3Fe<sub>2</sub>O<sub>3</sub>·4SO<sub>3</sub>·6H<sub>2</sub>O). The concentrations of pyrrhotite were wide spread, with 3.7–5.6 wt.% for unit 1 and with 40–50 wt.% for unit 3. The difference in the levels of pyrrhotite for unit 1 and unit 3 may be an indication of the furnaces operating under different combustion conditions, with unit 3 possibly being exposed to prolonged reducing conditions.

# Investigation of the mechanism for fireside corrosion in coal-fired boilers in South Africa

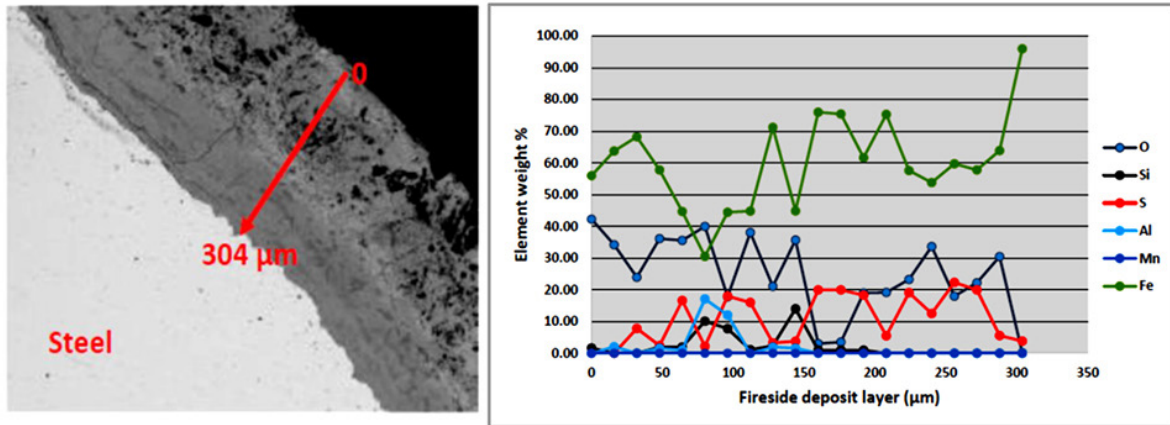


Figure 15—Unit 6 of Station C showing Fe-O rich inner and outer layers, low levels of S, and Fe-O/Fe-S middle layer. Low levels of fly ash particles in the outer layers

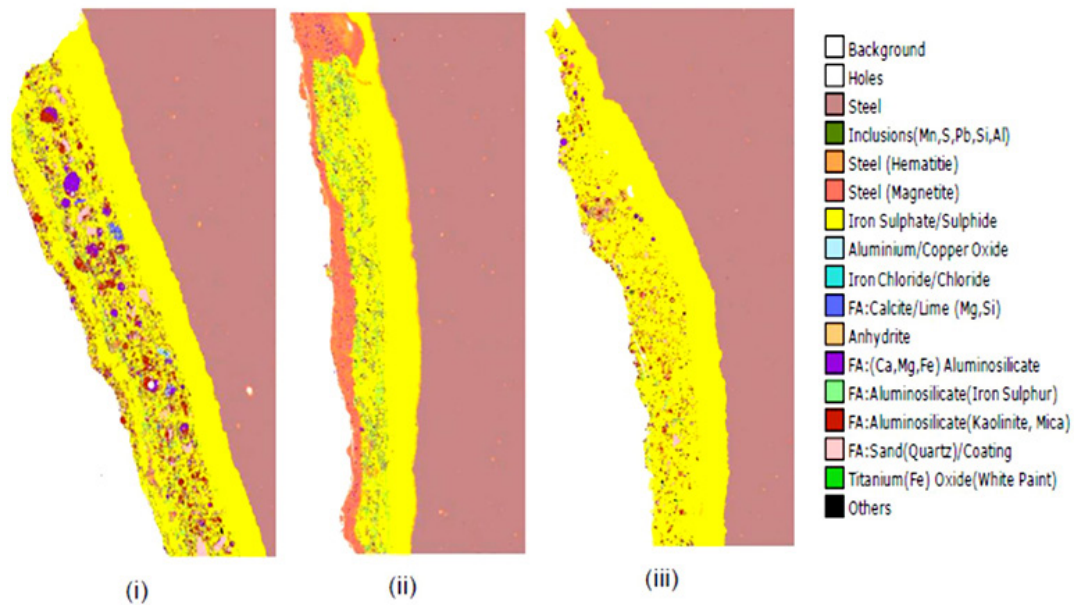


Figure 16—QEMSCAN characterization of the fireside deposits from Station A for (i) unit 1, (ii) unit 3, and (iii) unit 4

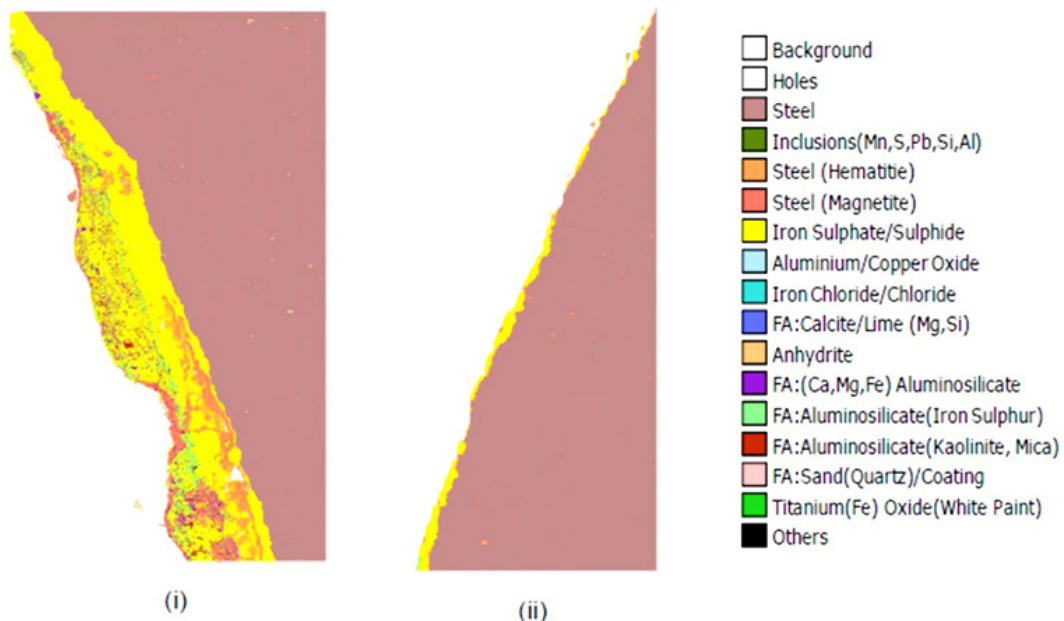


Figure 17—QEMSCAN characterization of the fireside deposits from Station C for (i) unit 4 and (ii) unit 6

## Investigation of the mechanism for fireside corrosion in coal-fired boilers in South Africa

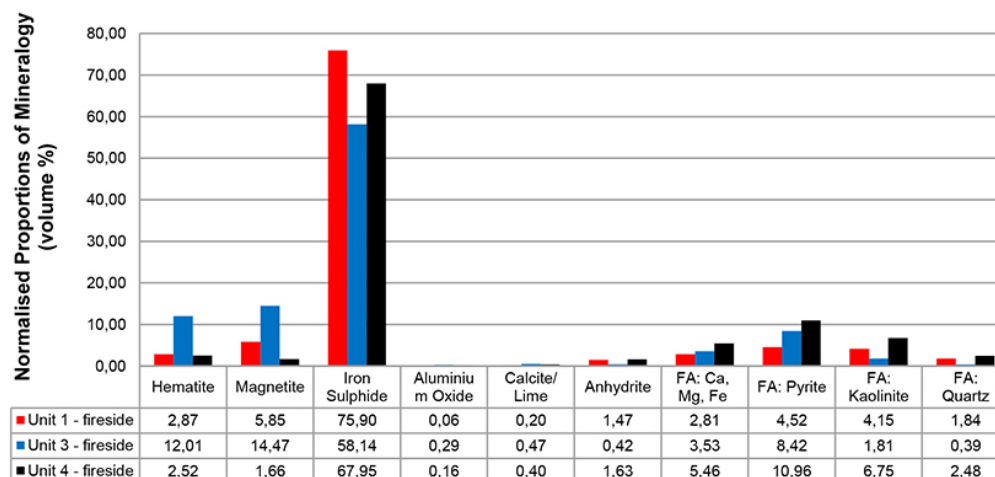


Figure 18—Quantitative mineralogy estimates of the fireside deposits for Station A

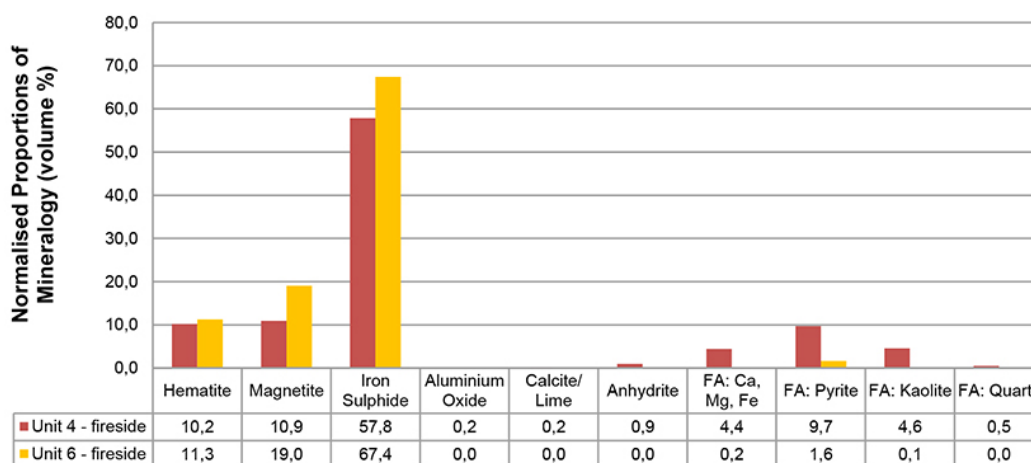


Figure 19—Quantitative mineralogy estimates of the fireside deposits for Station C

*Station C:* The fireside deposit on the tubes from both units of Station C showed high levels of pyrrhotite. Differences were seen in the concentrations of magnetite; the fireside deposit from unit 6 had higher concentrations than unit 4. The difference in the morphology of unit 4 and unit 6 fireside deposits may be indicative of the different furnace environments. The high concentration of pyrrhotite and iron oxide phases in unit 6 samples suggests the existence of alternating oxidizing and reducing conditions, whereas in unit 4 it appears that conditions were reducing for a longer time, which resulted in the formation of pyrrhotite and minimal iron oxide phases.

### Differential thermal analysis (DTA)

DTA results for stations A and B revealed similar thermal behaviour. Peaks were generally measured at temperatures from 950 to 1250°C. On isolated samples from stations A and B, lower temperature activities were indicated at 565°C and 541°C respectively, as shown in Figures 20 and 21. These thermal activities seem to correlate with a survey reported by Bryers (1995) on the thermal behaviour of minerals commonly found in coal. Bryers showed that kaolinite transforms into metakaolinite at temperatures around 500°C, which further transforms into other forms of aluminosilicate at around 925°C and 1100°C. At

lower temperatures pyrite ( $\text{FeS}_2$ ) oxidizes to form FeO and Fe sulphide, which occurs at 475°C. FeO transforms further into  $\text{Fe}_2\text{O}_3$  at 525°C. The low-temperature peaks (at 541 and 565°C) measured on Station A and B samples are likely an indication of the oxidation of pyrite to FeS and  $\text{Fe}_2\text{O}_3$ , whereas the thermal peaks measured above 900°C may represent metakaolinite transformation into other forms of aluminosilicate such as mullite.

### Discussion

The systematic investigation and characterization of the fireside deposits on the furnace wall boiler tubes from the three coal-fired power stations yielded unambiguous results that indicate the same mechanism of fireside corrosion. SEM-EDS and QEMSCAN analyses revealed that the fireside scale was composed of three distinct layers with a Fe-oxide and Fe-sulphide rich inner layer, a Fe-sulphide rich middle layer, and the outer layer consisting of low Fe-sulphide, high Fe-oxide, and low to moderate levels of fly ash particles. The iron oxide was mainly in the form of  $\text{Fe}_3\text{O}_4$  and  $\text{Fe}_2\text{O}_3$  and the iron sulphide was identified as predominantly pyrrhotite (FeS), with low levels of galena (PbS) and pyrite ( $\text{FeS}_2$ ). Fly ash particles consisted mostly of silica ( $\text{SiO}_2$ ) and aluminosilicate associated with calcium and magnesium. The thermal phase transformations of aluminosilicate,

## Investigation of the mechanism for fireside corrosion in coal-fired boilers in South Africa

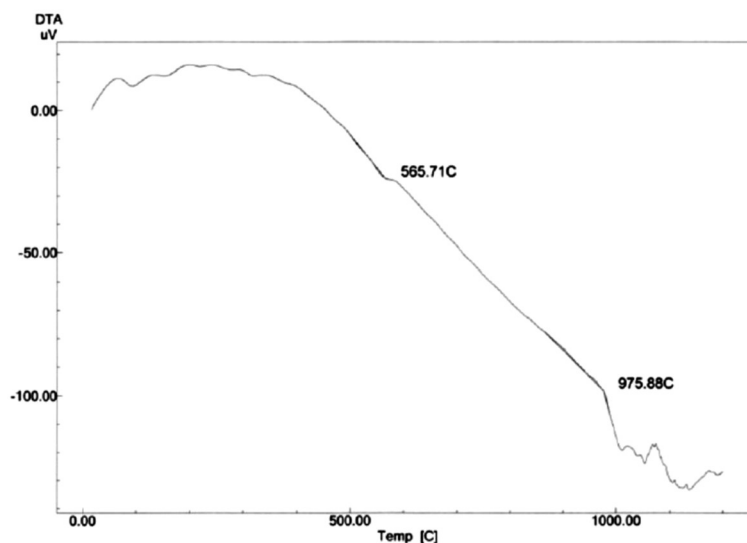


Figure 20—Thermal behaviour of the fireside deposit on Station A tubing sample

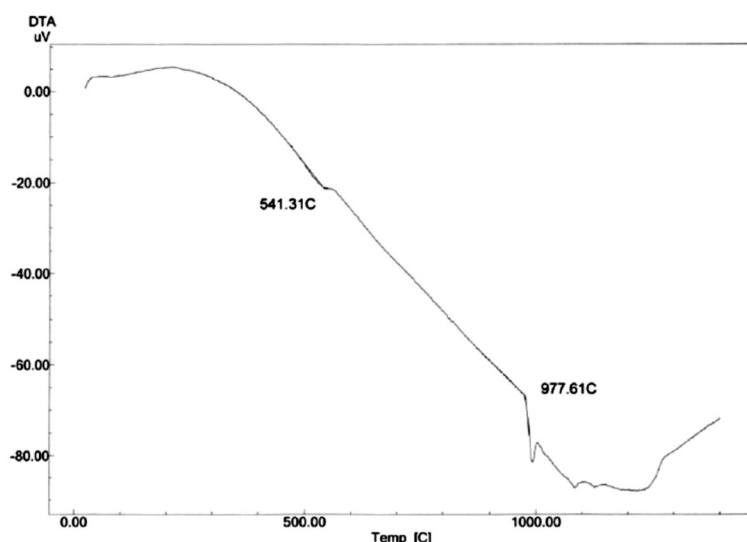


Figure 21—Thermal behaviour of the fireside deposit on Station B tubing sample

*i.e.* metakaolinite, into mullite, were detected consistently at temperatures in the range 950–1250°C, which concurs with thermal behaviour described by Bryers (1995). Lower temperature peaks were measured between 500 and 600°C, indicating pyrite ( $\text{FeS}_2$ ) transformation to FeS,  $\text{Fe}_2(\text{SO}_4)_2$ , and FeO (Corey, 1964). The coexistence of high levels of pyrrhotite with iron oxide and the presence of pyrite in the fireside deposit is indicative of reducing conditions in the furnace as well as on the surface of the boiler tubes.

The morphology and characteristics of the fireside deposits from stations A, B, and C contradict the theory presented by Reid, Corey, and Cross (1945) and Srivastava, Godiwalla, Banerjee (1997), who identified the pyrosulphates, molten at temperatures exceeding 398°C for sodium pyrosulphate ( $\text{Na}_2\text{S}_2\text{O}_7$ ) and 454°C for potassium pyrosulphate ( $\text{K}_2\text{S}_2\text{O}_7$ ), as being responsible for fireside corrosion of boiler tubes. Neither sodium nor potassium were detected in the fireside deposits from stations A, B, and C. Instead, a phase rich in iron sulphide was identified consistently. French (1982) and Yu *et al.* (2017), in several failure investigations of furnace wall tubes, consistently detected sulphur, oxygen, iron, silicon, and chromium in the ash deposits,

and also identified this type of fireside corrosion mechanism. No sodium, potassium, or chlorine were detected in these studies. French (1982) suggests that corrosion attack on the furnace wall tubes is associated with sulphides and requires strongly reducing conditions at the tube surface. He further states that carbon is required to stabilize the sulphites that form; carbon can enter the ash deposit either as unburned char or by deposition from carbon monoxide. Yu *et al.* (2017) found that the corrosion products were composed mostly of iron-containing sulphide and magnetite, and as a result classified the corrosion in that power plant as the sulphide corrosion. They further state that high-temperature corrosion of the sulphide type is due mainly to the large amounts of  $\text{H}_2\text{S}$ , detached sulphur, and unstable FeS that would be formed in the oxygen-deficient conditions when a high-sulphur coal is burned.

Reducing conditions occur when there is limited excess oxygen (< 2%) in the furnace. Bakker (1998) states that low excess  $\text{O}_2$  favours the gasification process over combustion. Gasification results in the formation of  $\text{H}_2\text{S}$  and limits oxidation of CO and combustion of pyrite ( $\text{FeS}_2$ ). This occurs through the reaction of sulphur in the coal ( $\text{FeS}_2$ ,  $\text{S}_{(\text{org})}$ ) and some  $\text{H}_2$  present

## Investigation of the mechanism for fireside corrosion in coal-fired boilers in South Africa

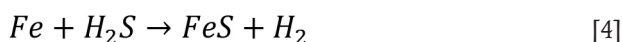
in the flue gas, which can be partially converted into  $H_2S$  instead of  $SO_2$  (Davis *et al.*, 2001; Chou, 1984-1986) through the following reactions:



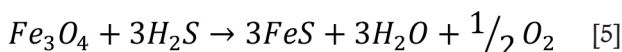
Reid, Corey, and Cross (1945) observed that under highly reducing conditions the pyrite is not completely burnt and the unburned pyrite is transported to the tube surface through flame impingement and may react directly with the iron in the tube walls, resulting in sulphidation:



The high amounts of CO and  $H_2S$  favour a shift in the chemical equilibria for the sulphur species in the flue gas towards higher sulphur potentials and thus allow sulphidation of the metal to take place as well as oxidation (Bakker, 1998). When  $H_2S$  is present in the flue gas, it will preferentially react with iron in the furnace wall tubes, through molecular diffusion, to form pyrrhotite (FeS):



By solid-state diffusion, already-formed  $Fe_3O_4$  may also be transformed to FeS:



The substoichiometric conditions in the furnace were confirmed by the morphology and characteristics of the fireside deposits found on tubings from station A, B, and C, with the inner layer consisting of  $Fe_3O_4$ ,  $Fe_2O_3$ , and FeS, the middle layer rich in FeS, and the outer layer rich in iron oxide, fly ash, and unburnt coal.

Davis *et al.* (2001) found that when the furnace of a pulverized coal boiler is operating under oxidizing conditions, corrosion rates will be negligible and the tube life will exceed the expected life. These conditions enable the formation of dense, adherent and protective mixed oxide/sulphide deposits leading to parabolic rate constants, as described in Equation [6], and are dependent only on metal temperature, with no effect of coal composition or heat flux.

$$K_{Po} = A \cdot e^{-(Q_o/RT)} \quad [6]$$

where

$K_{Po}$  is the parabolic rate constant ( $cm^2 \cdot s^{-1}$ ) under oxidation

$A$  is a constant

$Q_o$  is the activation energy for oxidation ( $J \cdot mole^{-1}$ )

$R$  is the gas constant ( $8.3143 J/K \cdot 1 \cdot mole^{-1}$ )

$T$  is temperature (K).

When the furnace operates under reducing conditions ( $O_2 < 0.5\%$ ,  $CO > 2\%$ ) in the absence of chlorine ( $Cl < 0.05\%$ ), the corrosion mechanism shifts progressively from oxidation towards sulphidation as the CO content of the flue gas increases and the  $O_2$  content declines. Increasing the CO content of the flue gas increases the corrosion rates via the formation of progressively more sulphide within the deposit as described in Equation [7].

$$K_{Pr} = B \cdot (\%CO)^n \cdot e^{-(Q_r/RT)} \quad [7]$$

where

$K_{Pr}$  is the parabolic rate constant ( $cm^2 \cdot sec^{-1}$ ) under reducing conditions

$B$  is a constant

$Q_r$  is the activation energy for mixed oxidation sulphidation ( $J \cdot mole^{-1}$ )

$\%CO$  is the percentage of CO in the local combustion environment.

Gas analysis at unit 1 of Station A correlates with the findings by Davis *et al.* (2001). High levels of CO were measured at the furnace wall (up to 38 000 ppm) and furnace exit ( $\geq 3500$  ppm) (Moodley, 2010, and van Wyk, 2010), which are areas with high wall thinning due to fireside corrosion. High CO concentrations are indicative of limited combustion caused by low excess  $O_2$ . These conditions promote the formation of FeS-rich deposits as seen in unit 1 of Station A. Sulphide deposits allow higher rates of transport (diffusion) of iron cations than oxides, and the strength and adherence of the deposit decrease with increasing FeS content while its growth rate and permeability increase significantly. These deposits are also brittle and poorly adherent, so they readily crack, spall, and are easily removed by soot blowing or thermal cycling. The result is increased metal loss, which becomes the dominant factor in tube life. The morphology and characteristics of the fireside deposits on tubes from the three power stations are indicative of a sulphidation mechanism of fireside corrosion caused by reducing conditions in the furnace.

### Conclusions

This investigation was aimed at gaining a better understanding of the mechanism(s) under which fireside corrosion is taking place on furnace wall tubes in Eskom's coal-fired boilers, and the role that the combustion process has played in promoting this fireside corrosion mechanism. The knowledge and understanding acquired from this study will not only be beneficial to the conventional subcritical coal-fired boilers, but also to subcritical boilers operated with low- $NO_x$  burners as well as supercritical boilers.

The conclusions drawn from the tests and analyses are as follows.

1. The mechanism of fireside corrosion taking place on the furnace walls in boilers at power stations A, B, and C is sulphidation due to FeS deposition. The main contributors to FeS deposition are reducing conditions in the furnace caused by high CO ( $> 2000$  ppm) and low excess  $O_2$  ( $< 2\%$ ) in the flue gas and on the tube surface.
2. Sulphide scales allow higher rates of transport of iron cations than oxides, and they are brittle and poorly adherent so they readily crack and spall. The result is increased tube wall thinning, which becomes the dominant factor in tube life.
3. Sulphidation corrosion can be mitigated through effective combustion, which can be achieved by controlling the amount of free oxygen in the flue gas, within acceptable limits,  $\geq 2\%$ , minimizing the amount of CO in the flue gas to below 2000 ppm, avoiding flame impingement on the tubes, and ensuring the use of the correct coal particle size to reduce the amount of unburned coal in the ash deposits.
4. The degree and extent of fireside corrosion is likely to increase in boilers operating with low- $NO_x$  combustion techniques and those operating at supercritical conditions. It is in these types of boilers where effective combustion process is highly necessary.

## Investigation of the mechanism for fireside corrosion in coal-fired boilers in South Africa

### Acknowledgements

The author gratefully appreciates the support of Eskom Research, Testing and Development management.

### References

- ASTM A106/A106M:18. 2018. Standard specification for seamless carbon steel pipe for high-temperature service. ASTM International, West Conshohocken, PA.
- ASTM A370. 2013. Standard test methods and definitions for mechanical testing of steel products/ ASTM International, West Conshohocken, PA. pp. 12–13.
- BAKKER, W. 1998. Waterwall wastage in low NO<sub>x</sub> boilers: Root causes and remedies. Report TR11155. Electric Power Research Institute, Charlotte, NC.
- BRYERS, R.W. 1995. Fireside slagging, fouling, and high-temperature corrosion of heat-transfer surface due to impurities in steam-raising fuels. *Progress in Energy & Combustion Science*, vol. 22. pp. 29–120.
- BS EN 10216-2. 2013. Seamless steel tubes for pressure purposes – Technical delivery conditions, Part 2: Non-alloy and alloy steel tubes with specified elevated temperature properties, BSI Standard Publications, London.
- CHABULA, N.D. 2009. Metallurgical analysis of failed boiler tubes. *Eskom Generation Procedure GPC 36-5*. Sandton, South Africa. pp. 5–6.
- CHOU, C.L. 1984-1986. Distribution of sodium, chlorine, and sulphur in Illinois coals removal by cleaning and their behaviour during combustion. Final Technical Report. Illinois State Geological Survey.
- COREY, R.W. 1964. Measurements and significance of the flow properties of coal ash slag. *Bulletin* 618. US Bureau of Mines.
- DAVIS, C.J., JAMES, P.J., PINDER, L.W., and MEHTA, A.K. 2001. Effects of fuel composition and combustion parameters on furnace wall fireside corrosion in pulverised coal-fired boilers. *Materials Science Forum*, vol. 369-372. pp. 857–864.
- DOOLEY, R.B. and McNAUGHTON, W.P. 2007. Boiler and heat recovery steam generator tube failures: Theory and practice. Vol. 2. *Manual* 1012757. Electric Power Research Institute, Charlotte, NC.
- FRENCH, D.N. 1982. Furnace wall corrosion problems in coal fired boilers, corporate quality assurance. *Proceedings of the National Association of Corrosion Engineers Conference*, Houston, TX, 22–26 March. <https://www.babcockpower.com/wp-content/uploads/2018/02/furnace-wall-corrosion-problems-in-coal-fired-boilers.pdf>
- HARB, J.N. and SMITH, E.E. 1990. Fireside corrosion in PC-fired boilers. *Progress in Energy and Combustion Science*, vol. 16. pp. 169–190.
- HATT, R.M. 1990. Fireside deposits in coal-fired utility boilers, Island Creek Corporation. *Progress in Energy and Combustion Science*, vol. 16. pp. 235–241.
- MOODLEY, L. 2010. Station A Unit 1 suction pyrometry tests economiser outlet measurements, revision 6. Research, Testing and Development, Eskom, Sandton, South Africa.
- REID, W.T. 1984. The relation of mineral composition to slagging, fouling and erosion during and after combustion. *Progress in Energy and Combustion Science*, vol. 10. doi:10.1016/0360-1285(84)90100-X
- REID, W.T., COREY, R.C., and CROSS, B.J. 1945. External corrosion of furnace-wall tubes – I History and occurrence. *Transactions of the ASME*, vol. 67. pp. 279–285.
- SRIVASTAVA, S.C., GODIWALLA, K.M., and BANERJEE, M.K. 1997. Fuel ash corrosion of boiler and superheater tubes. *Journal of Materials Science (UK)*, vol. 32, no. 4. pp. 835–849.
- SYED, A., SIMMS, N., and OAKLEY, J. 2011. Fireside corrosion study of superheater materials in advanced power plants. School of Applied Science, Cranfield University. <http://dspace.lib.cranfield.ac.uk/handle/1826/7181>
- VAN WYK, D.C. 2010. Station A preliminary report: Gas analysis test on Unit 1. Generation Business Unit, Eskom, Sandton, South Africa.
- YU, X., GONG, B., GAO, Q., ZHAO, Y., TIAN, C., and ZHANG, J. 2017. Investigation of fireside corrosion at water-cooled wall from a coal-fired power plant in China. China Electric Power Research Institute. ◆



16-17 AUGUST 2021

# WORLDGOLD ONLINE CONFERENCE 2021



**SAIMM**  
THE SOUTHERN AFRICAN INSTITUTE  
OF MINING AND METALLURGY



## TOPICS

World Gold 2021 will reflect on the following key issues:

- Future gold deposits
- Brownfield gold exploration successes
- Gold mining
- Geometallurgy
- Sampling
- Mineral Processing
- Extraction and refining
- Overcoming operational challenges, success stories

- Rapid deployment plants
- New technology
- Human resources
- Financial resources

Thus, be agile, focus on reduced environmental, social and health impacts while improving resource, mining, processing, and energy efficiencies.

CPD Points: 2 ECSA CPD Points

SAIMM ONLINE  
CONFERENCE

Re-thinking  
gold operations  
for the future



# Mechanical properties and damage mode of cemented tailings backfill in an acidic environment

Y. Huang<sup>1</sup>, G. Wang<sup>1</sup>, Y. Rao<sup>2</sup>, and W. Liu<sup>2</sup>

## Affiliation:

<sup>1</sup> School of Civil Engineering, Changsha University of Science and Technology, Changsha, Hunan China.

<sup>2</sup> Jiangxi Key Laboratory of Mining Engineering, Jiangxi University of Science and Technology, Ganzhou, Jiangxi, China.

## Correspondence to:

Y. Huang

## Email:

huangyounger@163.com

## Dates:

Received: 13 Jan. 2020

Revised: 19 Mar. 2021

Accepted: 26 Mar. 2021

Published: June 2021

## How to cite:

Huang, Y., Wang, G., Rao, Y., and Liu, W. 2021

Mechanical properties and damage mode of cemented tailings backfill in an acidic environment.

Journal of the Southern African Institute of Mining and Metallurgy, vol. 121, no. 6, pp. 317–324.

## DOI ID:

<http://dx.doi.org/10.17159/2411-9717/1093/2021>

## ORCID

Y. Huang

<https://orcid.org/0000-0002-8014-405X>

G. Wang

<https://orcid.org/0000-0002-6536-234X>

## Synopsis

The properties and deterioration in strength of cemented tailings backfill (CTB) in the underground acidic environment under oxidizing conditions were studied. X-ray diffraction analysis and scanning electron microscopy of the surface of the CTB was carried out, and the sulphuric acid corrosion mechanism elucidated. The properties tested included compressive strength, elastic modulus, cohesion, internal friction angle, variation in the hydrogen ion concentration, and stress-strain relationship in different corrosion periods. The damage model of the CTB was established considering the effects of parameters such as corrosion time and strain on the damage evolution. It was found that the compressive strength, elastic modulus, cohesion (binder effect), and internal friction angle increased at first and then decreased with exposure time. In the long term, the peak stress decreased with corrosion time while the peak strain increased; elastic modulus, and deformation modulus also decreased. The damage caused by corrosion and by load were related by means of a mathematical model, which revealed the relationships between sulphuric attack, load, and damage to backfill in complex underground environments. During corrosion, the expansion of gypsum and ettringite caused microfractures in the CTB. With increasing corrosion time, micro-cracks developed and proliferated. The mechanism of corrosion damage was found to be the dissolution of hydrogen ions and a sulphate ion reaction that produces an expansive substance, resulting in deterioration of the strength of CTB.

## Keywords

underground environment, sulphuric acid corrosion, porosity, cemented tailings backfill, damage evolution model.

## Introduction

Underground mining operations can bring problems such as overburden pressure, surface subsidence, and instability of mined-out areas. At the same time, tailings dams occupy large areas of land, are increasingly costly to build, and carry the risk of environmental pollution. Backfilling of underground workings with cemented tailings is one of the effective methods of solving these problems. The backfill plays a structural role in the mining area (Cai, 1985), and thus the strength of the backfill is of paramount importance.

The backfill is composed of water, tailings, and cementing materials, among others. Much research has focused on the influence of different proportions of ingredients on the strength of backfill (Alireza and Fall, 2016; Djurdjevic, Ignjatovic, and Ljubojev 2016; Yang, Yang, and Gao, 2016; Liang, Dong, and Jiang, 2015; Li, Feng, and Guo, 2016a; Li, Jin, and Tan, 2016b; Chang, Zhou, and Qin, 2009; Li *et al.*, 2005; Cao, Song, and Xue, 2016; Song, Li, and Lei, 2012). This research provides a theoretical basis for the proportions of ingredients. However, backfill strength is determined not only by intrinsic factors, but also by external influences. In addition, Li, Jin, and Tan (2016) found that the loading rate had a significant effect on the uniaxial compressive strength and secant modulus of the backfill. As regards the influence of the properties of the backfill, Nie, Wang, and Huang (2018) found that different water contents have a significant influence on the strength of the backfill. However, only limited research has been done on the influence of corrosion on the strength of the backfill. Such research as has been done has focused mainly on corrosion by salts, such as NaCl, Na<sub>2</sub>SO<sub>4</sub>, Na<sub>2</sub>CO<sub>3</sub>, and other solutions (Sun *et*

# Mechanical properties and damage mode of cemented tailings backfill in an acidic environment

*et al.*, 2015a, 2015b, 2015c, 2015d; Zhang, 2017). Acid minewater (Ning, 2000; Dai *et al.*, 2007; Liu, Zhao, and Hun, 2008; Yang *et al.*, 2009; Huang, 2018) produced during mining and beneficiation corrodes the backfill, and affects its strength, thus affecting the stability of the goaf to a certain extent. Furthermore, there is a difference between acid solution and salt corrosion (Wang, 2017), and the tailings composition at each mine is different.

In this research we used accelerated corrosion methods (Zhao *et al.*, 2016) to configure sulphuric acid solutions with pH values of 1, 3, and 5. These solutions are referred to in this paper as P1, P3, and P5 respectively. CTB was configured with a ratio of 1:4 (four parts tailings to one part cement), a slurry concentration of 75%, and a standard curing time of 28 days. The CTB was then immersed in different sulphuric acid solutions. Some experiments were conducted to simulate the mechanical characteristics and deterioration of concrete in an acidic environment. The parameters that were tested included compressive strength, elastic modulus, cohesion, internal friction angle, and stress-strain curves over different corrosion periods. In addition, the effect of different hydrogen ion concentrations was studied, and X-ray diffraction (XRD) and scanning electron microscopy (SEM) of the CTB surface were carried out in order to elucidate the corrosion mechanism. A damage model of corroded concrete was established, taking into account the effects of parameters such as corrosion time and strain on the damage evolution. The results of this study enrich the theory of backfill strength and provide a theoretical basis for the design of durable backfill for use in an acid environment.

## Materials

The tailings, which were taken from an iron ore mine, had a specific density of 2.997 g/cm<sup>3</sup> and a bulk density of 1.667 g/cm<sup>3</sup>. A particle size analysis (Table I) showed that the tailings were dominated by fine fractions, and characterized by uneven distribution of the coarse and fine particles. The main chemical constituents of the tailings were SiO<sub>2</sub> (75.6%),

Fe<sub>total</sub> (10.8%), and MgO (3.62%), with minor constituents CaO (2.54%) and Al<sub>2</sub>O<sub>3</sub> (2.29%) as shown in Table II.

The samples were prepared as follows.

1. Prepare the tailings and cement (PC32.5) in a ratio of 4:1, stir evenly, pour mixture into the stirring pot, add tap water, start the mixer, stir for 120 seconds. Stop mixing, wait for 60 seconds, and carefully scrape off the slurry sticking on the blade. Remove the stirrer.
2. Clean the mould before injection moulding, and evenly apply a thin layer of oil on the inner surface of the mould to facilitate demoulding.
3. Put the mixture into the mould (mould dimensions 50 mm diameter × 100 mm height), shake it on the vibrating table of the mortar to make it uniform and dense, then scrape off and smooth the mixture from the surface of the test block, and label the test block.

After 24 hours, the mould was removed and then placed in a box for maintenance. The curing temperature was 20±1°C, humidity ≥95%, and the samples were cured for 28 days before they were transferred to the acid solution. There were three sets of CTB in the experiment, 90 in each group, and a total of 285 CTB samples were prepared.

The pre-test density of the CTB was between 2.04 g/cm<sup>3</sup> and 2.16 g/cm<sup>3</sup>, the longitudinal wave velocity was between 1915 m/s and 1990 m/s, and the porosity was between 5.01% and 6.03%.

The reagent used in the experiment was 98% concentrated sulphuric acid, and the water was from the laboratory of Jiangxi University of Science and Technology. First, a certain amount of water was filled into a plastic bucket. To ensure that the amount of water was constant in every test, the water level was marked on the bucket. The volume of water in the bucket was chosen so that the solution level in every test was 2 cm above the CTB surface. Then the pH meter probe, calibrated using pH buffer solutions, was inserted into the water. The concentrated sulphuric acid was slowly dripped into the water using a dropper, with continuously stirring using a glass rod, until the pH of the solution reached the required test value. Lastly, the sulphuric acid solution was poured into the plastic frame of dimensions 62 × 36 × 13 cm (Figure 1). Using the method of accelerating the corrosion rate, the sulphuric acid solution was discarded after soaking for 10 days. The acidic solution was replenished five times at 10-day intervals to the 60th day.

## Methods

The investigation included two main aspects: chemical/mineralogical characterization and mechanical properties assessment. In order to analyse the reaction mechanism and the relationship between the solution and CTB, the pH value of the sulphuric acid solution was monitored by a pH meter, taking readings on days 3, 7 and 10 of each test. This verifies whether H<sup>+</sup> ions participate in the corrosion reaction.

Granularity (mm)	Yield (%)	Cumulative yield (%)
>0.25	3.20	3.20
<0.25 >0.2	9.80	13.00
<0.2 >0.15	8.90	21.90
<0.15 >0.0948	19.30	41.20
<0.0948 >0.0692	9.10	50.30
<0.0692 >0.0502	8.40	58.70
<0.0502 >0.0365	8.70	67.40
<0.0365 >0.0188	10.50	77.90
<0.0188 >0.0137	4.30	82.20
<0.0137 >0.0099	2.10	84.30
<0.0099	15.70	100

Na <sub>2</sub> O	K <sub>2</sub> O	Zn	S	Cu	P	Fe <sub>total</sub>
0.72	0.69	0.019	0.178	0.023	0.19	10.8
TiO <sub>2</sub>	MnO	MgO	CaO	Al <sub>2</sub> O <sub>3</sub>	SiO <sub>2</sub>	
0.16	0.14	3.62	2.54	2.29	75.6	

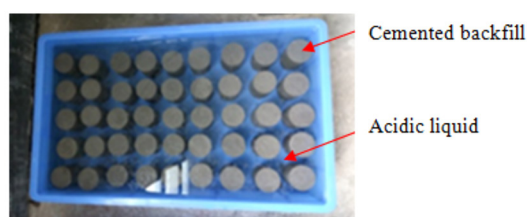


Figure 1—Container for soaking CTB samples

## Mechanical properties and damage mode of cemented tailings backfill in an acidic environment

In addition, the corrosion layer of the CTB during the corrosion process was subjected to XRD analysis to verify whether  $\text{SO}_4^{2-}$  ions participate in the corrosion reaction. After the CTB had been soaked for the set number of days, the surface layer of the sample was removed, dried, ground, and X-ray microanalysis was performed (XRD; Dandonghaoyuan DX-2700, China). JADE software was used for data processing.

In the electron microscopy experiment, after the CTB had been soaked for the set number of days, the surface layer was removed, dried, and broken into small pieces ( $\leq 10 \times 10 \times 5$  mm), and examined using a scanning electron microscope (MLA650F, USA). Specimens were scanned before corrosion and after exposure for 60 days in the P1 environment.

After the CTB samples had been soaked for the set number of days, twelve samples were taken from each of the different acidic solutions and gently rinsed with tap water. The samples were placed in a drying oven for 24 hours at a temperature of  $100^\circ\text{C}$ . An RMT-150C rock mechanics test system was used to test the compressive strength (DZ/T 0276.19-2015, China) and the variable angle shear strength of the samples (DZ/T 0276.25-2015, China). Three samples from a group were tested for uniaxial compressive strength. The shear test was done at angles of  $30^\circ$ ,  $45^\circ$ , and  $60^\circ$  (Figure 2). Three samples were tested at each angle. The tests were done on samples with ages of 10, 20, 30, 40, 50, and 60 days.

### Results and discussion

#### Influence of corrosion on mechanical properties of CTB

It can be seen from Figure 3 that from zero to 10 days the pH of the solution changes from acidic to alkaline. The pH gradually rises from 1 to 9, and there is a large amount of  $\text{H}^+$  consumption, mainly by the  $\text{Ca}(\text{OH})_2$  dissolution reaction. From 10~50 days, the change of pH value is like the change rule for 0~10 days, although the solution remains weakly acidic. This suggests that the dissolution rate of  $\text{Ca}(\text{OH})_2$  is slowing; the surface of the CTB and the pore structure are covered by gypsum crystals and colloids, hindering the reaction from proceeding inside the CTB, thus the chemical reaction rate is lowered, and the phenomenon becomes more obvious with increasing time.

From Figure 4, the pH of the P3 solution changes from 3 to 11 over the first 3 days. Due to the presence of colloidal compounds such as hydrosilicate, tobemullite, *etc.* it is not easy to store in this alkaline environment, which provides a favourable



Figure 2—Shear experiment

chemical environment for the formation of colloids. But the colloids are observed in this solution, although the amount is less than for P1, indicating that the rate of chemical reaction in the acidic environment is slowed down. After 3 days, the pH jumps slightly, and the chemical reaction tends to be relatively stable.

The pH change of the solution under P5 condition is like that of P3. As shown in Figure 5, the pH of the solution becomes alkaline at 3 days, and then tends to be stable. The solubility of hydrogen ions in this environment is weaker than that in the P3 environment. No formation of colloids was observed in this acidic environment.

Regardless of whether the initial solution is strongly or weakly acidic, the pH of the solution increases to neutral. The acidic solution is neutralized and becomes alkaline. Three days after the reaction of the sulphuric acid solution with CTB, the neutralization of  $\text{H}^+$  ions at different pH values is obvious. The neutralization of  $\text{H}^+$  ions decreases and stabilizes after 3 days, indicating that the water chemistry is closely related to time. Eventually, the change in the water chemistry gradually slows down and stabilizes under alkaline conditions. In weak acidic conditions the neutralization of  $\text{H}^+$  ions in the solution is substantial; while in strongly acidic conditions the

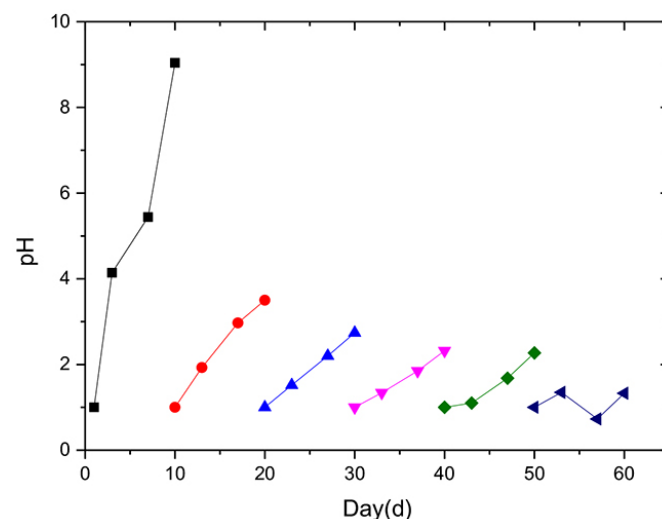


Figure 3—The change in pH of sulphuric acid soaking solution at pH 1

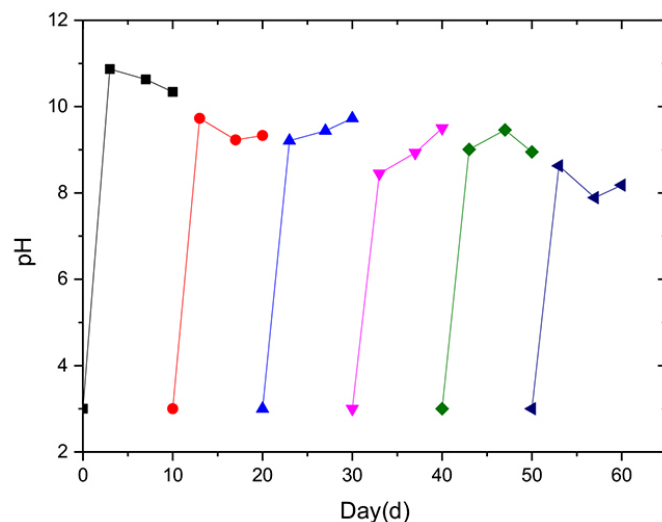


Figure 4—The change in pH of sulphuric acid soaking solution at pH 3

# Mechanical properties and damage mode of cemented tailings backfill in an acidic environment

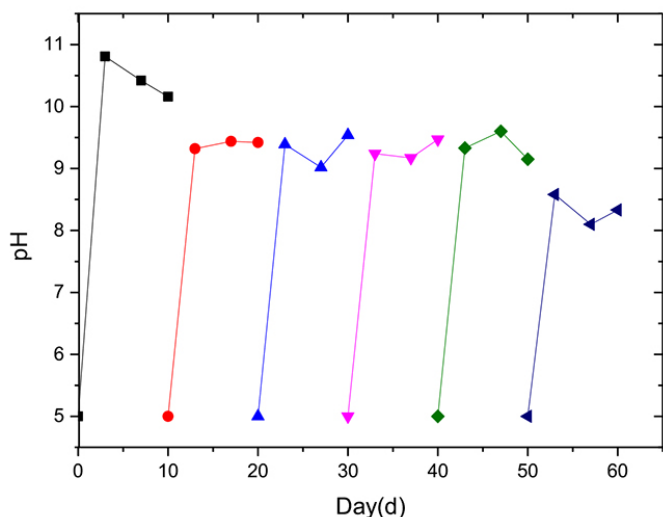


Figure 5—The change in pH of sulphuric acid soaking solution at pH 5

neutralization of  $H^+$  ions does not change substantially. It is evident that the water chemistry under weak acid reaction can change the environmental conditions of the solution and affect the subsequent water chemistry. Under the strong acidic environment, the water chemistry does not change the solution environment. This is due to the coating of the reactive mineral surfaces by secondary mineral precipitates, which decreases the effective reactive surface area, so the effect of the sulphuric acid on the CTB is reduced.

For reasons of brevity, only the XRD spectra of the CTB in the P1 environment, for 60 days of corrosion and before immersion, is presented (Figures 6 and 7). Before corrosion, the spectrum depicts mainly the hydration reaction product C-S-H. When the sample immersed in pH 5 sulphuric acid is corroded for 10 days, in addition to the hydration product, there is a diffraction peak of Aft ( $6CaO \cdot Al_2O_3 \cdot 3SO_3 \cdot 32H_2O$ , Aft). Under these conditions, the amount of ettringite, which filled the micropores of the test piece and optimized the pore structure, was limited. As the etching time increases, the number of  $Ca(OH)_2$  and Aft diffraction peaks decreases, and the number of  $CaSO_4 \cdot 2H_2O$  peaks increases. The sample immersed in pH 1 sulphuric acid exhibits a very minor Aft diffraction peak. The number of  $CaSO_4 \cdot 2H_2O$  diffraction

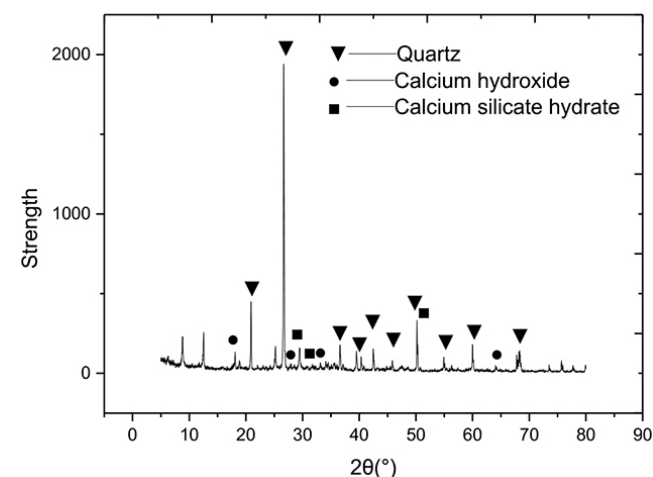


Figure 6—XRD spectrum of the prefilled CTB

peaks decreases, and the sample immersed in pH 3 sulphuric acid shows a similar pattern to that of pH 1. The number of Aft diffraction peaks was larger than that of CTB under the P1 environment, and the number of  $CaSO_4 \cdot 2H_2O$  diffraction peaks greater than in the P1 environment. With the progress of corrosion, the amount of gypsum gradually increases, the porosity of the CTB also increases, and the degree of corrosion increases. A large amount of ettringite and gypsum generates expansion stress inside the test piece. When the expansion stress is greater than the internal tensile stress, micro-cracks are formed and the internal pore structure begins to deteriorate.

As described above, in a sulphuric acid environment a complex chemical reaction occurs between CTB and the solution. The  $Ca(OH)_2$  in CTB increases the porosity, the mesostructure of the test piece is altered, and the mechanical strength of the CTB deteriorates. Gypsum generated by the chemical reaction causes expansion stress in the CTB, resulting in micro-cracks and an increase in volume, thereby decreasing the strength.

Figures 8a and 8b are SEM micrographs of the corrosion products. The backfill is dense before corrosion, and several columnar crystals appear after corrosion. According to Qiao *et al.* (2019), the morphologies of ettringite and gypsum are needle-like. Several ettringite crystals are visible in Figure 8c.

## Effect of corrosion on uniaxial compression behaviour of CTB

Figure 9 shows the change in the uniaxial compressive strength of CTB with time. The trends in the three pH environments are basically similar, rising first and then falling, indicating that the pH has an impact on the strength of CTB. In P1 the CTB reached a peak strength of 5.6 MPa in 10 days, an increase of 45%. In P3 and P5 the CTB reached peak strength of 5.2 MPa in 20 days, an increase of around 34%. This indicates that during the initial stage of corrosion in sulphuric acid the strength of CTB increases. Similar results were obtained by Zhao *et al.* (2016) and Li *et al.* (2014). After 60 days of corrosion, the CTB samples in P1, P3, and P5 increased in strength by 7.1%, 16.7%, and 10.4% respectively, compared with the strength before corrosion. Although there is a slight overall gain in strength over time with exposure to sulphuric acid, the initial increase in strength (during the first 10 or 20 days) deteriorates significantly with time. This is because during the first stages of corrosion the ettringite or gypsum crystals fill the pores, so that the strength of CTB is improved. With increasing of corrosion time, sulphuric acid solution gradually penetrates the CTB, weakening it. In the first instance, the reaction results in an increase in the internal

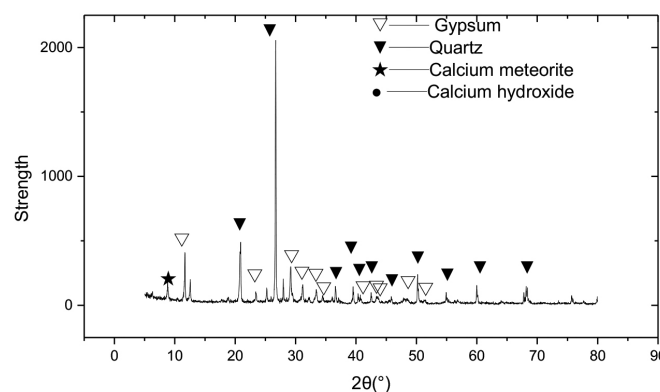


Figure 7—XRD spectrum of CTB after soaking for 60 days at pH 1

# Mechanical properties and damage mode of cemented tailings backfill in an acidic environment

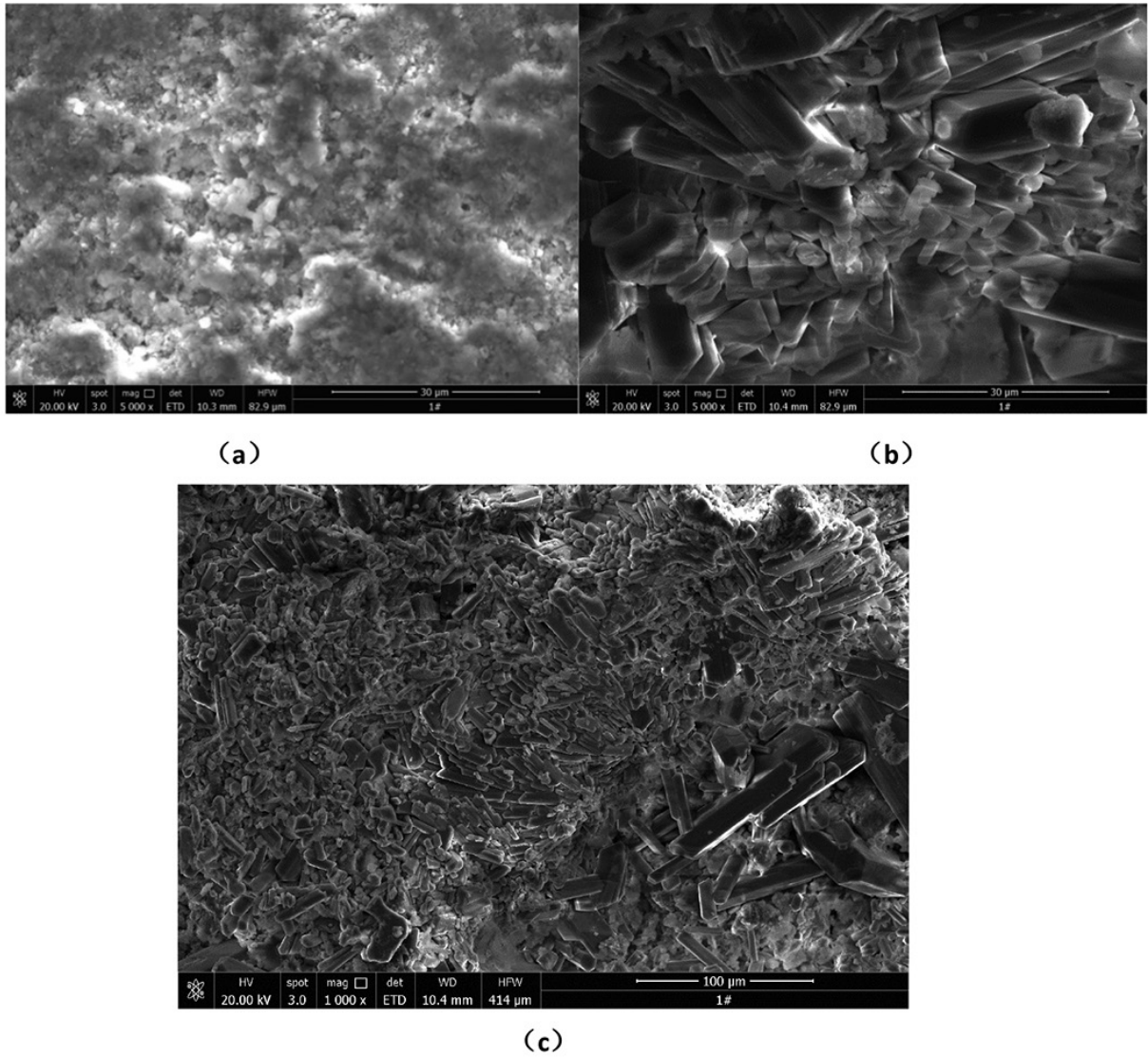


Figure 8—SEM micrographs of corrosion products after soaking in P1 sulphuric acid solution for 60 days. (a) Before etching, 5000x, (b) after etching, 5000x, (c) after etching, 1000x

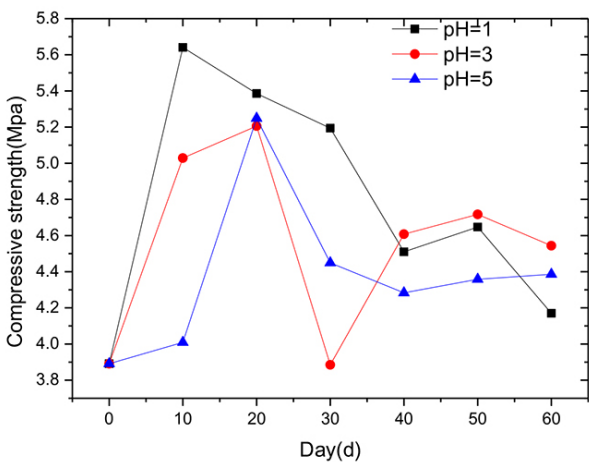


Figure 9—The change in uniaxial compressive strength of CTB with time

porosity of CTB, thus decreasing of effective stress area, with a consequent decrease in compressive strength. Compounding this, the amount of gypsum and other expansion products generated by the chemical reaction increases, resulting in expansion

stresses in the CTB, which lead to micro-cracks and a further reduction in strength. The maximum intensity of the three pH environments is different, perhaps due to the aggressiveness of the solution. The aggressiveness of the P1 solution is higher than P3 and P5, hence the rate of chemical reaction is higher, therefore the time to reach the strength peak value is shorter for P1 than for P3 and P5.

Figure 10 shows the change in the elastic modulus of the CTB with time. The basic trend in the three pH environments is an initial increase in the elastic modulus followed by a gradual decrease. In P1 and P3, the elastic modulus reached its peak value after 10 days. The peak value for P1 was 1.6G Pa, an increase of 118% compared with the pre-corrosion value. The peak value for P3 was 1.2 GPa, 40.5% above the pre-corrosion value, and for P5 the maximum elastic modulus was reached at 20 days, with an increase of 67.8% compared with the pre-corrosion value. Although the pH affected the elastic modulus significantly in the early days, there is no positive correlation between elastic modulus and pH. After 60 days of corrosion, the relative changes for P1, P3 and P5 were 28.3%, 8.4%, and 6.1% respectively, indicating that longer exposure had little effect on the elastic modulus of the filling. The modulus of elasticity can

# Mechanical properties and damage mode of cemented tailings backfill in an acidic environment

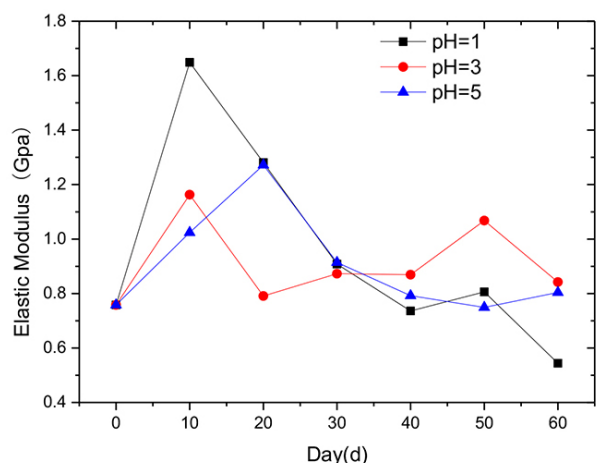


Figure 10—The change in the elastic modulus of CTB with time

be used as an index for judging the susceptibility of a material to elastic deformation – the larger the elastic modulus, the greater the stress required for elastic deformation, which is basically consistent with the change in compressive strength of backfill. During the initial stage of corrosion, the solution fills the CTB's pores, and the degree of cohesion of the filler particles is high, which makes the elastic modulus increase. The change in behaviour may also be related to the degree of cement hydration of the test piece. With increasing corrosion time the porosity increases, the cohesion between the filler particles decreases greatly, and the elastic modulus of the filler decreases. The test results fluctuate because of the dispersion and the difference in the degree of erosion. The reason may be the different solubilities of the solutions.

## Effect of corrosion on cohesion and internal friction angle of CTB

Figure 11 illustrates the trend of cohesion of CTB with time. The cohesion increases at first and then decreases for all the different pH solutions. The cohesion of CTB in P1 and P3 reaches its peak at 20 days, with strengths of 2.8 MPa and 2.96 MPa, respectively, increases of 167% and 150% from the pre-corrosion value. The CTB in P5 reaches its peak strength of 2.5 MPa at 30 days, increasing by 132%. After 60 days of corrosion, the cohesion values of the CTB in P1, P3, and P5 increased by 106%, 40.4% and 57.4% respectively, compared to the pre-corrosion value. This indicates that sulphuric acid enhanced cohesion during the early stages, but this effect deteriorated during the later stages. On the one hand, the gypsum produced by the chemical reaction fills the pores of CTB, which increases the compactness of CTB and its overall cohesion. On the other hand, acid corrosion will destroy the hydration products, such as  $\text{Ca}(\text{OH})_2$ , and destroy the intermolecular cementation. With increasing corrosion time, the damage will intensify, and the cohesion will deteriorate. The cohesion values in P1 and P3 peak earlier than in P5; this is related to the solubility of the ions. The range cohesion values depends mainly related on the dispersion of the samples.

Figure 12 shows the changes in the friction angle of CTB with time. The internal friction angle, although fluctuating, generally decreases in all the solutions. The change range of the internal friction angle of CTB in P5 solution is relatively small, with a maximum of  $31.9^\circ$ , and a minimum of  $9.6^\circ$ . The change in P1 is a maximum of  $41.4^\circ$ , and a minimum of  $13.3^\circ$ . The

chemical reaction rate in the P5 solution is slow, and the reaction products are few. The chemical reaction rate in the P1 solution is the fastest, and the reaction products are more than in P3 or P5. Therefore the pores of CTB in P1 are filled more completely than in P3 and P5, thus the change range of friction angle in P1 is smaller than in P3 and P5. It appears that the internal friction angle of CTB is related to porosity.

## Damage evolution analysis of CTB in corrosion and loading process

Figure 13 depicts the stress-strain curve of CTB in P1 after corrosion for 0, 10, 20, 30, 40, 50 and 60 days. As corrosion progresses, the peak stress  $f_c$  of CTB first increases and then decreases. The elastic modulus of the corroded CTB is taken from the slope of the straight line in the elastic deformation stage on the measured stress-strain curve. The peak secant deformation modulus  $E_p$  is taken from the ratio of the peak stress  $f_c$  to the peak strain  $\epsilon_c$  on the measured stress-strain curve. Both  $E_c$  and  $E_p$  at first increase and then decrease. After soaking for 10 days,  $E_c$  and  $E_p$  increased by 22.2% and 16.1% respectively. After 60 days, the modulus of elasticity decreased to 0.41 times that of the CTB before corrosion, and the peak modulus of deformation reduced to 0.47 times the pre-corrosion value. The peak strain  $\epsilon_c$  is proportional to the corrosion time; this increased by 66.67% after 60 days of soaking.

From examination of the stress-strain curves, the deformation and failure process of CTB can be divided into four stages:

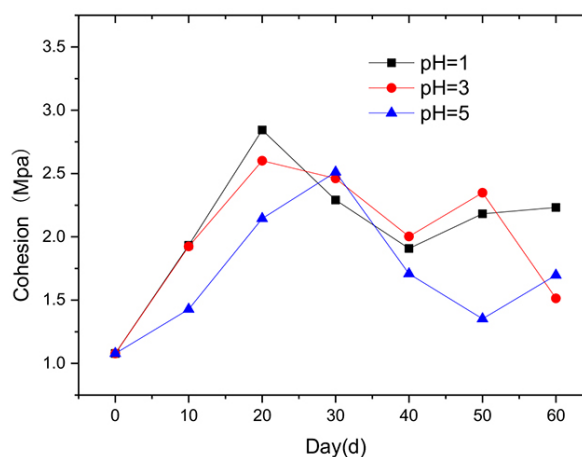


Figure 11—The change in cohesion of CTB with time

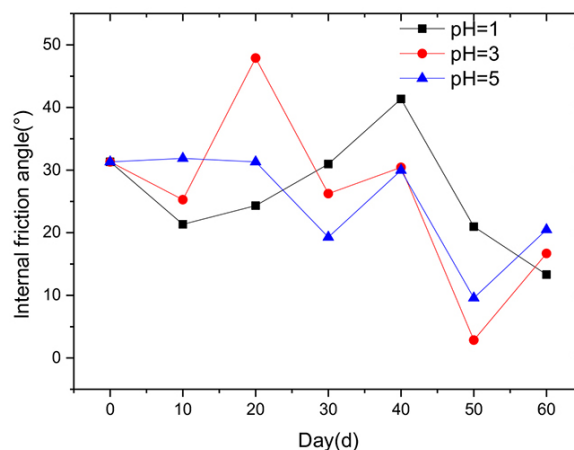


Figure 12—The change in internal friction angle of CTB with time

## Mechanical properties and damage mode of cemented tailings backfill in an acidic environment

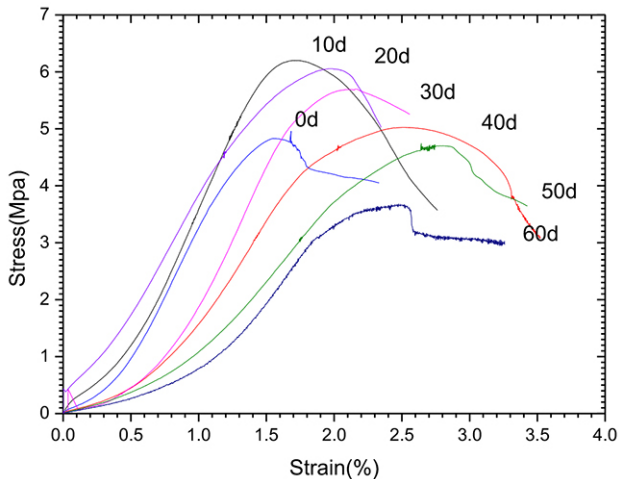


Figure 13—Stress-strain curves for CTB at pH 1 at different ages

- The first stage is the initial deformation stage: CTB is in the initial stage of stress-strain, the graph's curved section is slightly concave upward, and the micropores and micro-cracks in the material are compacted. With prolonged corrosion time, the pore content in CTB increases and the compaction process is more obvious in CTB.
- The second stage is the elastic deformation stage, in which the stress-strain curve of CTB is approximately linear, and the steeper the straight line, the larger the elastic modulus. At the initial stage of corrosion, the elastic modulus of CTB tends to increase. As the corrosion time increases, the elastic modulus gradually decreases.
- The third stage is the yield stage, and the slope of the curve segment decreases as the stress increases. In the initial stage of corrosion, the strength of CTB will increase, and the higher the peak strength, the more obvious is the yield deformation process. As the corrosion time increases, the strength of CTB will gradually decrease.
- The fourth stage is destruction. As the deformation increases, the load-carrying capacity of CTB gradually decreases.

The failure of CTB samples is a process of cumulative damage. The damage during the loading process is regarded as a continuous process. The distribution of mesoscopic defects inside the material is relatively random. After CTB is affected by the external environment, the micro-cracks and cracks in the material continue to evolve and develop in some areas, then macroscopic cracks are formed which cause the structure of CTB to be destroyed. The relationship between the damage factor  $D$  and the statistical distribution density of CTB micro-destruction can be expressed as  $dD/d\varepsilon = \varphi(\varepsilon)$ , where  $\varphi(\varepsilon)$  is a measure of the damage rate of the micro-element during loading. If CTB micro-element strength obeys the Weibull distribution, the damage evolution equations of the loaded CTB are:

$$D = \int_0^\varepsilon \varphi(x) dx = 1 - e^{-\frac{1}{m}(\frac{\varepsilon}{\varepsilon_c})^m} \quad [1]$$

$$m = \frac{1}{\ln\left(\frac{E_0 \varepsilon_c}{\sigma_c}\right)} \quad [2]$$

where  $\varepsilon_c$  is the strain corresponding to the peak stress  $\sigma_c$ ,  $m$  is the material parameter of the damage evolution characteristic

of CTB, and  $E_0$  is the initial elastic modulus before corrosion. There are two kinds of corrosion damage to CTB – the damage caused by sulphuric acid and the damage caused by the load. The strain equivalence promoted by the Lemaitre strain equivalence principle can be used to derive the constitutive relationship of the internal corrosion damage to CTB:

$$\sigma = E_t(1 - D)\varepsilon \quad [3]$$

where  $D$  is the damage factor due to the load, and  $E_t$  is the elastic modulus after corrosion for a period.

The corrosion stress-strain relationship of CTB expressed by the corrosion and the total damage variable  $D_m$  is:

$$\sigma = E_t(1 - D_m)\varepsilon \quad [4]$$

$$D_m = D_t + D - D_t D \quad [5]$$

In the formula,  $D_t$  is the damage factor caused by corrosion,  $D$  is the damage factor caused by the loading, and  $D_t D$  is the coupling term.

It has been seen that corrosion causes the strength of CTB to deteriorate over time. The degree of deterioration can be quantified by an indicator. Various indicators may be used. Elastic modulus is easy to obtain for the damage variable, and the quantitative description of the corrosion damage is as follows:

$$D_t = 1 - \frac{E_t}{E_0} \quad [6]$$

Equations [1], [5], and [6] can be used to derive the total damage evolution equation of CTB under corrosion and load:

$$D_m = 1 - \frac{E_t}{E_0} e^{-\frac{1}{m}(\frac{\varepsilon}{\varepsilon_c})^m} \quad [7]$$

Assuming that CTB is only corroded, the loaded strain  $\varepsilon = 0$ ; at this time  $D_m = D_t$ . When only the damage is considered,  $E_t = E_0$ ; at this time  $D_m = D$ . According to the test data and the result of Equation [7], the evolution curve of the corrosion damage model of CTB samples as shown in Figure 14 is obtained.

It also can be seen from Figure 8 that in an acidic environment, in the long run, the degree of corrosion damage of the CTB is correlated with the corrosion time. That is, the longer the corrosion time, the more serious the deterioration of the sample. In the first instance, corrosion causes the porosity of the CTB sample to increase, hence the effective force area decreases under the load. Therefore, the mechanical strength

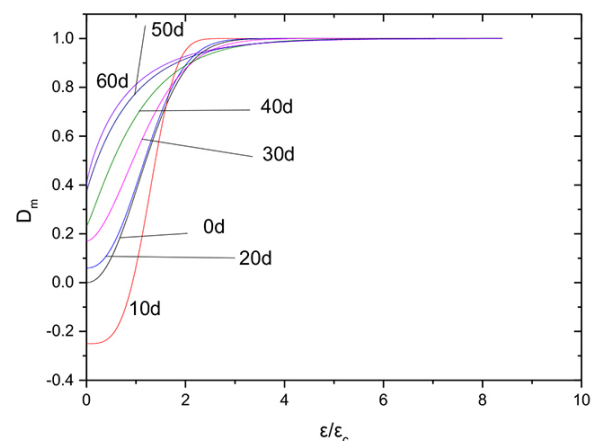


Figure 14—Evolution curve of damage model of CTB corrosion

# Mechanical properties and damage mode of cemented tailings backfill in an acidic environment

properties deteriorate. Compounding this, the amount of gypsum and other expansion products increases due to the corrosion, and when the expansion is greater than the internal cohesiveness of CTB, microfractures are formed. In a corrosive environment, the degree of damage deterioration of CTB increases with increasing strain. At the initial stage of loading, the micropores and defects inside the CTB are 'compacted' (the compaction stage). With the gradual increase of strain, the micropores and micro-cracks in CTB continue to expand and develop into macro-cracks, and the damage is intensified. When the stress on the test piece reaches its peak, the damage is at a maximum.

## Conclusions

CTB samples were fabricated and exposed to sulphuric acid solutions with different pH values. The compressive strength and shear strength of the backfill were measured after immersion for different times, and the pH values of the solutions was measured. The backfill after corrosion was analysed by XRD and SEM. The conclusions are as follows.

1. Sulphuric acid solution corrosion influences the mechanical properties of CTB. Although it is beneficial to the strength of the CTB in the early stages, corrosion is unfavourable in the long term. Compressive strength, modulus of elasticity, and cohesion all change similarly in an acidic environment, showing a trend of increasing first and then gradually decreasing. However, the trend for the internal friction angle is not obvious; it fluctuates while decreasing overall.
2. Sulphuric acid corrosion increases the secondary porosity of the CTB; the corrosion product gypsum forms, causing expansion and micro-fractures in the specimen. With increasing corrosion, the micro-fractures gradually proliferate and expand, causing the volume of the CTB to increase. Both of these phenomena affect the mechanical properties of CTB. In summary, the corrosion failure mechanism of CTB is caused by two failure modes – the neutralization of H<sup>+</sup> and the formation of expansive substances by SO<sub>4</sub><sup>2-</sup> reaction (gypsum formation), which result in the change in the strength of CTB.
3. Regardless of whether the initial solution is strongly or weakly acidic, the pH of the solution changes from acidic to neutral over time; that is, the sulphuric acid solution-filler system becomes alkaline.
4. In the long term, the peak stress of the specimens decreases, the peak strain increases, and the elastic modulus and the peak deformation modulus decrease.

Some limitations of this study may be noted. Firstly, the experiments were carried out in an indoor environment. This is different from the actual situation in the field. In the field, the chemical composition of acidic mine drainage from the oxidation of sulphide minerals is complex. Secondly, the tests were carried out under controlled conditions of solubility, cement-to-tailings ratio, and curing days. The effects of variability in solubility, pH, cement-to-tailings ratio, and curing and exposure days have not been assessed. In addition, considering the influence of sulphur in tailings on the strength of backfill, this investigation is exploratory and focuses on the influence of acidic mine drainage on the strength of CTB, thus the tailings samples did not contain sulphur. Further research is required in the underground environment to assess whether the depth of corrosion attack is significant. If the corrosion is shallow (say 300 mm) relative to the backfill (many metres thick), is the weakening of this outer skin a major factor? Especially when backfill is required

mainly to stabilize areas until such time as adjacent ore has been mined. If the weakening of this outer skin is a major factor, it is recommended that mitigation measures for the generation of acid mine drainage are considered when tailings are used as backfill to avoid corrosion and deterioration in the strength of the backfill material.

## Acknowledgements

The authors gratefully acknowledge financial support from the Hunan Graduate Innovation Fund under Grant No. CX2018B535.

## References

- ALIREZA, G. and FALL, M. 2016. Strength evolution and deformation behaviour of cemented paste backfill at early ages: Effect of curing stress, filling strategy and drainage. *International Journal of Mining Science and Technology*, vol. 5. pp. 809–817.
- CAI, S.J. 1985. Strength characteristics and strength design of cemented filling materials. 1. Strength design of cemented filling materials. *Journal of South Metallurgy College*, vol. 3. pp. 39–46.
- CAO, S.A., SONG, W.D., and XUE, G.L. 2016. Change rule and failure mode of mechanical properties of layered tailings cemented backfill. *Journal of China University of Mining and Technology*, vol. 4. pp. 717–722.
- CHANG, Q.L., ZHOU, H.Q., and QIN, J.Y. 2009. Neural network prediction of paste filling material ratio. *Journal of Mining and Safety Engineering*, vol. 26. pp. 74–77.
- DAI, Y.H., RAO, Y.Z., WU, H., and ZHANG, S.P. 2007. Study on the pollution law of acidic wastewater and heavy metal in mine. *Gold*, vol. 28. pp. 45–47.
- DJURDJEVIC, L., IGNIJATOVIC, D., and LJUBOJEV, M. 2016. Change the uniaxial compressive strength of paste backfill depending on change the parameters. *Mining & Metallurgy Engineering Bor*, vol. 1. pp. 17–24.
- HUANG, Y.G. 2018. Study on mechanical properties of full tailings cemented backfill in acidic solution. Master's thesis, Jiangxi University of Science and Technology, Ganzhou, Jiangxi, China.
- LI, D., FENG, G.R., and GUO, Y.X. 2016. Analysis of strength growth rule of filling body based on response surface method. *Journal of Coal Industry*, vol. 41. pp. 392–398.
- LI, Y.G., JIN, L.Z., and TAN, H. 2016. Loading rate effect test of mechanical properties of cemented backfill. *Journal of Harbin University of Technology*, vol. 48. pp. 49–53.
- LI, Y., ZHANG, J., DENG, F., and BAI, S.W. 2005. Experimental study on strength characteristics of cemented tailing backfill in deep goaf. *Geotechnical Mechanics*, vol. 26. pp. 865–868.
- LIANG, B., DONG, Q., and JIANG, L.G. 2015. Orthogonal test for optimal proportioning of cemented filling material of lead zinc tailings. *Chinese Journal of Safety Sciences*, vol. 12. pp. 81–86.
- LIU, W.Y., XIAO, L.P., and LIANG, B. 2008. Study on treatment of mine acid wastewater and prospect of SAPS technology. *Mining Research and Development*, vol. 28. pp. 71–73.
- LIU, J.Z., ZHAO, C.J., and HUN, B.C. 2008. Stress analysis of cemented filling body. *Nonferrous Mining and Metallurgy*, vol. 24. pp. 12–13.
- NIE, Y.L., WANG, X.J., and HUANG, G.L. 2018. Strength and damage model analysis of pure tailings cemented backfill with different water content. *Silicate Bulletin*, vol. 37. pp. 201–206.
- NING, S.C. 2000. Treatment and improvement of acid wastewater in Nanshan Coal Mine of Maanshan Iron and Steel Company. *Metal Mine*, vol. 6. pp. 43–44.
- QIAO, H.X., CHEN, Z.C., LIANG, J.K., and LI, Y.K. 2019. Sulfate erosion resistance of basalt manufactured sand concrete. *Journal of Architecture and Civil Engineering*, vol. 36. pp. 1422–1428.
- SONG, W.D., LI, H.F., and LEI, Y.K. 2012. Experimental study on cementation performance of Chengchao iron ore tailings. *Mining Research and Development*, vol. 1. pp. 8–11.
- SUN, Q., LI, X.L., WEI, X., and MU, Q.W. 2015a. Experimental study on the effect of chloride corrosion on creep characteristics of filling paste. *Journal of Experimental Mechanics*, vol. 30. pp. 231–238.
- SUN, Q., LI, X.L., WEI, X., and MU, Q.W. 2015b. Experimental study on the effect of mine water corrosion on the strength of filling paste. *Journal of Ceramics Bulletin*, vol. 34. pp. 1246–1251.
- SUN, Q., LI, X.L., WEI, X., and MU, Q.W. 2015c. Study on creep characteristics of paste filling material under sulfate corrosion. *Journal of Safety Science and Technology*, vol. 34. pp. 12–18.
- SUN, Q., LI, X.L., WEI, X., and MU, Q.W. 2015d. Study on strength evolution law of filling paste under corrosion and curing. *Journal of Ceramics Bulletin*, vol. 34. pp. 1480–1484.
- WANG, K. 2017. Study on durability of concrete under acid rain and carbonization and freeze-thaw coupling. Master's thesis, Wuhan University of Technology, Wuhan, Hubei, China.
- YANG, Q., NING, P., CHENG, F.Y., and ZHANG, T.L. 2009. Progress of treatment of acid wastewater in mine. *Metal Mine*, vol. 1. pp. 131–134.
- YANG, X., YANG, Z.Q., and GAO, Q. 2016. Study on cemented filling strength test and optimal ratio decision of mixed filling aggregate. *Geotechnical Mechanics*, vol. 2. pp. 635–641.
- ZHANG, S.G. 2017. Study on corrosion characteristics and safety protection of reinforcing bars in underground filling. *Mining Technology*, vol. 3. pp. 58–60.
- ZHAO, L., LIU, J.H., ZHOU, W.J., and JI, H.G. 2016. Damage evolution and mechanism of concrete erosion at sulfate environment in underground mine. *Journal of Coal Science*, vol. 41, no.6. pp. 1422–1428. ◆

# NATIONAL & INTERNATIONAL ACTIVITIES

2021

**27-30 June 2021 — European Metallurgical Conference, EMC 2021**

Salzburg, Austria

Tel: +49 (5323) 93 79-0

E-Mail: [verein@gdmb.de](mailto:verein@gdmb.de), Website: <https://emc.gdmb.de/contact/>

**28-30 June 2021 — Renewable Solutions for an Energy Intensive Industry Hybrid Conference 2021**

Mintek, Randburg, South Africa

Contact: Camielah Jardine

Tel: +27 11 834-1273/7, Fax: +27 11 838-5923/833-8156

E-mail: [camielah@saimm.co.za](mailto:camielah@saimm.co.za), Website: <http://www.saimm.co.za>

**1-2 July 2021 — The Mine Waste & Tailings Stewardship Conference 2021**

Brisbane, Australia

Website: <https://www.ausimm.com/conferences-and-events/mine-waste-and-tailings/>

**28 July – 22 September 2021 — 5th Mineral Project Valuation Webinar Series**

Contact: Gugu Charlie

Tel: +27 11 834-1273/7, Fax: +27 11 838-5923/833-8156

E-mail: [gugu@saimm.co.za](mailto:gugu@saimm.co.za), Website: <http://www.saimm.co.za>

**3-4 August 2021 — DIMI (Diversity and Inclusion in the Minerals Industry) Online Conference 2021**

*'Empowering the African minerals industry through diversity and inclusion'*

Contact: Camielah Jardine

Tel: +27 11 834-1273/7, Fax: +27 11 838-5923/833-8156

E-mail: [camielah@saimm.co.za](mailto:camielah@saimm.co.za), Website: <http://www.saimm.co.za>

**16-17 August 2021 — Worldgold Online Conference 2021**

Contact: Camielah Jardine

Tel: +27 11 834-1273/7, Fax: +27 11 838-5923/833-8156

E-mail: [camielah@saimm.co.za](mailto:camielah@saimm.co.za), Website: <http://www.saimm.co.za>

**30 August-1 September 2021 — APCOM 2021 Minerals Industry Online Conference**

*'The next digital transformation in mining'*

Contact: Camielah Jardine

Tel: +27 11 834-1273/7, Fax: +27 11 838-5923/833-8156

E-mail: [camielah@saimm.co.za](mailto:camielah@saimm.co.za), Website: <http://www.saimm.co.za>

**21-22 September 2021 — 5th Young Professionals Hybrid Conference 2021**

*'A Showcase of Emerging Research and Innovation in the Minerals Industry'*

The Canvas, Riversands, Fourways, South Africa

Contact: Gugu Charlie

Tel: +27 11 834-1273/7, Fax: +27 11 838-5923/833-8156

E-mail: [gugu@saimm.co.za](mailto:gugu@saimm.co.za), Website: <http://www.saimm.co.za>

**23-24 September 2021 — 3rd Global Engineering Online Symposium**

*'Bridging the gap between research (academia) and industry while transitioning into 4IR'*

Contact: Gugu Charlie

Tel: +27 11 834-1273/7, Fax: +27 11 838-5923/833-8156

E-mail: [gugu@saimm.co.za](mailto:gugu@saimm.co.za), Website: <http://www.saimm.co.za>

**26-29 September 2021 — The 16th International Ferroalloys Congress (INFACON XVI)**

Clarion Hotel & Congress, Trondheim, Norway

[infacon2021@videre.ntnu.no](mailto:infacon2021@videre.ntnu.no)

**18-19 October 2021 — Southern African Rare Earths International Hybrid Conference 2021**

Misty Hills Conference Venue, Muldersdrift,

Johannesburg, South Africa

Contact: Camielah Jardine

Tel: +27 11 834-1273/7, Fax: +27 11 838-5923/833-8156

E-mail: [camielah@saimm.co.za](mailto:camielah@saimm.co.za), Website: <http://www.saimm.co.za>

**25-29 October 2021 — SAMCODES Online Conference 2021 'Good Practice and Lessons Learnt'**

Contact: Gugu Charlie

Tel: +27 11 834-1273/7, Fax: +27 11 838-5923/833-8156

E-mail: [gugu@saimm.co.za](mailto:gugu@saimm.co.za), Website: <http://www.saimm.co.za>

**11 November 2021 — 17<sup>th</sup> Annual Online Student Colloquium 2021**

Contact: Gugu Charlie

Tel: +27 11 834-1273/7, Fax: +27 11 838-5923/833-8156

E-mail: [gugu@saimm.co.za](mailto:gugu@saimm.co.za), Website: <http://www.saimm.co.za>

**15-26 November 2021 — Global Tailings Standards and Opportunities Online Conference 2021**

*'For the Mine of the Future'*

Contact: Gugu Charlie

Tel: +27 11 834-1273/7, Fax: +27 11 838-5923/833-8156

E-mail: [gugu@saimm.co.za](mailto:gugu@saimm.co.za), Website: <http://www.saimm.co.za>

2021

**16-19 May 2022 — 8th Sulphur and Sulphuric Acid Conference 2022**

The Vineyard Hotel, Newlands, Cape Town, South Africa

Contact: Camielah Jardine

Tel: +27 11 834-1273/7, Fax: +27 11 838-5923/833-8156

E-mail: [camielah@saimm.co.za](mailto:camielah@saimm.co.za), Website: <http://www.saimm.co.za>

**14-16 June 2022 — Copper Cobalt Africa In Association with The 10<sup>th</sup> Southern African Base Metals Conference**

Avani Victoria Falls Resort, Livingstone, Zambia

Contact: Camielah Jardine

Tel: +27 11 834-1273/7, Fax: +27 11 838-5923/833-8156

E-mail: [camielah@saimm.co.za](mailto:camielah@saimm.co.za), Website: <http://www.saimm.co.za>

**4-8 July 2022 — 32nd SOMP Annual Meeting and Conference 2022**

Windhoek Country Club & Resort, Windhoek, Namibia

Contact: Camielah Jardine

Tel: +27 11 834-1273/7, Fax: +27 11 838-5923/833-8156

E-mail: [camielah@saimm.co.za](mailto:camielah@saimm.co.za), Website: <http://www.saimm.co.za>

**9-13 July 2022 — Sustainable Development in the Minerals Industry (SDIMI) 2022 10th International Conference**

Swakopmund Hotel and Entertainment Centre, Swakopmund, Namibia

Contact: Gugu Charlie

Tel: +27 11 834-1273/7, Fax: +27 11 838-5923/833-8156

E-mail: [gugu@saimm.co.za](mailto:gugu@saimm.co.za), Website: <http://www.saimm.co.za>

**21-25 August 2022 — XXXI International Mineral Processing Congress 2022**

Melbourne, Australia + Online, [www.impc2022.com](http://www.impc2022.com)

**6-8 September 2022 — PGM The 8th International Conference 2022**

Sun City, Rustenburg, South Africa

Contact: Camielah Jardine

Tel: +27 11 834-1273/7, Fax: +27 11 838-5923/833-8156

E-mail: [camielah@saimm.co.za](mailto:camielah@saimm.co.za), Website: <http://www.saimm.co.za>

**7-8 September 2022 — Thermodynamic from Nanoscale to Operational Scale (THANOS) International Hybrid Conference 2022**

*on Enhanced use of Thermodynamic Data in Pyrometallurgy Teaching and Research*

Mintek, Randburg, South Africa

Contact: Camielah Jardine

Tel: +27 11 834-1273/7, Fax: +27 11 838-5923/833-8156

E-mail: [camielah@saimm.co.za](mailto:camielah@saimm.co.za), Website: <http://www.saimm.co.za>

## Company affiliates

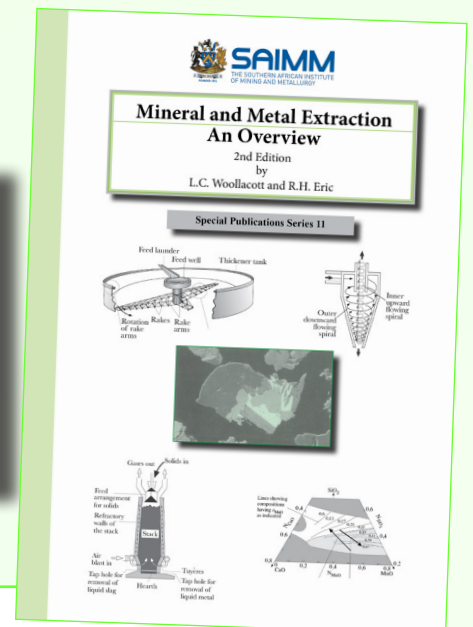
The following organizations have been admitted to the Institute as Company Affiliates

3M South Africa (Pty) Limited	Expectra 2004 (Pty) Ltd	MSA Group (Pty) Ltd
AECOM SA (Pty) Ltd	Exxaro Coal (Pty) Ltd	Multotec (Pty) Ltd
AEL Mining Services Limited	Exxaro Resources Limited	Murray and Roberts Cementation
African Pegmatite (Pty) Ltd	Filtaquip (Pty) Ltd	Nalco Africa (Pty) Ltd
Air Liquide (Pty) Ltd	FLSmith Minerals (Pty) Ltd	Namakwa Sands(Pty) Ltd
Alexander Proudfoot Africa (Pty) Ltd	Fluor Daniel SA ( Pty) Ltd	Ncamiso Trading (Pty) Ltd
AMEC Foster Wheeler	Franki Africa (Pty) Ltd-JHB	New Concept Mining (Pty) Limited
AMIRA International Africa (Pty) Ltd	Fraser Alexander (Pty) Ltd	Northam Platinum Ltd - Zondereinde
ANDRITZ Delkor (Pty) Ltd	G H H Mining Machines (Pty) Ltd	Opermin Operational Excellence
Anglo Operations Proprietary Limited	Geobruigg Southern Africa (Pty) Ltd	OPTRON (Pty) Ltd
Anglogold Ashanti Ltd	Glencore	Paterson & Cooke Consulting Engineers (Pty) Ltd
Arcus Gibb (Pty) Ltd	Gravitas Minerals (Pty) Ltd	Perkinelmer
ASPASA	Hall Core Drilling (Pty) Ltd	Polysius A Division of Thyssenkrupp Industrial Sol
Aurecon South Africa (Pty) Ltd	Hatch (Pty) Ltd	Precious Metals Refiners
Aveng Engineering	Herrenknecht AG	Rams Mining Technologies
Aveng Mining Shafts and Underground	HPE Hydro Power Equipment (Pty) Ltd	Rand Refinery Limited
Axiom Chemlab Supplies (Pty) Ltd	Immersive Technologies	Redpath Mining (South Africa) (Pty) Ltd
Axis House (Pty) Ltd	IMS Engineering (Pty) Ltd	Rocbolt Technologies
Bafokeng Rasimone Platinum Mine	Ingwenya Mineral Processing (Pty) Ltd	Rosond (Pty) Ltd
Barloworld Equipment -Mining	Ivanhoe Mines SA	Royal Bafokeng Platinum
BASF Holdings SA (Pty) Ltd	Joy Global Inc. (Africa)	Roytec Global (Pty) Ltd
BCL Limited	Kudumane Manganese Resources	RungePincockMinarco Limited
Becker Mining (Pty) Ltd	Leica Geosystems (Pty) Ltd	Rustenburg Platinum Mines Limited
BedRock Mining Support (Pty) Ltd	Longyear South Africa (Pty) Ltd	Salene Mining (Pty) Ltd
BHP Billiton Energy Coal SA Ltd	Lull Storm Trading (Pty) Ltd	Sandvik Mining and Construction Delmas (Pty) Ltd
Blue Cube Systems (Pty) Ltd	Maccaferri SA (Pty) Ltd	Sandvik Mining and Construction RSA(Pty) Ltd
Bluhm Burton Engineering Pty Ltd	Magnetech (Pty) Ltd	SANIRE
Bond Equipment (Pty) Ltd	MAGOTTEAUX (Pty) LTD	Schauenburg (Pty) Ltd
Bouygues Travaux Publics	Malvern Panalytical (Pty) Ltd	Sebilo Resources (Pty) Ltd
Castle Lead Works	Maptek (Pty) Ltd	SENET (Pty) Ltd
CDM Group	Maxam Dantex (Pty) Ltd	Senmin International (Pty) Ltd
CGG Services SA	MBE Minerals SA Pty Ltd	SISA Inspection (Pty) Ltd
Coalmin Process Technologies CC	MCC Contracts (Pty) Ltd	Smec South Africa
Concor Opencast Mining	MD Mineral Technologies SA (Pty) Ltd	Sound Mining Solution (Pty) Ltd
Concor Technicrete	MDM Technical Africa (Pty) Ltd	SRK Consulting SA (Pty) Ltd
Council for Geoscience Library	Metalock Engineering RSA (Pty)Ltd	Time Mining and Processing (Pty) Ltd
CRONIMET Mining Processing SA (Pty) Ltd	Metorex Limited	Timrite (Pty) Ltd
CSIR Natural Resources and the Environment (NRE)	Metso Minerals (South Africa) (Pty) Ltd	Tomra (Pty) Ltd
Data Mine SA	Micromine Africa (Pty) Ltd	Traka Africa (Pty) Ltd
Digby Wells and Associates	MineARC South Africa (Pty) Ltd	Ukwazi Mining Solutions (Pty) Ltd
DRA Mineral Projects (Pty) Ltd	Minerals Council of South Africa	Umgeni Water
DTP Mining - Bouygues Construction	Minerals Operations Executive (Pty) Ltd	Webber Wentzel
Duraset	MineRP Holding (Pty) Ltd	Weir Minerals Africa
Elbroc Mining Products (Pty) Ltd	Mining Projections Concepts	Welding Alloys South Africa
eThekwini Municipality	Mintek	Worley
Ex Mente Technologies (Pty) Ltd	MIP Process Technologies (Pty) Limited	
	MLB Investment CC	
	Modular Mining Systems Africa (Pty) Ltd	

**New Book Release**

# Mineral and Metal Extraction An Overview

2nd Edition  
by  
L.C. Woollacott and R.H. Eric



## ABOUT THE BOOK

The intention of this book is to provide a concise overview of the processing of mined material that is comprehensive in scope and digestible in form. Both mineral beneficiation and extractive metallurgy are considered with each receiving about the same amount of attention.

The overview will be helpful to anyone interested in the processing of mined material and the extraction of metals. For the most part, non-practitioners are interested only in the broad issues and not the fine detail. The overview addresses their needs directly. For students—who might sometimes lose sight of the more general aspects in their efforts to understand the detail—it provides a broad perspective that will strengthen their overall understanding of the subject. Even for practitioners the overview will be helpful when needing to review those aspects of the technology with which they are less familiar.

Because the overview will be of particular interest to geologists, mineralogists, and mining engineers a slight bias has been introduced for their benefit. Those topics that are closer to their areas of interest—namely ore properties, physical processing and mineral beneficiation—have been presented in slightly greater detail than have other areas of the technology.

Several strategies have been adopted in an effort to make the overview comprehensive, concise, and easily understandable. In the first place, concepts and principles have been given particular attention. In regard to detail, only as much as is needed to gain a good general grasp of the various aspects of the technology has been presented. To cater for a broad audience the level of the discussion is predominantly qualitative and no assumptions are made about the readers background beyond a general familiarity with physics and chemistry.

## ABOUT THE SECOND EDITION

Three additional chapters have been included in this edition. Chapter 14 addresses the more general aspects of extractive processing: namely process economics and cost engineering; materials handling (the ancillary operations and equipment needed to 'handle' solids, liquids and gases appropriately before and after processing stages) and a fairly detailed treatment of process control and process management. Chapter 15 focuses on topics relating to environmental impacts—namely recycling and the disposal of processing wastes—while the final chapter addresses the issues of sustainability, the circular economy and the future of the mineral and metal industry.

In addition to the updating of all topics covered in the first edition, three sub-chapters have been added dealing with sampling, centrifugal gravity concentration, and ionic liquids. The sections on the textural and liberation characteristics of ores, and on the design of mineral processing circuits have also been largely rewritten. The review of mineral and metal extraction routes has also been updated.

## TO PLACE AN ORDER CONTACT

**The Southern African Institute of Mining and Metallurgy**

**Mineral and Metal Extraction An Overview**

by L.C. Woollacott and R.H. Eric

Please contact: Tsholo Solo • Email: [saimmreception@saimm.co.za](mailto:saimmreception@saimm.co.za)

Please indicate your choice by (✓ tick)

Hard Copy: R700 (excluding VAT and postage)  Number of copies

E-book: R400 (excluding VAT)  Number of copies

**Order Now to avoid  
disappointment!!**

# Real power comes from ideas

## We've got **what it takes**

Operators use our pumps, valves, actuators and automation products across all primary and secondary processes in more than 1,000 power stations. KSB products help you manage boiler feed water, condensate and cooling water systems. Around the world, more than 170,000 of our pumps and some three million valves are already in action helping to generate energy.

KSB has been serving customers with innovative solutions for more than 140 years. Our know-how and experience across a wide spectrum of pump and valve technology make us the ideal partner for the consultants, plant engineering contractors and operators of high-performance power stations.

**KSB Pumps and Valves (Pty) Ltd**

**Tel: +27-11-876-5600**

**[www.ksb.com/ksb-za](http://www.ksb.com/ksb-za)**

**Your B\_BBEE Partner**



Boiler feed pumps



High Pressure Globe Valves

**KSB**  
ENERGY

